Horizon 2020
European Union Funding
for Research & Innovation

SILVARSTAR

Grant agreement number: 101015442
Project Acronym: SILVARSTAR
Project title: Soil vibration and Auralisation Software Tools for Application in Railways

DELIVERABLE D1.3

Validation of the prototype vibration prediction tool against documented cases

Project acronym:	SILVARSTAR
Starting date:	01/11/2020
Duration (in months):	24
Call (part) identifier:	H2020-S2RJU-2020 (Shift2Rail JU call proposals 2020) Topic: S2R-OC-CCA-01-2020
Grand agreement no:	101015442
Grand Amendments:	NA
Due date of deliverable:	30/04/2022
Actual submission date:	30/06/2022
Coordinator:	Pascal Bouvet, VIBRATEC
Lead Beneficiary:	KU Leuven
Version:	Final
Type:	Report
Sensitivity or Dissemination level[1]:	PU
Contribution to S2R TDs or WAs[2]	WA5
Taxonomy/keywords:	railway induced ground vibration, hybrid vibration prediction model, numerical validation, experimental validation

This project has received funding from the Shift2Rail Joint Undertaking (JU) under grant agreement 101015442. The JU receives support from the European Union's Horizon 2020 Research and Innovation Programme and the Shift2Rail JU members other than the Union.

[1] PU: Public; CO: Confidential, only for members of the consortium (including Commission Services)
[2] https://projects.shift2rail.org/s2r_matrixtd.aspx

Domain	WP1, Task T1.4
Leader	Geert Degrande
Deliverable	D1.3
Title	Validation of the prototype vibration prediction tool against documented cases
Authors	Pieter Reumers[1], Geert Degrande[1], Geert Lombaert[1], Fakhraddin Seyfaddini[1], Geertrui Herremans[1], Evangelos Ntotsios[2], David Thompson[2], Brice Nélain[3], Pascal Bouvet[3], Bernd Fröhling[4] and Andreas Nuber[4]
Partners	[1]KU Leuven, [2]ISVR, University of Southampton, [3]Vibratec and [4]Wölfel
Document Code	20220630_D1.3_Validation_V1.0_KULeuven
Due date	30 April 2022
Submission date	30 June 2022

Document history

Date	Name	Company	Details of Contribution	Position/ Project Role
01/01/2022	Geert Degrande	KU Leuven	Initial draft framework	WP1 leader
28/02/2022	Fakhraddin Seyfaddini	KU Leuven	Section 2	Partner
28/02/2022	Geertrui Herremans	KU Leuven	Section 2	Partner
15/05/2022	Pieter Reumers	KU Leuven	Sections 1, 2, 3, 4, 6	Task T1.4 leader
15/05/2022	Evangelos Ntotsios	ISVR	Sections 2, 3	Partner
15/05/2022	Brice Nélain	Vibratec	Section 5	Partner
24/05/2022	Pieter Reumers	KU Leuven	Assembly final document	Task T1.4 leader
25/05/2022	Geert Degrande	KU Leuven	Review	WP1 leader
10/06/2022	David Thompson	ISVR	Review	WP2 leader
17/06/2022	Pieter Reumers	KU Leuven	Final version	Task T1.4 leader
20/06/2022	Geert Degrande	KU Leuven	Final review	WP1 leader

TABLE OF CONTENTS

LIST OF FIGURES

LIST OF TABLES

LIST OF ABBREVIATIONS

2D	Two-dimensional
2.5D	Two-and-a-half-dimensional
3D	Three-dimensional
BE	Boundary element
BEM	Boundary element method
DOF	Degree of freedom
DIN	Deutsche Institut für Normung
EU	European Union
FE	Finite element
FEM	Finite element method
FRA	Federal Railroad Administration
FTA	Federal Transit Administration
HBL	Hydraulically bonded layer
HSL	High speed line
HST	High speed train
IC	Intercity
ICE	Intercity Express
ISO	International Organization for Standardization
P2	Resonance of vehicle unsprung mass on combined track-soil stiffness
PSD	Power spectral density
RMS	Root mean square
SASW	Spectral Analysis of Surface Waves
SCPT	Seismic Cone Penetration Test
SR	Seismic Refraction
UIC	International Union of Railways
WP	Work Package

EXECUTIVE SUMMARY

This report forms Deliverable D1.3 "Validation of the prototype vibration prediction tool against documented cases" of the Collaborative Project SILVARSTAR that is funded under the European Union's Horizon 2020 Research and Innovation Program under the open call as part of the Cross Cutting Activities of the Shift2Rail Joint Undertaking.

The report initially presents the comparison between state-of-the-art numerical models TRAFFIC (developed by KU Leuven) and MOTIV (developed by ISVR) corresponding to work carried out in Task T2.2 of the Description of Work. The comparison is performed in terms of vehicle and track compliance, dynamic axle loads, vibration velocity levels, line source transfer mobility and force density. There are 18 case histories (two track types, three soil types and three train speeds) considered.

Next, TRAFFIC is used to validate the simplifying assumptions made in the prototype vibration prediction tool to reduce the computational time. The modelling simplifications are introduced gradually. First, the track compliance is computed in a stationary instead of a moving frame of reference. Subsequently, the dynamic axle loads are applied to the track at fixed positions, which results in a low-speed approximation that does not account for the Doppler effect. As a final simplification, the axle loads are assumed as incoherent.

Subsequently, the validation of the prototype vibration prediction tool against numerical case histories corresponding to Task T1.4 in the Description of Work is presented. We focus on the following quantities of interest: line source transfer mobility, vibration velocity level and force density. These quantities are computed for the 18 numerical case histories with TRAFFIC (including all modelling simplifications) and are compared with the predictions of the prototype vibration prediction tool.

The final part of this report presents the validation of the prototype vibration prediction tool against experimental case histories corresponding to Task T1.4 in the Description of Work. Extensive experimental data (transfer functions and train passages) were collected at a site in Lincent (Belgium). The prototype vibration prediction tool is used to predict the line source transfer mobility, vibration velocity level and force density, which are subsequently compared to the experimental data.

1. INTRODUCTION

This report focuses on the validation of the prototype vibration prediction tool against numerical and experimental case histories, corresponding to Task T1.4 in the Description of Work.

For the numerical validation, results obtained with the prototype vibration prediction tool are validated with state-of-the-art prediction models TRAFFIC (developed by KU Leuven) [9] and MOTIV (developed by ISVR) [14, 12, 13]. An extensive description of both models is presented in Deliverable D1.1 [2], while detailed information on the prototype vibration prediction tool is provided in Deliverable D1.2 [1]. For the experimental validation, measurement data (transfer functions and train passages) collected at a site in Lincent (Belgium) are used.

The numerical validation of the prototype vibration prediction tool is performed for 18 cases: two track forms (ballasted and slab track), three soil conditions (soft, medium and stiff), one train (IC train with 4 carriages), and three train speeds (50 km/h, 150 km/h and 300 km/h). The properties of the track, train and soil, as well as the track unevenness are taken from the numerical database described in Deliverable D2.1 [17].

Prior to the validation of the prototype vibration prediction tool, results obtained with state-of-the-art models TRAFFIC and MOTIV are compared for the 18 case histories (ballasted and slab track), corresponding to work carried out in Task T2.2 in the Description of Work. The comparison is performed in terms of vehicle and track compliance, dynamic axle loads, transfer functions, line source transfer mobility, vibration velocity levels and force densities. The vibration velocity level is computed accounting for the Doppler effect (due to the moving axle loads) and includes the contribution of the quasi-static and dynamic excitation (due to the rail unevenness).

In the prototype vibration prediction tool, however, a number of modelling simplifications are made in order to reduce computation times. These simplifications include: (1) the computation of the track compliance in a stationary instead of a moving frame of reference; (2) the application of the dynamic axle loads at fixed positions (low-speed approximation neglecting the Doppler effect); and (3) the assumption of incoherent instead of coherent axle loads. The influence of these modelling assumptions on the free field vibration velocity levels is quantified with TRAFFIC.

Next, the implementation of the prototype vibration prediction tool is validated by comparing the line source transfer mobility, vibration velocity level and force density with computations made with TRAFFIC for the 18 cases accounting for the aforementioned modelling simplifications. The prototype vibration prediction tool uses pre-computed soil impedance and transfer functions available in the numerical database, as described in Deliverable D2.1 [17].

The prototype vibration prediction tool is subsequently validated by means of experimental results that have been collected at a site in Lincent (Belgium) next to the high speed line L2 Brussels-Köln. Extensive vibration measurements were performed at this site, resulting in a large data set containing transfer functions and vibration velocity levels during train passages. This is completed with determination of dynamic soil characteristics by means of situ geophysical prospection tests (SASW, SCPT, seismic refraction) and laboratory tests (bender element tests). The validation is performed by comparing experimental vibration velocity levels to those obtained with numerical and hybrid models.

This report is organized as follows. Section 2 presents the comparison between state-of-the-art numerical models TRAFFIC and MOTIV for 18 case histories. Section 3 assesses the modelling assumptions made in the prototype vibration prediction tool by means of comparison with results computed with TRAFFIC. Section 4 reports on the validation of the prototype vibration prediction tool for the 18 case histories by means of comparison with results computed with TRAFFIC. Section 5 reports on the validation of the prototype vibration prediction tool by means of comparison with experimental results measured on the site in Lincent. Section 6 concludes the report.

2. COMPARISON OF STATE-OF-THE-ART NUMERICAL MODELS

2.1 Introduction

In this section, we use two state-of-the-art models TRAFFIC [9] and MOTIV [12, 13, 14] to compute the track and free field response for 18 case histories. Comparisons between them are used to verify that they can give equivalent results. A detailed description of the train-track-soil models used in TRAFFIC and MOTIV is presented in Deliverable D1.1 [2]. The 18 case histories consist of two tracks (ballasted and slab track) on top of a homogeneous halfspace with three stiffness values (soft, medium, and stiff). An IC train with 4 carriages is running on these tracks with three speeds (50 km/h, 150 km/h and 300 km/h). The properties of the track, soil and train, and the unevenness profile are selected from the numerical database as described in Deliverable D2.1 [2]. In section 4, these 18 case histories are also used for the numerical validation of the prototype vibration prediction tool.

This section is organized as follows. First, the track models, soil properties, track unevenness and train properties are briefly recapitulated. Next, the comparison between TRAFFIC and MOTIV is presented in terms of track and vehicle compliance, dynamic axle loads, transfer functions, line source transfer mobility, vibration velocity level and force density. This is first performed for the ballasted track, and next for the slab track.

2.2 Track models

In TRAFFIC and MOTIV, two-and-a-half-dimensional (2.5D) track models are used to efficiently solve the track-soil interaction problem and account for moving loads. It is assumed that the track geometry, material properties and soil layering are invariant in the longitudinal direction $\mathbf{e}_y$. By application of a forward Fourier transform from the coordinate y to the wavenumber domain k_y, the 3D track-soil interaction problem is solved as a superposition of 2D problems for each wavenumber k_y.

2.2.1 Ballasted track

The ballasted track model is shown in figure 1 and the track properties are summarized in table 1. The origin of the Cartesian frame of reference is at the centre of the track-soil interface Σ, with the $x-$axis pointing to the right and the $z-$axis pointing upwards.

The numerical implementation of the ballasted track model in TRAFFIC and MOTIV is elaborated in section 4 of Deliverable D1.1 [2]. The implementation mainly differs in the kinematic assumptions made at the track-soil interface: TRAFFIC assumes that the track-soil interface is rigid in the plane of the track cross-section, resulting in two degrees of freedom (DOFs) (vertical displacement and rotation about the y-axis) as illustrated in figure 1a. MOTIV, on the other hand, allows for an arbitrary distribution of displacements and tractions across the width of the track by dividing the track-soil interface in n_s strips (figure 1b). This results in n_s DOFs at the track-soil interface, corresponding to the vertical displacement for each of the

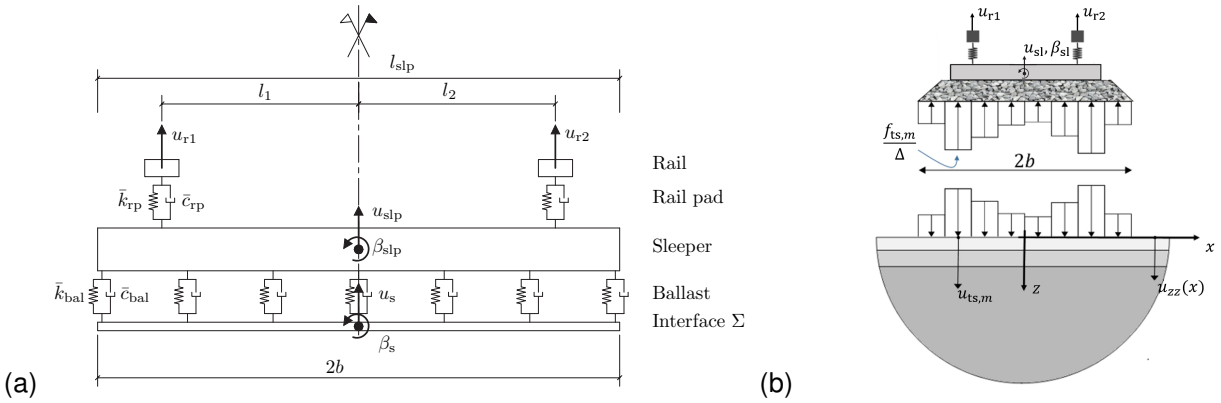

Figure 1: Cross-section of the ballasted track model with kinematic assumptions made in (a) TRAFFIC and (b) MOTIV.

Table 1: Properties of the ballasted track.

Rail UIC60	Rail positions	$l_1 = l_2 = 0.72$ m
	Cross-sectional area	$A_{\mathrm{r}} = 76.70 \times 10^{-4}$ m^2
	Moment of inertia about x-axis	$I_{\mathrm{r}} = 3057.1 \times 10^{-8}$ m^4
	Young's modulus	$E_{\mathrm{r}} = 210 \times 10^{9}$ N/m^2
	Damping loss factor	$\eta_{\mathrm{r}} = 0.01$
	Density	$\rho_{\mathrm{r}} = 7850$ kg/m^3
Rail pad	Stiffness	$k_{\mathrm{rp}} = 150 \times 10^{6}$ N/m
	Damping loss factor	$\eta_{\mathrm{rp}} = 0.3$
Sleeper	Spacing	$d_{\mathrm{slp}} = 0.6$ m
	Length	$l_{\mathrm{slp}} = 2.6$ m
	Height	$h_{\mathrm{slp}} = 0.2$ m
	Width	$b_{\mathrm{slp}} = 0.25$ m
	Mass	$m_{\mathrm{slp}} = 325$ kg
Ballast	Height	$h_{\mathrm{bal}} = 0.3$ m
	Top width	$b_{\mathrm{bal}t} = 3.0$ m
	Bottom width	$b_{\mathrm{bal}b} = 3.6$ m
	Stiffness per sleeper	$k_{\mathrm{bal}} = 500 \times 10^{6}$ N/m
	Poisson's ratio	$\nu_{\mathrm{bal}} = 0.0$
	Damping loss factor	$\eta_{\mathrm{bal}} = 0.15$
	Density	$\rho_{\mathrm{bal}} = 1500$ kg/m^3
	Mass per unit length	$m_{\mathrm{bal}} = 1485$ kg/m

n_{s} strips. Both models assume relaxed boundary conditions, as there is no coupling between horizontal DOFs of the track and the soil.

The rails are modelled as Euler-Bernoulli beams with bending stiffness $E_{\mathrm{r}}I_{\mathrm{r}}$ and mass per unit length $\rho_{\mathrm{r}}A_{\mathrm{r}}$. The rail displacements are denoted as $u_{\mathrm{r}1}(y,t)$ and $u_{\mathrm{r}2}(y,t)$. The positions of the rail are determined by l_1 and l_2.

The rail pads are modelled as continuous springs between the rails and the sleeper. The stiffness k_{rp} of a single rail pad is used to calculate an equivalent stiffness per unit length $\overline{k}_{\mathrm{rp}} = k_{\mathrm{rp}}/d$, where d is the distance between sleepers. Damping is accounted for by a hysteretic loss factor η_{rp}, resulting in a complex value for the rail pad stiffness $\overline{k}^*_{\mathrm{rp}} = \overline{k}_{\mathrm{rp}}(1 + \mathrm{i}\eta_{\mathrm{rp}})$.

The sleepers are assumed to be rigid in the plane of the track cross-section. Hence, the vertical motion of the sleeper is described by the vertical displacement $u_{\mathrm{slp}}(y, t)$ at its centre of mass and the rotation $\beta_{\mathrm{slp}}(y, t)$ about the longitudinal axis. The sleepers do not contribute to the longitudinal stiffness of the track, and are modelled as a uniformly distributed mass $\overline{m}_{\mathrm{slp}} = m_{\mathrm{slp}}/d$ per unit length along the track, where m_{slp} is the mass of an individual sleeper.

If the ballast bed is assumed to act as a set of distributed, independent linear springs and dampers, each sleeper is only supported by that part of the ballast that is in contact with the sleeper. Hence, the ballast stiffness per sleeper k_{bal} [N/m] is calculated from the sleeper width b_{slp}, the sleeper length l_{slp} and the ballast bedding modulus K_{bal} [N/m^3] as $b_{\mathrm{slp}} l_{\mathrm{slp}} K_{\mathrm{bal}}$. The smeared ballast stiffness $\overline{k}_{\mathrm{bal}}$ [N/m^2] is equal to k_{bal}/d. Damping in the ballast bed is accounted for by a hysteretic loss factor η_{bal} resulting in a complex value for the ballast stiffness $\overline{k}^*_{\mathrm{bal}} = \overline{k}_{\mathrm{bal}}(1 + \mathrm{i}\eta_{\mathrm{bal}})$.

Analytical expressions are derived for the elements of the track stiffness matrix $\tilde{\mathbf{K}}^{\mathrm{tr}}(\omega)$, which are given in section 4.2.2 of Deliverable D1.1 [2] for TRAFFIC and MOTIV.

2.2.2 Slab track

The track is a typical monolithic wet-poured slab track based on the Rheda 2000 slab track system shown in figure 2 [13]. The slab system rests on a hydraulically bonded layer (HBL) consisting of a mixture of aggregates with a bonding agent. Both UIC60 rails are discretely supported every 0.65 m by rail pads between the rails and the slab.

The track model as it is implemented in MOTIV and TRAFFIC is shown in figure 3. An analytical model of the slab track is coupled to the underlying soil. Equivalent slab properties were computed to account for the hydraulically bonded layer.

The rails are modelled as Euler-Bernoulli beams with bending stiffness $E_{\mathrm{r}} I_{\mathrm{r}}$ and mass per unit length $\rho_{\mathrm{r}} A_{\mathrm{r}}$. The rail pads are represented by a spring connection between the rails and the slab. The smeared rail pad

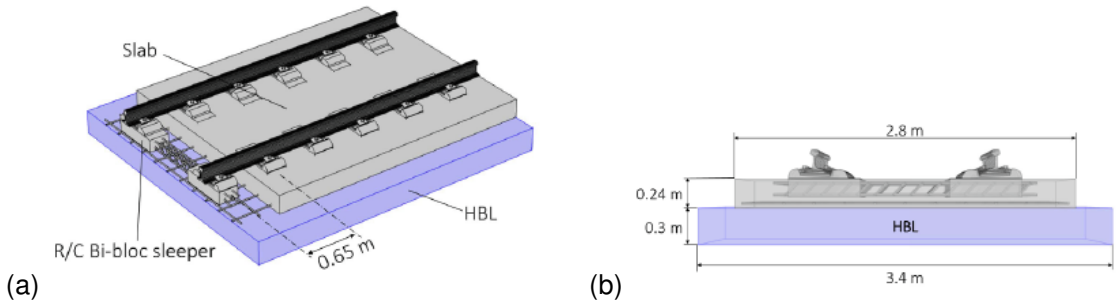

Figure 2: The Rheda 2000 slab track system [13]. (a) 3D segment of the continuous track and underlying HBL and (b) track cross-section.

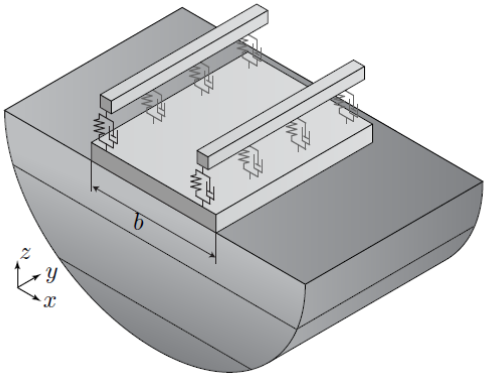

Figure 3: Problem geometry for slab track.

Table 2: Properties of the slab track [13].

Rail UIC60	Rail positions	$l_1 = l_2 = 0.72$ m
	Cross-sectional area	$A_\mathrm{r} = 76.70 \times 10^{-4}$ m^2
	Moment of inertia about x-axis	$I_\mathrm{r} = 3057.1 \times 10^{-8}$ m^4
	Young's modulus	$E_\mathrm{r} = 210 \times 10^9$ N/m^2
	Damping loss factor	$\eta_\mathrm{r} = 0.01$
	Density	$\rho_\mathrm{r} = 7850$ kg/m^3
Rail pad	Spacing	$d = 0.65$ m
	Stiffness	$k_\mathrm{rp} = 120 \times 10^6$ N/m
	Damping loss factor	$\eta_\mathrm{rp} = 0.15$
Slab*	Width	$b_\mathrm{sl} = 3.4$ m
	Mass per unit length	$\rho_\mathrm{sl} A_\mathrm{sl} = 3720$ kg/m
	Bending stiffness	$E_\mathrm{sl} I_\mathrm{sl} = 233 \times 10^6$ Nm^2
	Damping loss factor	$\eta_\mathrm{sl} = 0.015$
	Torsional stiffness	$G_\mathrm{sl} C_\mathrm{sl} = 339 \times 10^6$ Nm^2
	Mass moment of inertia	$\rho_\mathrm{sl} I_\mathrm{sl,t} = 3086$ kgm

*Equivalent properties of the slab and the hydraulically bonded layer.

stiffness is equal to $\bar{k}_\mathrm{rp} = k_\mathrm{rp}/d$. Damping is accounted for by a hysteretic loss factor η_rp, resulting in a complex value for the rail pad stiffness $\bar{k}^*_\mathrm{rp} = \bar{k}_\mathrm{rp}(1 + \mathrm{i}\eta_\mathrm{rp})$.

The slab (including the hydraulically bonded layer) is simplified to an equivalent beam which is assumed to be rigid in the plane of its cross-section. The beam has a width b_sl, mass per unit length $\rho_\mathrm{sl} A_\mathrm{sl}$, bending stiffness $E_\mathrm{sl} I_\mathrm{sl}$, mass moment moment of inertia $\rho_\mathrm{sl} I_\mathrm{sl,t}$ and torsional stiffness $G_\mathrm{sl} C_\mathrm{sl}$. The vertical motion of the slab $u_{\mathrm{sl}z}(x, y, t)$ is described by the vertical displacement of its centre $u_\mathrm{sl}(y, t)$ and rotation $\beta_\mathrm{sl}(y, t)$ about the longitudinal axis:

$$u_{\mathrm{sl}z}(x, y, t) \quad = \quad u_\mathrm{sl}(y, t) + x\beta_\mathrm{s}(y, t). \tag{1}$$

Analytical expressions can be derived for the elements of the track stiffness matrix $\tilde{\mathbf{K}}^\mathrm{tr}(\omega)$ in a similar way as for the ballasted track. The resulting track properties are based on the specifications of the Rheda 2000

track as detailed by Ntotsios et al. [13] and are summarized in table 2.

2.3 Soil properties

Three homogeneous soils are considered. The dynamic soil characteristics are summarized in table 3; these correspond to the soft, medium and stiff soil as discussed in section 5.1.1 of Deliverable D2.1 [17]. Each soil is characterized by its shear wave velocity C_{s}, dilatational wave velocity C_{p}, density ρ and material damping ratios β_{s} and β_{p} for shear and dilatational deformation, respectively.

Table 3: Dynamic soil characteristics.

Soil type	C_{s} [m/s]	C_{p} [m/s]	ρ [kg/m^3]	β_{s} [-]	β_{p} [-]
Soft	100	200	1800	0.025	0.025
Medium	200	400	1800	0.025	0.025
Stiff	400	800	1800	0.025	0.025

2.4 Track unevenness

The track unevenness is determined following guidelines from the Federal Railroad Administration (FRA) taking into account track quality. Figure 4 shows the one-sided PSD functions of the track unevenness $\tilde{S}_{rzz}(k_y)$ [m^2/(rad/m)] for FRA track quality classes 1 to 6. These are determined by the following expression [6]:

$$\tilde{S}_{rzz}(k_y) \quad = \quad \frac{1}{2\pi} A \frac{n_{y2}^2 (n_y^2 + n_{y1}^2)}{n_y^4 (n_y^2 + n_{y2}^2)} \tag{2}$$

where $n_y = k_y/2\pi$, $n_{y1} = 0.0233\,\mathrm{m}^{-1}$ and $n_{y2} = 0.13\,\mathrm{m}^{-1}$. The parameter A depends on the track quality class, labelled from 1 to 6, where 1 represents the poorest and 6 the best track quality [4, 6]. The values for A are summarized in table 4 for each class. For the 18 numerical case histories, we assume a track quality class 6 corresponding to smooth track. Wheel unevenness is disregarded.

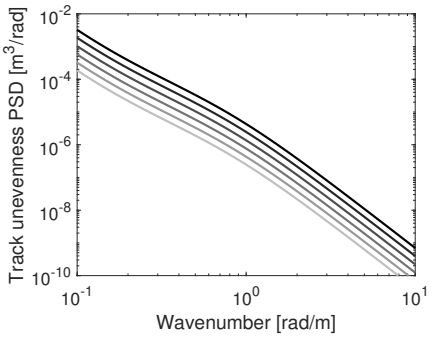

Figure 4: One-sided PSD of the track unevenness for FRA track quality classes 1 (black line) to 6 (light grey line).

Table 4: Track quality parameters according to the FRA database [6].

Class	1	2	3	4	5	6
A [10^{-7} m]	16.72	9.53	5.29	2.96	1.67	0.96

From the one-sided PSD $\tilde{S}_{rzz}(k_y)$, a sample of the track unevenness $u_{\mathrm{rz}}(y)$ [m] is generated using the spectral representation theorem [16]:

$$u_{\mathrm{rz}}(y) = \sum_{m=1}^{n} \sqrt{2\tilde{S}_{\mathrm{rzz}}(k_{ym})\Delta k_y}\cos(k_{ym}y - \theta_m) \tag{3}$$

where $k_{ym} = m\Delta k_y$ is the wavenumber sampling, Δk_y the wavenumber bin and θ_{m} are independent random phase angles uniformly distributed in $[0, 2\pi]$. Figure 5a shows a track unevenness sample generated from the one-sided PSD for FRA track quality class 6. The one-sided PSD of this track unevenness sample $u_{\mathrm{rz}}(y)$ can be estimated using Welch's method [20]. Figure 5b compares the PSD obtained from the track unevenness sample to the PSD for FRA track quality class 6.

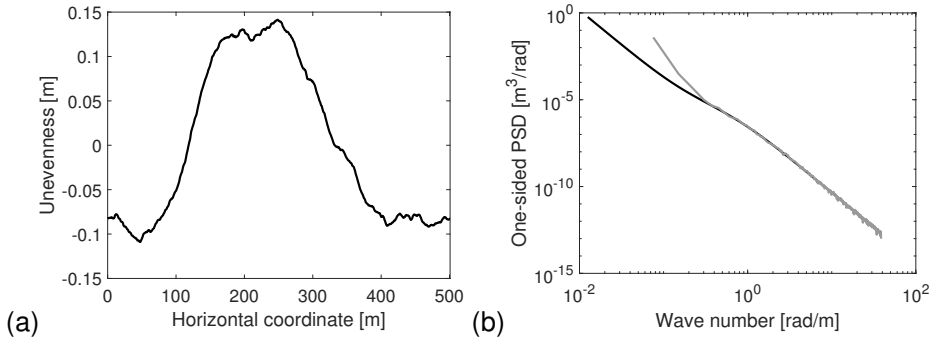

Figure 5: (a) Track unevenness sample as a function of the coordinate y. (b) Comparison of the estimated PSD obtained using Welch's method (grey line) to the PSD for FRA track quality class 6 (black line).

The track unevenness in the frequency domain $\hat{\mathbf{u}}_{\mathrm{w/r}}(\omega)$ [m/Hz] perceived by each axle moving at speed v is determined as:

$$\hat{\mathbf{u}}_{\mathrm{w/r}}(\omega) = \frac{1}{v}\tilde{u}_{\mathrm{rz}}\left(-\frac{\omega}{v}\right)\hat{\mathbf{T}}(\omega) \tag{4}$$

where $\tilde{u}_{\mathrm{rz}}(k_y)$ is the wavenumber transform of the rail unevenness $u_{\mathrm{rz}}(y)$ and $\hat{\mathbf{T}}(\omega)$ is a $3n_{\mathrm{a}} \times 1$ vector that contains the phase shift for each axle:

$$\hat{\mathbf{T}}(\omega) = \left\{\ldots, 0, \exp\left(+\mathrm{i}\omega\frac{y_{k0}}{v}\right), 0, \ldots\right\}^{\mathrm{T}} \tag{5}$$

with y_{k0} the initial position of axle k. The first term on the right-hand side of equation (4) is given by:

$$\frac{1}{v}\tilde{u}_{\mathrm{rz}}\left(-\frac{\omega}{v}\right) = \sum_{m=1}^{n}\frac{-1}{\sqrt{v}}\sqrt{2\tilde{S}_{\mathrm{rzz}}\left(\frac{|\omega_m|}{v}\right)\Delta\omega_m}\left[\pi\delta(\omega-\omega_m)e^{+\mathrm{i}\theta_m} + \pi\delta(\omega+\omega_m)e^{-\mathrm{i}\theta_m}\right] \tag{6}$$

where $\Delta\omega_m = v\Delta k_y$ and $\omega_m = -vk_{ym}$. For different samples of unevenness, the harmonic functions have the same modulus, but a different random phase.

2.5 Dynamic axle loads

The dynamic axle loads $\hat{\mathbf{g}}_{\mathrm{d}}(\omega)$ [N/Hz] are determined by assuming perfect contact between the train and the track. This leads to a coupled system of equations in terms of the vehicle compliance $\hat{\mathbf{C}}^{\mathrm{v}}(\omega)$ and the track compliance $\hat{\mathbf{C}}^{\mathrm{t}}(\omega)$:

$$\left[\hat{\mathbf{C}}^{\mathrm{t}}(\omega) + \hat{\mathbf{C}}^{\mathrm{v}}(\omega)\right] \hat{\mathbf{g}}_{\mathrm{d}}(\omega) \quad = \quad -\hat{\mathbf{u}}_{\mathrm{w/r}}(\omega) \tag{7}$$

The inverse $[\hat{\mathbf{C}}^{\mathrm{t}}(\omega) + \hat{\mathbf{C}}^{\mathrm{v}}(\omega)]^{-1}$ [N/m] of the total compliance matrix can be considered as the dynamic stiffness matrix of the coupled vehicle-track system.

The one-sided PSD matrix of the dynamic axle loads $\hat{\mathbf{S}}_{\mathbf{g}}(\omega)$ [N^2/(rad/s)] is determined from the one-sided PSD of the track unevenness:

$$\hat{\mathbf{S}}_{\mathbf{g}}(\omega) \quad = \quad \left[\hat{\mathbf{C}}^{\mathrm{t}}(\omega) + \hat{\mathbf{C}}^{\mathrm{v}}(\omega)\right]^{-1} \hat{\mathbf{T}}(\omega) \frac{1}{v} \tilde{S}_{\mathrm{rzz}}\left(-\frac{\omega}{v}\right) \hat{\mathbf{T}}^{\mathrm{H}}(\omega) \left[\hat{\mathbf{C}}^{\mathrm{t}}(\omega) + \hat{\mathbf{C}}^{\mathrm{v}}(\omega)\right]^{-\mathrm{H}} \tag{8}$$

where $(\cdot)^{\mathrm{H}}$ denotes the complex conjugate transpose.

2.6 Train properties

For the estimation of the dynamic axle loads, the vehicle is usually modelled as a multi-degree of freedom system, where the vehicle's car body, bogies and wheelsets are considered as rigid parts (characterized by their mass and pitching moment of inertia), while the vehicle's primary and secondary suspensions are represented by springs and dashpots. The contact stiffness can also be included in the vehicle model, linearized, and represented by springs (and dashpots).

The IC train considered in this section consists of 4 identical vehicles with a length $l_{\mathrm{v}} = 23\,\mathrm{m}$. The vehicle properties are taken from Table 7 in Deliverable D2.1, and are summarized in table 5. The 10-DOF vehicle model (figure 6a) consists of the vehicle body, two bogies, four axles, as well as primary and secondary suspensions. Alternatively, a 4-DOF model (figure 6b) can be used consisting of one bogie and two axles, or each axle can be represented by a 1-DOF model (figure 6c) consisting of only the axle (unsprung) mass.

Table 5: Vehicle properties of the IC train.

Car body	Vehicle length	$l_{\mathrm{v}} = 23$ m
	Mass	$m_{\mathrm{c}} = 32000$ kg
	Pitching moment of inertia	$J_{\mathrm{cx}} = 1.2 \times 10^6$ kgm^2
Bogie	Bogie spacing	$l_{\mathrm{b}} = 17$ m
	Mass	$m_{\mathrm{b}} = 5000$ kg
	Pitching moment of inertia	$J_{\mathrm{bx}} = 6000$ kgm^2
Wheelset (unsprung mass)	Axle spacing	$l_{\mathrm{a}} = 2.5$ m
	Mass	$m_{\mathrm{a}} = 1200$ kg
	Contact stiffness (per wheel)	$k_{\mathrm{H}} = 1.26 \times 10^9$ N/m
Primary suspension	Vertical stiffness per axle	$k_1 = 2 \times 10^6$ N/m
	Vertical viscous damping per axle	$c_1 = 40 \times 10^3$ Ns/m
Secondary suspension	Vertical stiffness per axle	$k_2 = 0.5 \times 10^6$ N/m
	Vertical viscous damping per axle	$c_2 = 31.6 \times 10^3$ Ns/m

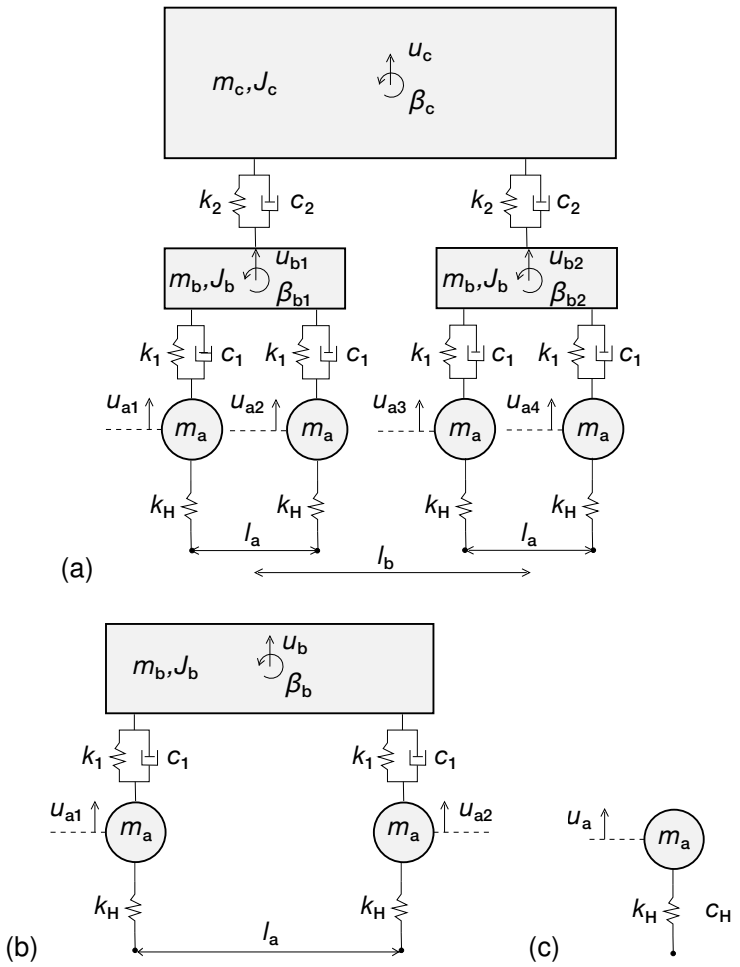

Figure 6: (a) 10-DOF, (b) 4-DOF and (c) 1-DOF vehicle models.

2.7 Comparison for the ballasted track

In the following, a comprehensive comparison between results obtained with TRAFFIC and MOTIV is presented for the ballasted track.

2.7.1 Track, vehicle and total compliance

The vertical component of the track compliance $\hat{\mathbf{C}}^{\mathrm{t}}(\omega)$ is computed in a moving frame of reference. Figure 7 shows the vertical compliance for a load moving at 150 km/h on the ballasted track supported by soft, medium and stiff soils. At low frequencies (below 16 Hz), the track compliance decreases with increasing soil stiffness, while at higher frequencies the track compliance slightly increases. For the medium and stiff soils, a resonance is observed close to 125 Hz due to the flexibility of the ballast layer. The results with TRAFFIC and MOTIV are in excellent agreement. The influence of the load speed on the track compliance is discussed later in section 3.2.

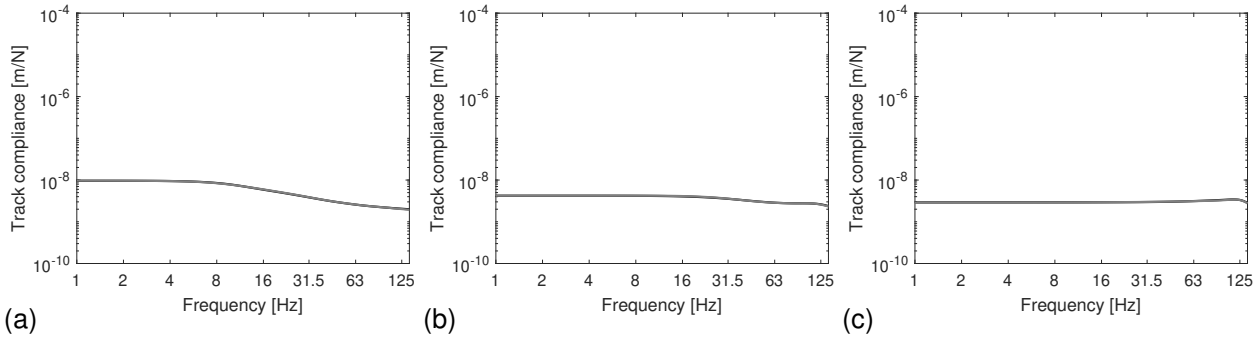

Figure 7: Vertical track compliance $\hat{\mathrm{C}}^{\mathrm{t}}_{11}(\omega)$ for the ballasted track supported by (a) soft, (b) medium and (c) stiff soil for a load moving at 150 km/h. Results are computed with TRAFFIC (black line) and MOTIV (grey line).

The vehicle compliance $\hat{\mathbf{C}}^{\mathrm{v}}(\omega)$ is computed with the 1-DOF model (figure 8a) and 10-DOF model (figures 8b and 8c). Above 10 Hz, the 1-DOF and 10-DOF models show identical results for the compliance $\hat{C}^{\mathrm{v}}_{11}(\omega)$ of the first axle (figures 8a and 8b), since only the axle (unsprung) mass of the vehicle affects the dynamic response of the wheelset. Below 10 Hz, the differences are attributed to the contribution of the bogie and vehicle mass in the 10-DOF model, which are not included in the 1-DOF model. For the 10-DOF model, the peaks around 2 Hz and 8 Hz are related to the resonance frequencies of the sprung masses on the primary and secondary suspensions. Figure 8c shows that the coupling term $\hat{C}^{\mathrm{v}}_{12}(\omega)$ between the first two axles is very low at high frequencies. The results obtained with TRAFFIC and MOTIV are in excellent agreement.

The total compliance $\hat{\mathbf{C}}(\omega) = \hat{\mathbf{C}}^{\mathrm{t}}(\omega) + \hat{\mathbf{C}}^{\mathrm{v}}(\omega)$ is shown in figure 9 for a load moving at 150 km/h. The track and vehicle compliance (computed with the 10-DOF model) are also shown in the figure. At low frequencies, the total compliance is governed by the vehicle compliance. Around 80 Hz, which can be identified as the P2 resonance, the curves for the track and vehicle compliance intersect, and the total compliance is close to its minimum value. At higher frequencies, the total compliance is governed by the track compliance. The results computed with TRAFFIC and MOTIV are in excellent agreement.

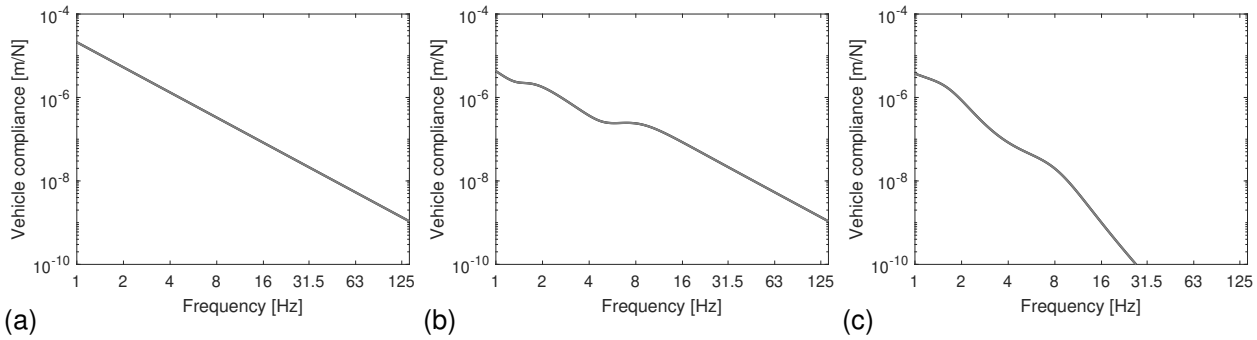

Figure 8: Vehicle compliance (a) $\hat{\mathrm{C}}^{\mathrm{v}}_{11}(\omega)$ for the 1-DOF model, (b) $\hat{\mathrm{C}}^{\mathrm{v}}_{11}(\omega)$ for the 10-DOF model and (c) $\hat{\mathrm{C}}^{\mathrm{v}}_{12}(\omega)$ for the 10-DOF model. Results are computed with TRAFFIC (black line) and MOTIV (grey line).

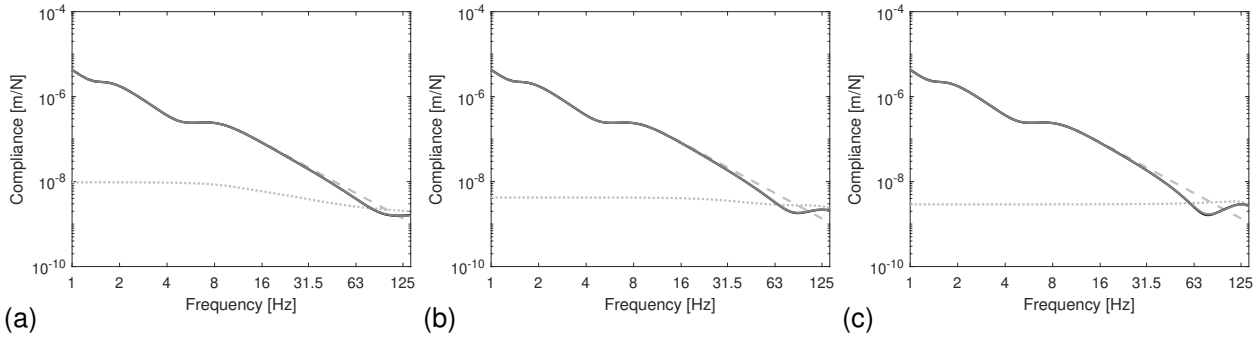

Figure 9: Total compliance $\hat{\mathrm{C}}_{11}(\omega)$ for the ballasted track supported by (a) soft, (b) medium and (c) stiff soil for a load moving at 150 km/h. Results are computed with TRAFFIC (black line) and MOTIV (grey line). The light grey lines correspond to the track (dotted line) and vehicle (dashed line) compliance.

2.7.2 Track response and transfer functions

The vertical sleeper response due to a unit axle load distributed equally to both rails at $y = 0\,\mathrm{m}$ is considered first. Figure 10 shows the sleeper response for the ballasted track on soft, medium and stiff soil. Similar to the track compliance (figure 9), the sleeper response at low frequencies decreases with increasing soil stiffness. A resonance around 125 Hz is observed in the case of medium and stiff soil due to the

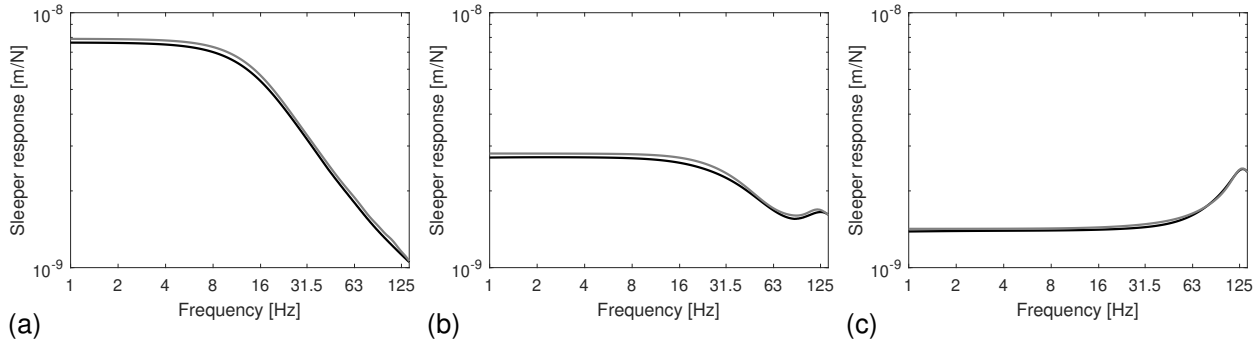

Figure 10: Vertical sleeper response due to a unit axle load for the ballasted track on (a) soft, (b) medium and (c) stiff soil. Results are computed with TRAFFIC (black line) and MOTIV (grey line).

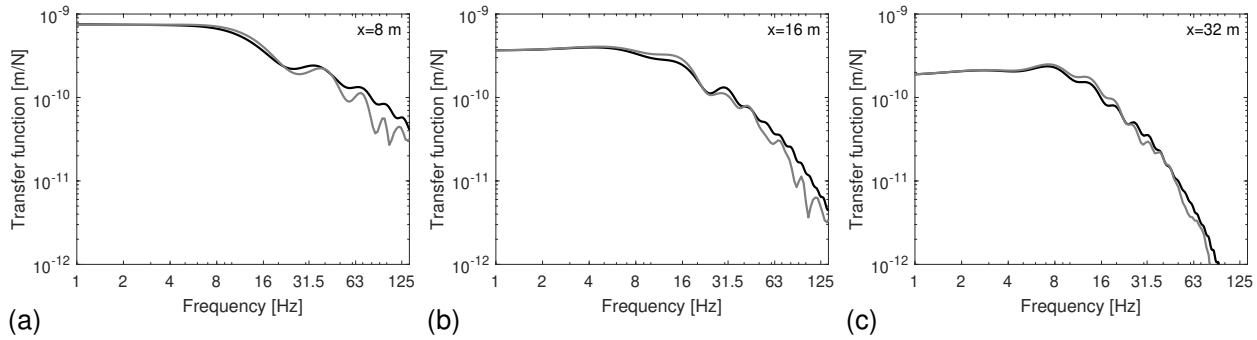

Figure 11: Track-soil transfer function at $y = 0$ m for the ballasted track on soft soil at (a) 8 m, (b) 16 m and (c) 32 m from the track. Results are computed with TRAFFIC (black line) and MOTIV (grey line).

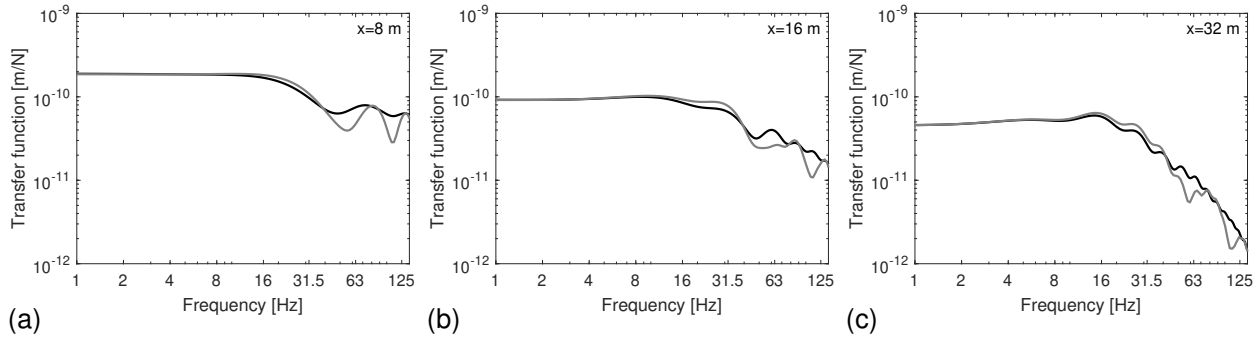

Figure 12: Track-soil transfer function at $y = 0$ m for the ballasted track on medium soil at (a) 8 m, (b) 16 m and (c) 32 m from the track. Results are computed with TRAFFIC (black line) and MOTIV (grey line).

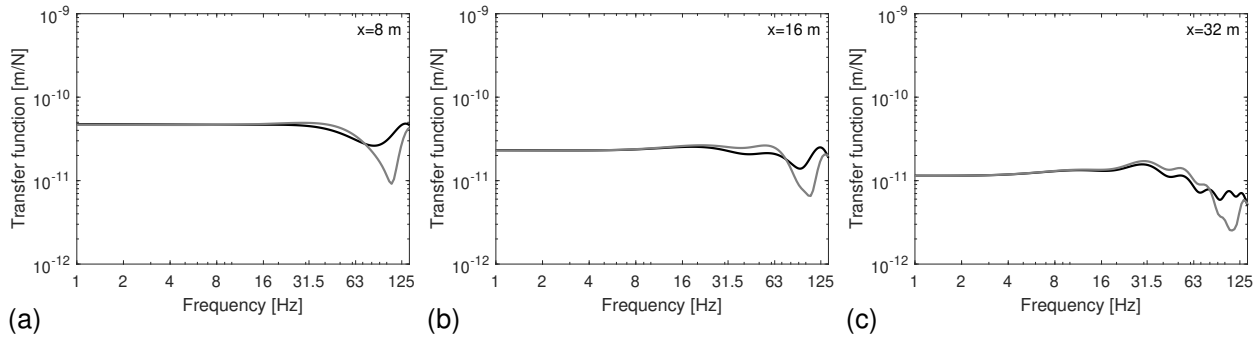

Figure 13: Track-soil transfer function at $y = 0$ m for the ballasted track on stiff soil at (a) 8 m, (b) 16 m and (c) 32 m from the track. Results are computed with TRAFFIC (black line) and MOTIV (grey line).

flexibility of the ballast. The results computed with TRAFFIC and MOTIV are in very good agreement.

Next, the track-soil transfer function $\hat{h}_{zz}(\mathbf{x}_1, \omega)$ is discussed. This is the vertical free field displacement at positions along a line perpendicular to the track at $y = 0$ m due to a unit axle load distributed equally to both rails. Figures 11, 12 and 13 show the track-soil transfer functions at 8 m, 16 m and 32 m from the ballasted track on soft, medium and stiff soil, respectively. At low frequencies, the highest free field response is found for the soft soil, shown in figure 11. The response decreases with increasing distance from the track due to geometrical attenuation in the soil. At high frequencies, the response rapidly attenuates due to material

damping in the soil, and the response is lower for the soft soil compared to the medium and stiff soils, shown in figures 12 and 13, respectively. The oscillations in the transfer functions are related to the width of the track-soil interface relative to the Rayleigh wavelength in the soil; dips appear at $f = kC_\mathrm{R}/b_\mathrm{balb}$ [Hz] for $k = 1, 2, \ldots$. In the MOTIV results, these dips are more prominent and occur at slightly higher frequencies because of the different kinematic assumptions applied at the track-soil interface.

The results computed with TRAFFIC and MOTIV are in excellent agreement up to 30 Hz. At higher frequencies, the different kinematic assumptions made in the two track models lead to some discrepancies in the transfer functions. The discrepancy is largest for receivers close to the track and increases with increasing stiffness of the soil relative to the ballast material. Due to the assumption of a rigid track-soil interface in TRAFFIC, the track-soil transfer function is generally higher compared to MOTIV at high frequencies.

2.7.3 Line source transfer mobility

First, a summary of the computation of the line source transfer mobility is presented. Next, a comparison of results obtained with TRAFFIC and MOTIV is presented.

Computation of the line source transfer mobility

The track-soil transfer function $\hat{h}_{zz}(\mathbf{x}_1, \omega)$ at receiver location $\mathbf{x}_1$ is used to compute the point source transfer mobility $\mathrm{TM_P}(\mathbf{X}_k, \mathbf{x}_1)$ represented in one-third octave bands with centre frequencies ω_j. The modulus of the track-soil mobility $\mathrm{i}\omega\hat{h}_{zz}(\mathbf{x}_1, \omega)$ is averaged in the frequency band $[\omega_{\mathrm{l}j}, \omega_{\mathrm{u}j}]$ with centre frequency ω_j, and the result is expressed in dB with reference velocity v_ref, as follows:

$$\mathrm{TM_P}(\mathbf{X}_k, \mathbf{x}_1) = 20\log_{10}\left(\sqrt{\frac{1}{\omega_{\mathrm{u}j} - \omega_{\mathrm{l}j}}\int_{\omega_{\mathrm{l}j}}^{\omega_{\mathrm{u}j}} |\mathrm{i}\omega\hat{h}_{zz}(\mathbf{x}_1, \omega)|^2 \mathrm{d}\omega} \Big/ v_\mathrm{ref}\right) \tag{9}$$

where $\mathbf{X}_k$ denotes the position of the unit axle load for which the transfer function $\hat{h}_{zz}(\mathbf{x}_1, \omega)$ is computed, and $v_\mathrm{ref} = 5 \times 10^{-8}$ m/s is the reference value for the velocity used within the SILVARSTAR project.

The line source transfer mobility $\mathrm{TM_L}(\mathbf{X}, \mathbf{x}_1)$ at a receiver location $\mathbf{x}_1$ is subsequently computed as a superposition of point source transfer mobilities for n source points $\mathbf{X}_k$ $(k = 1, 2, \ldots, n)$ along the track centred around $y = 0$. These n source points represent the n_a axle positions or $n_\mathrm{b} = n_\mathrm{a}/2$ bogie positions of a train (figures 14a and 14b), but are often considered to be equidistantly spaced along a length L_t (figure 14c). If a fixed spacing $h = L_\mathrm{t}/n$ between the source points is assumed (figure 14d), the line source transfer mobility is calculated as:

$$\mathrm{TM_L}(\mathbf{X}, \mathbf{x}_1) = 10\log_{10}\left[h\sum_{k=1}^{n} 10^{\frac{\mathrm{TM_P}(\mathbf{X}_k, \mathbf{x}_1)}{10}}\right] \tag{10}$$

Alternatively, the contribution of the source points at both ends of the line load can also be weighted by half (figure 14e), so that equation (10) becomes:

$$\mathrm{TM_L}(\mathbf{X}, \mathbf{x}_1) = 10\log_{10}\left[h'\left(\frac{1}{2}10^{\frac{\mathrm{TM_P}(\mathbf{X}_1, \mathbf{x}_1)}{10}} + \sum_{k=2}^{n-1} 10^{\frac{\mathrm{TM_P}(\mathbf{X}_k, \mathbf{x}_1)}{10}} + \frac{1}{2}10^{\frac{\mathrm{TM_P}(\mathbf{X}_n, \mathbf{x}_1)}{10}}\right)\right] \tag{11}$$

where $h' = h\frac{n}{n-1}$. Within the SILVARSTAR project, the line source transfer mobility is computed with equation (11) for $n = 21$ source points and $h' = 10\,\text{m}$, corresponding to a total length of 200 m.

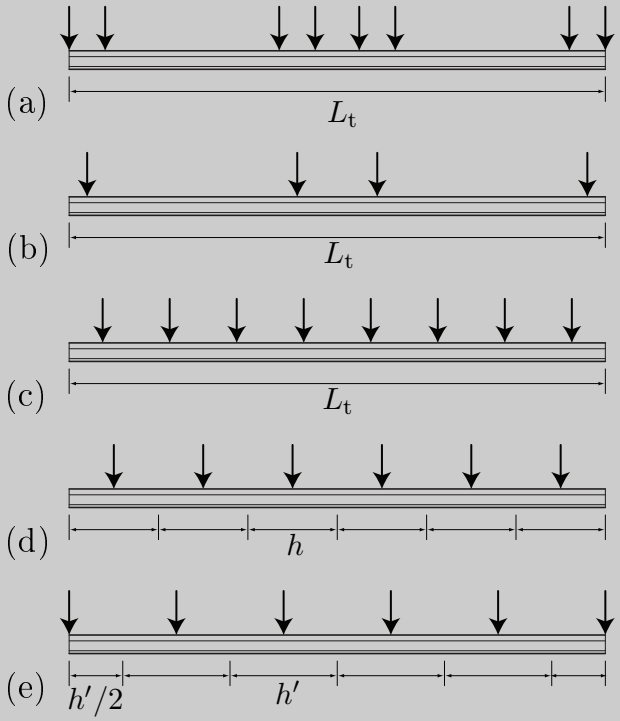

Figure 14: Location of the source points for the determination of the line source transfer mobility $\text{TM}_\text{L}(\mathbf{X}, \mathbf{x}_1)$ with (a) n_a source points corresponding to the axle locations, (b) n_b source points corresponding to the bogie locations, (c) n_a equidistant source points, (d) n equidistant source points with spacing h and (e) n equidistant source points with spacing h' including two edge points.

The location of the source points $\mathbf{X}$ affects the line source transfer mobility $\text{TM}_\text{L}(\mathbf{X}, \mathbf{x}_1)$. Unless otherwise mentioned, source points are considered at both rail heads: a unit load is equally distributed across both rails when computing the transfer functions $\hat{h}_{zz}(\mathbf{x}_1, \omega)$. Alternatively, the source points could be located at one rail, the sleeper centre, or the sleeper edge. The influence of the source positions has been studied by Verbraken [18].

Figure 15 shows the line source transfer mobility for the ballasted track on soft soil. As the track-soil transfer function $\hat{h}_{zz}(\mathbf{x}_1, \omega)$ at $y = 0\,\text{m}$ shown in figure 11 mainly determines the line source transfer mobility, similar observations can be made regarding the influence of geometrical attenuation and material damping. The discrepancy at high frequencies between TRAFFIC and MOTIV is around 5 dB close to the track and 3-5 dB in the far field. The discrepancy is attributed to the different kinematic assumptions at the track-soil interface.

For the medium soil, figure 16 shows that the line source transfer mobility is around 12 dB lower at low frequencies than for the soft soil, but a few dB higher in the 125 Hz frequency band. The discrepancy between results computed with TRAFFIC and MOTIV is limited to between 0 dB and 3 dB in every frequency

band, both close to the track and in the far field.

Figure 17 shows the line source transfer mobility for the stiff soil. At low frequencies, the line source transfer mobility is close to 12 dB lower than for the medium soil. Close to the track, the discrepancy between TRAFFIC and MOTIV is limited to 2 dB, while significant differences were observed in the transfer function at $y = 0$ m (figure 13a). However, the amplitude of the transfer functions at $y = 10, 20, \ldots$ m computed with MOTIV is higher than with TRAFFIC, which compensates for the lower amplitude of the transfer function at $y = 0$ m (figure 13a) when computing the line source transfer mobility. At 16 m and 32 m from the track (figures 17b and 17c), the difference at high frequencies is around 4 dB and 5 dB, respectively.

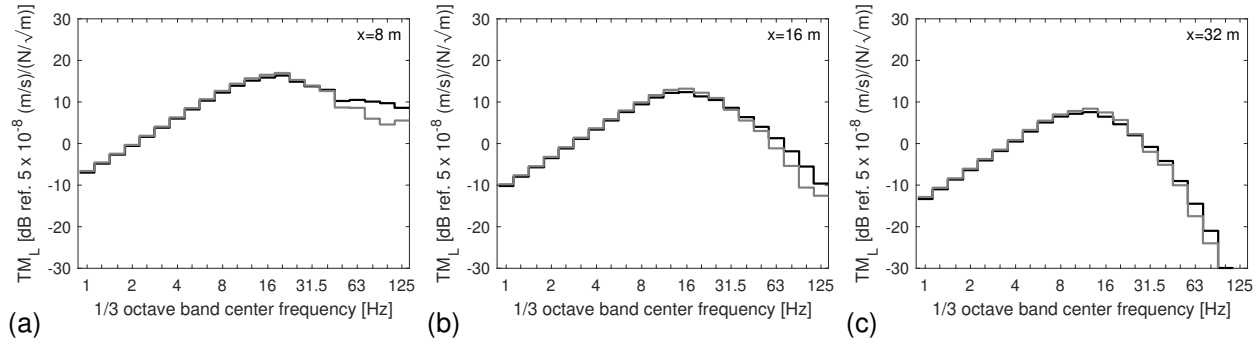

Figure 15: Line source transfer mobility $\mathrm{TM_L}(\mathbf{X}, \mathbf{x}_1)$ of the ballasted track supported by soft soil for receivers at (a) 8 m, (b) 16 m and (c) 32 m from the track. Results are computed with TRAFFIC (black line) and MOTIV (grey line).

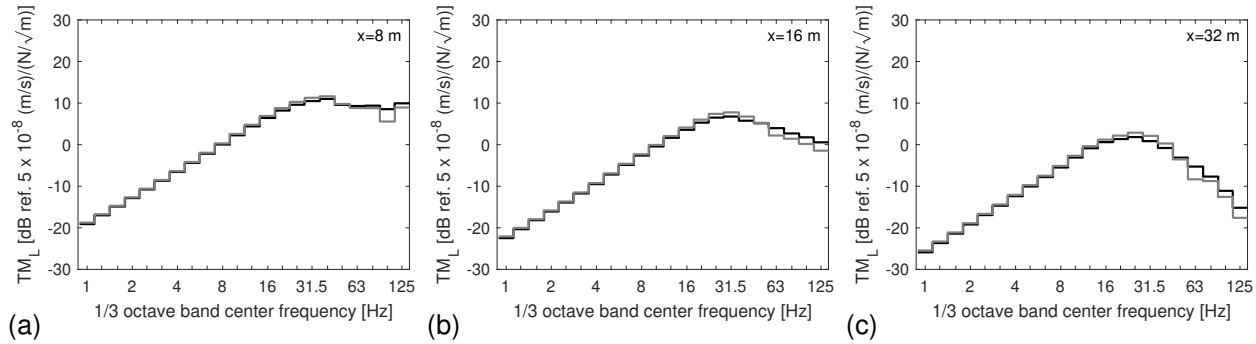

Figure 16: Line source transfer mobility $\mathrm{TM_L}(\mathbf{X}, \mathbf{x}_1)$ of the ballasted track supported by medium soil for receivers at (a) 8 m, (b) 16 m and (c) 32 m from the track. Results are computed with TRAFFIC (black line) and MOTIV (grey line).

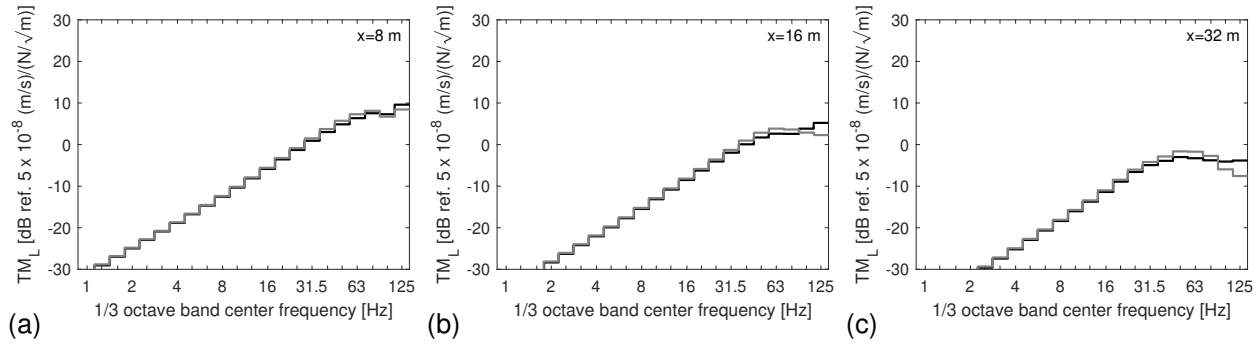

Figure 17: Line source transfer mobility $\mathrm{TM_L}(\mathbf{X}, \mathbf{x}_1)$ of the ballasted track supported by stiff soil for receivers at (a) 8 m, (b) 16 m and (c) 32 m from the track. Results are computed with TRAFFIC (black line) and MOTIV (grey line).

2.7.4 Dynamic axle loads

First, the dynamic axle loads are computed using equation (7) for the case of unit track unevenness by setting the term $\frac{1}{v}\tilde{u}_{\mathrm{rz}}\left(-\frac{\omega}{v}\right)$ in equation (4) equal to unity for each frequency ω. The vehicle compliance is computed with the 10-DOF model, and the track compliance is evaluated in the moving frame of reference.

Figure 18 shows the first axle load of the IC train running on the ballasted track on soft soil. Three train speeds are considered: 50 km/h, 150 km/h and 300 km/h. As unit unevenness is considered, the amplitude of the dynamic axle load is not affected by the train speed. Peaks are observed in the dynamic axle load at multiples of the axle passage frequency $f_{\mathrm{a}} = v/l_{\mathrm{a}}$ (see table 6 for an overview of the quasi-static excitation components).

Table 6: Quasi-static excitation components for the IC train running at different speeds.

Speed [km/h]	50	150	300
Axle passage frequency $f_{\mathrm{a}} = v/l_{\mathrm{a}}$ [Hz]	5.6	16.7	33.3
Bogie passage frequency $f_{\mathrm{b}} = v/l_{\mathrm{b}}$ [Hz]	0.8	2.5	4.9
Vehicle passage frequency $f_{\mathrm{v}} = v/l_{\mathrm{v}}$ [Hz]	0.6	1.8	3.6

Figure 19 shows the dynamic axle load for the track on medium soil. The maximum amplitude of the load is reached around 80 Hz, which corresponds to the P2 resonance (minimum in the total compliance in figure 9). Besides peaks at multiples of the axle passage frequency f_{a}, smaller peaks are identified below 100 Hz at multiples of the vehicle passage frequency $f_{\mathrm{v}} = v/l_{\mathrm{b}}$ [11]. Due to the higher soil stiffness, the contribution of the coupling terms in the track compliance matrix increases. This explains why the peaks at multiples of the vehicle passage frequency f_{v} were not visible for the soft soil.

For the stiff soil, figure 20 clearly shows the P2 resonance around 80 Hz. The maximum amplitude of the dynamic axle load is also higher than for the medium and soft soil. Peaks are observed at multiples of f_{a} and f_{v} in the entire frequency range. The results computed with TRAFFIC and MOTIV are in very good agreement, which was also the case for the soft (figure 18) and medium (figure 19) soil.

Next, a track unevenness profile is generated from the PSD given by the FRA (class 6 track quality, figure 4) using equation (6). The dynamic axle loads for unit unevenness are multiplied with the frequency content of the generated unevenness profile.

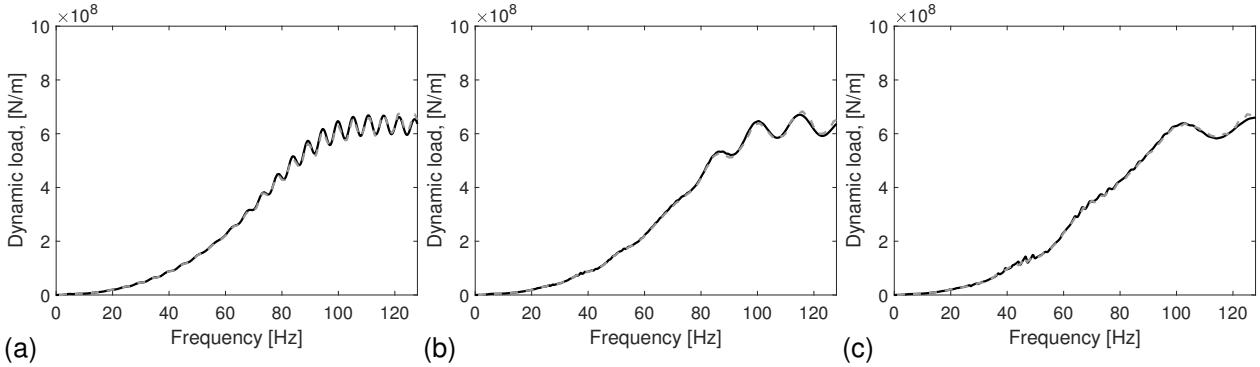

Figure 18: First dynamic axle load of the IC train running at (a) 50 km/h, (b) 150 km/h and (c) 300 km/h on the ballasted track supported by soft soil. Results are computed with TRAFFIC (black solid line) and MOTIV (grey dashed line) for unit track unevenness.

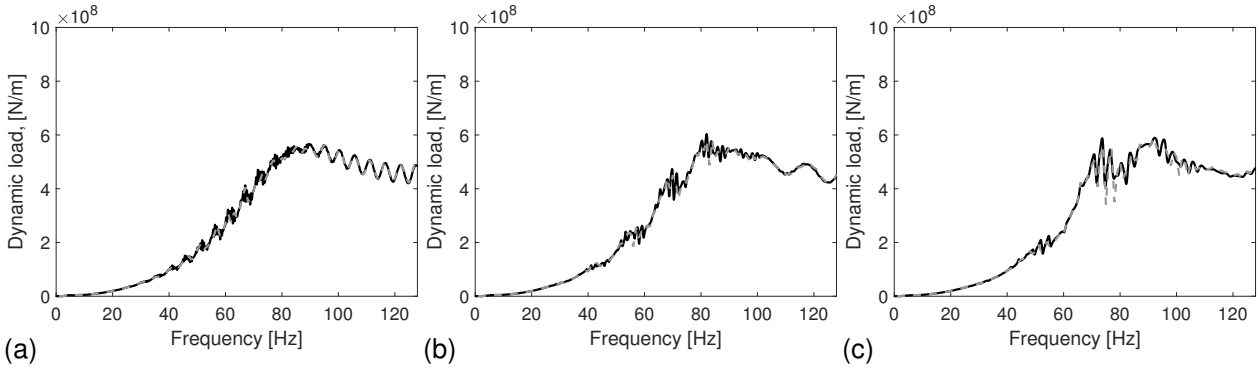

Figure 19: First dynamic axle load of the IC train running at (a) 50 km/h, (b) 150 km/h and (c) 300 km/h on the ballasted track supported by medium soil. Results are computed with TRAFFIC (black solid line) and MOTIV (grey dashed line) for unit track unevenness.

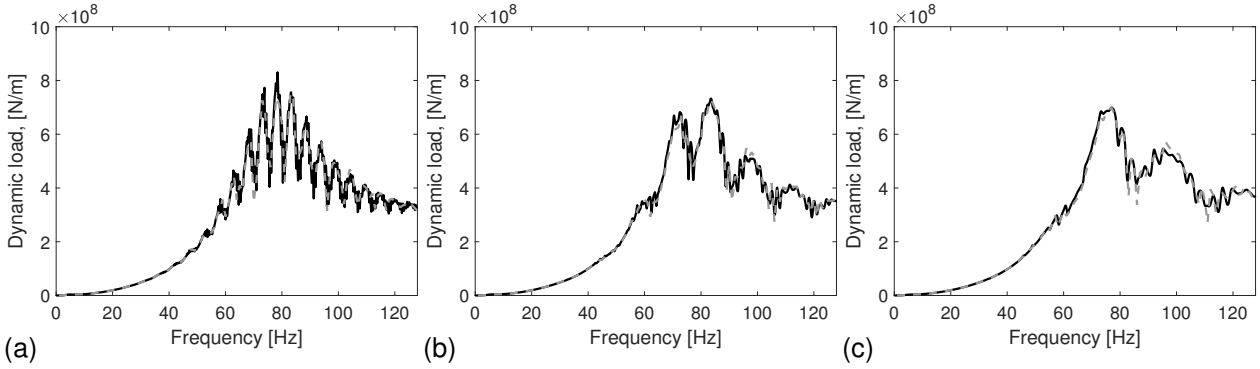

Figure 20: First dynamic axle load of the IC train running at (a) 50 km/h, (b) 150 km/h and (c) 300 km/h on the ballasted track supported by stiff soil. Results are computed with TRAFFIC (black solid line) and MOTIV (grey dashed line) for unit track unevenness.

Figure 21 shows the first dynamic axle load of the IC train running on the ballasted track on soft soil. For a train speed of 50 km/h, the perceived unevenness in the frequency range between 1 and 125 Hz corresponds to the wavenumber range k_y between 0.07 rad/m and 9 rad/m, for which the amplitude of the track unevenness is relatively low (figure 4). For higher train speeds, excitation between 1 Hz and 125 Hz corresponds to lower wavenumbers, and consequently, the dynamic axle loads are higher.

The effect of increasing soil stiffness is presented in figures 22 (medium soil) and 23 (stiff soil). Around the P2 resonance at 80 Hz, the dynamic axle load increases with increasing soil stiffness. This is best observed for a train speed of 300 km/h.

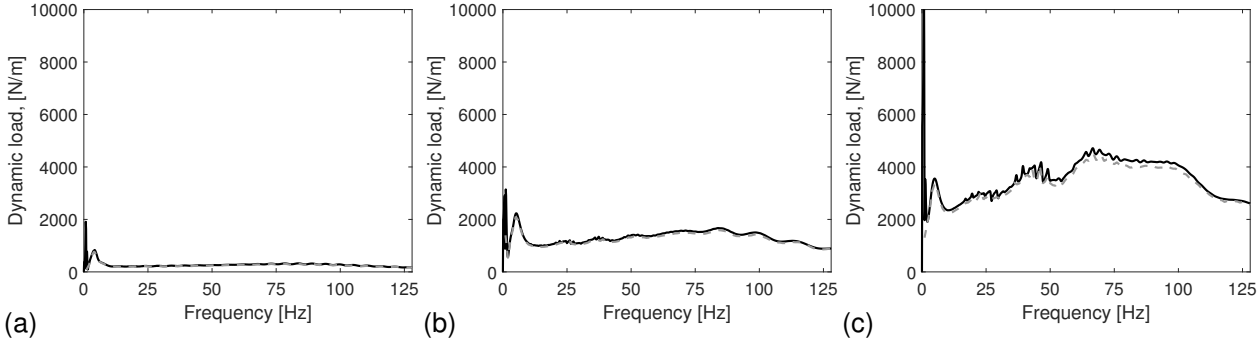

Figure 21: First dynamic axle load of the IC train running at (a) 50 km/h, (b) 150 km/h and (c) 300 km/h on the ballasted track supported by soft soil. Results are computed with TRAFFIC (black solid line) and MOTIV (grey dashed line) with track unevenness according to FRA class 6.

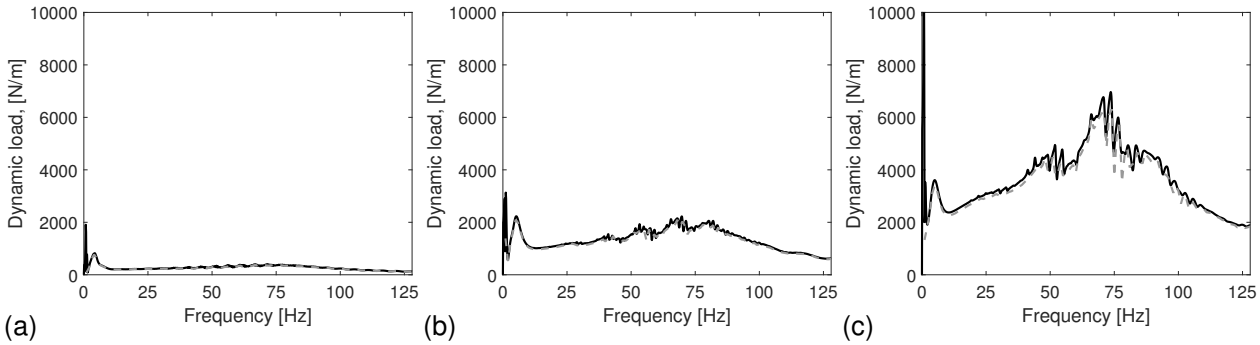

Figure 22: First dynamic axle load of the IC train running at (a) 50 km/h, (b) 150 km/h and (c) 300 km/h on the ballasted track supported by medium soil. Results are computed with TRAFFIC (black solid line) and MOTIV (grey dashed line) with track unevenness according to FRA class 6.

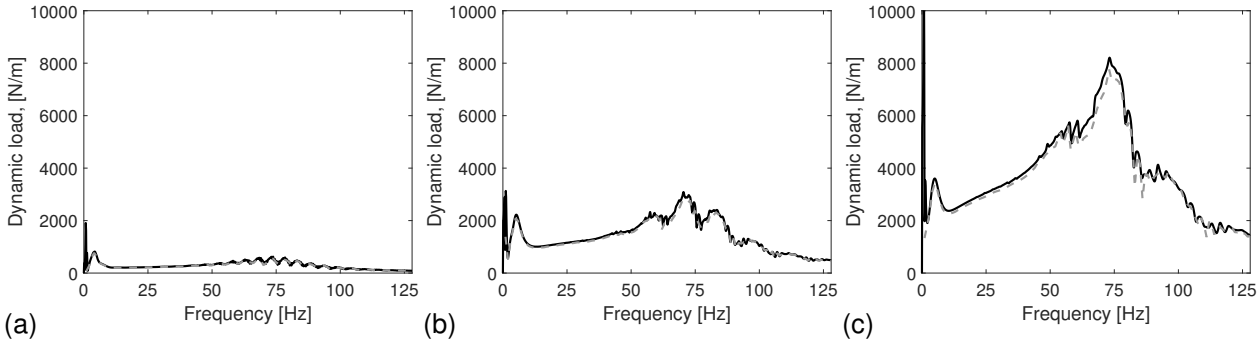

Figure 23: First dynamic axle load of the IC train running at (a) 50 km/h, (b) 150 km/h and (c) 300 km/h on the ballasted track supported by stiff soil. Results are computed with TRAFFIC (black solid line) and MOTIV (grey dashed line) with track unevenness according to FRA class 6.

2.7.5 Vibration velocity level

First, a summary is given on the computation of the vibration velocity level in TRAFFIC and MOTIV. Next, the vibration velocity level predicted with TRAFFIC and MOTIV is compared for the ballasted track.

Computation of the vibration velocity level in TRAFFIC

The free field vibration velocity level $\mathrm{L_v}(\mathbf{x}_1)$ [dB] is computed from the vertical RMS velocity $\hat{v}_{z\mathrm{RMS}}(\mathbf{x}_1)$ in one-third octave bands as:

$$\mathrm{L_v}(\mathbf{x}_1) \quad = \quad 20\log_{10}(\hat{v}_{z\mathrm{RMS}}(\mathbf{x}_1)) - 20\log_{10}(v_{\mathrm{ref}}) \tag{12}$$

The RMS velocity $\hat{v}_{z\mathrm{RMS}}(\mathbf{x}_1)$ [m/s] is computed according to the German standard DIN 45672-2 [3] for a reference period T_2. This period T_2 is the duration of the stationary part of the time history $v_z(\mathbf{x}_1, t)$ [m/s] obtained as the inverse Fourier transform of the velocity $\hat{v}_z(\mathbf{x}_1, \omega)$ [(m/s)/Hz]. In paragraph 3.3.3 of Deliverable D1.1, it was illustrated that the vertical velocity $\hat{v}_z(\mathbf{x}_1, \omega)$ is computed from the track-soil transfer function $\tilde{h}_{zz}(x, k_y, \omega)$ in the frequency-wavenumber domain and the dynamic axle loads $\hat{g}_{\mathrm{d}kz}(\omega)$:

$$\hat{v}_z(x, y, \omega) \quad = \quad \sum_{k=1}^{n_\mathrm{a}} \frac{1}{2\pi} \int_{-\infty}^{+\infty} \mathrm{i}\omega \tilde{h}_{zz}\left(x, k_y, \omega\right) \exp\left[-\mathrm{i}k_y(y - y_{k0})\right] \hat{g}_{\mathrm{d}kz}(\omega - k_y v)\mathrm{d}k_y \tag{13}$$

or, alternatively, by substituting $\tilde{\omega} = \omega - k_y v$:

$$\hat{v}_z(x, y, \omega) \quad = \quad \sum_{k=1}^{n_\mathrm{a}} \frac{1}{2\pi v} \int_{-\infty}^{+\infty} \mathrm{i}\omega \tilde{h}_{zz}\left(x, \frac{\omega - \tilde{\omega}}{v}, \omega\right) \exp\left[-\mathrm{i}\frac{\omega - \tilde{\omega}}{v}(y - y_{k0})\right] \hat{g}_{\mathrm{d}kz}(\tilde{\omega})\mathrm{d}\tilde{\omega} \tag{14}$$

where $\tilde{\omega}$ is the frequency content of the dynamic axle loads, which is shifted with respect to the frequency content ω of the receiver due to the Doppler effect. The explicit dependence of variables on the

z-coordinate is omitted from the notation. The time history $v_z(x, y, t)$ of the velocity is obtained as the inverse Fourier transform of $\hat{v}_z(x, y, \omega)$.

The transfer function $\tilde{h}_{zz}(x, k_y, \omega)$ is deterministic, but the axle loads $\hat{g}_{\mathrm{d}kz}(\omega)$ are determined by the randomly generated track unevenness profile through equation (7). Hence, the vibration velocity level $\mathrm{L_v}(\mathbf{x}_1)$ is different for each realization of the track unevenness. For this reason, the ensemble average of the vibration velocity level is calculated instead, which is the average vibration velocity level for multiple realizations of the track unevenness. Lombaert et al. [10] presented a statistical procedure to directly obtain the ensemble average of the vibration velocity level from the PSD $\hat{\mathbf{S}}_{\mathbf{g}}(\omega)$ of the dynamic axle loads. First, the power spectrum $\hat{S}_{\mathrm{d}zz}(x, y, \omega)$ [(m/s)^2/Hz^2] of the dynamic contribution to the free field velocity is computed as:

$$\hat{S}_{\mathrm{d}zz}(x, y, \omega) = \int_{-\infty}^{+\infty} \sum_{k=1}^{n_\mathrm{a}} \sum_{l=1}^{n_\mathrm{a}} \left[\hat{V}_{zz}(x, y - y_{k0}, \omega, \tilde{\omega}) \otimes \hat{V}^*_{zz}(y - y_{l0}, \omega, \tilde{\omega}) \right] : \hat{S}_{\mathrm{g}kl}(\tilde{\omega}) \mathrm{d}\tilde{\omega} \tag{15}$$

where

$$\hat{V}_{zz}(x, y - y_{k0}, \omega, \tilde{\omega}) = \frac{1}{v} \mathrm{i}\omega \tilde{h}_{zz} \left(x, \frac{\omega - \tilde{\omega}}{v}, \omega \right) \exp \left[-\mathrm{i} \frac{\omega - \tilde{\omega}}{v} (y - y_{k0}) \right] \tag{16}$$

The RMS velocity $\hat{v}_{z\mathrm{RMS}}(\mathbf{x}_1)$ in one-third octave bands with centre frequency ω_j is subsequently obtained as:

$$\hat{v}_{z\mathrm{RMS}}(\mathbf{x}_1, \omega_j) = \frac{1}{\sqrt{T_2}} \int_{\omega_{\mathrm{l}j}}^{\omega_{\mathrm{u}j}} \sqrt{\hat{S}_{\mathrm{d}zz}(\mathbf{x}_1, \omega)} \mathrm{d}\omega \tag{17}$$

This procedure is illustrated by computing the time history (figure 24) and frequency content (figure 25) of the free field velocity at 8 m, 16 m and 32 m from the ballasted track on medium soil for the IC train running at 150 km/h (note: the contribution of the quasi-static axle loads to the vibration velocity level is not accounted for).

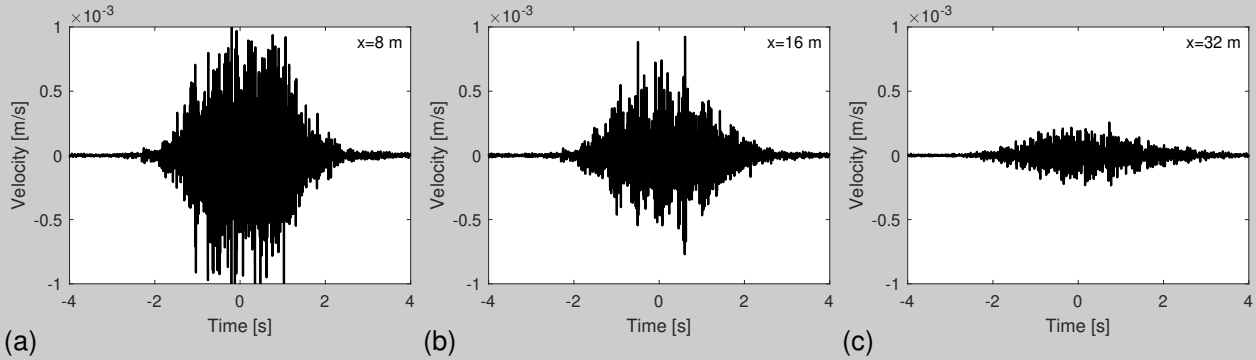

Figure 24: Time history $v_z(\mathbf{x}_1, t)$ of the free field velocity during the passage of the IC train running at 150 km/h on the ballasted track supported by medium soil. Receivers are located at (a) 8 m, (b) 16 m and (c) 32 m from the track. Results are computed with TRAFFIC for one realization of the track unevenness according to FRA class 6.

The time history is characterized by an increasing response when the train approaches, a nearly stationary response during the passage of the train, and a decreasing response after the train has passed. The passage of individual axles or bogies cannot be observed. The frequency content is characterized by peaks at multiples of the axle and vehicle passage frequencies f_{a} and f_{v}, respectively.

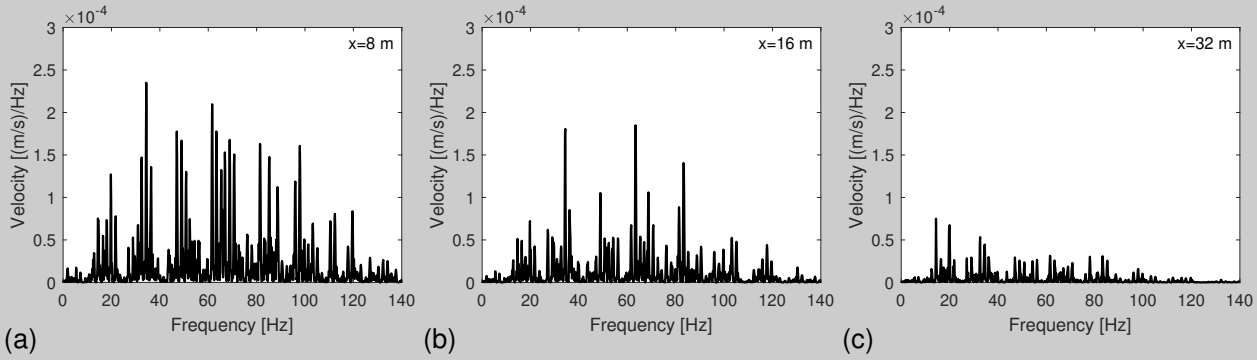

Figure 25: Frequency content $\hat{v}_z(\mathbf{x}_1, \omega)$ of the free field velocity during the passage of the IC train running at 150 km/h on the ballasted track supported by medium soil. Receivers are located at (a) 8 m, (b) 16 m and (c) 32 m from the track. Results are computed with TRAFFIC for one realization of the track unevenness according to FRA class 6.

The computations are repeated for 10 realizations of the track unevenness. Figure 26 shows the running RMS velocity averaged in a 1 s time window for each realization of the track unevenness, as well as the average running RMS velocity. The amplitude of the RMS velocity varies considerably depending on the randomly generated track unevenness: at 8 m from the track, differences up to a factor 1.5 are observed. The running RMS velocity is used to estimate the time period T_2 [3] during which the response is nearly stationary; this is illustrated by the blue line in the figures which shows that T_2 varies between 3.1 s at $x = 8$ m and 4.6 s at $x = 32$ m.

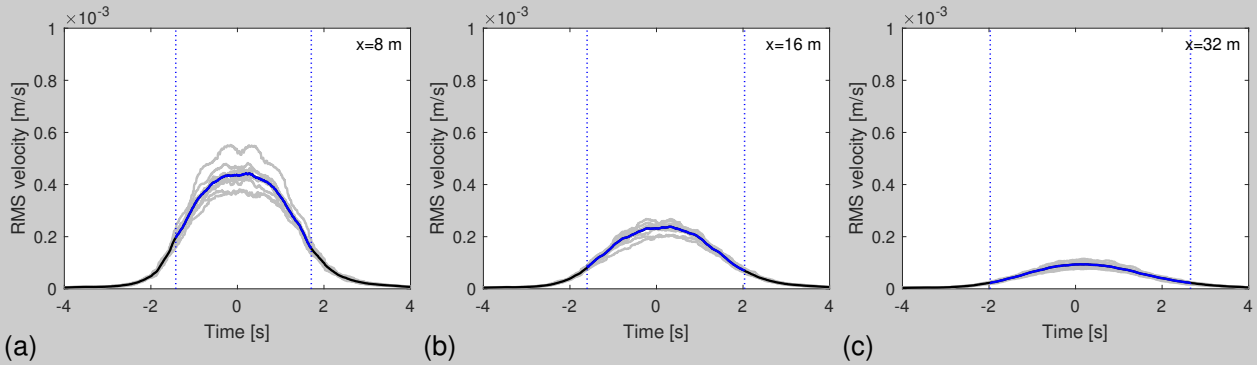

Figure 26: Running RMS velocity $v_{z\mathrm{RMS}}(\mathbf{x}_1, t)$ during the passage of the IC train running at 150 km/h on the ballasted track supported by medium soil. Receivers are located at (a) 8 m, (b) 16 m and (c) 32 m from the track. Results are computed with TRAFFIC for 10 realizations of the track unevenness (light grey lines). The average RMS velocity is indicated by the black line, and the time period T_2 is indicated by the superimposed blue line; the beginning and end of the time period T_2 is marked by the dotted blue lines.

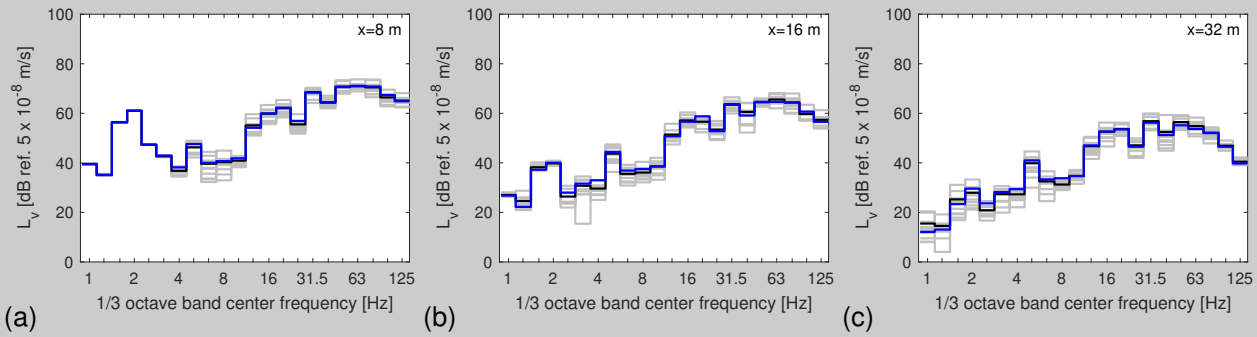

Figure 27: Vibration velocity level $\mathrm{L_v}(\mathbf{x}_1)$ during the passage of the IC train running at 150 km/h on the ballasted track supported by medium soil. Receivers are located at (a) 8 m, (b) 16 m and (c) 32 m from the track. Results are computed with TRAFFIC for 10 realizations of the track unevenness (light grey lines). The average vibration velocity level (black line) and the ensemble average (blue line) computed with the statistical procedure are also shown.

The vibration velocity level is subsequently computed using equation (12) for each realization of the track unevenness; the RMS velocity $\hat{v}_{z\mathrm{RMS}}(\mathbf{x}_1)$ is calculated from the time history $v_z(\mathbf{x}_1, t)$ during the time period T_2. The average vibration velocity level is computed for the 10 realizations of the track unevenness and compared to the ensemble average obtained from the power spectrum $\hat{S}_{\mathrm{d}zz}(\mathbf{x}_1, \omega)$ in equation (15). These results are summarized in figure 27, where the quasi-static contribution to the response is included (it is not affected by the track unevenness). The ensemble average and the average vibration velocity level for the 10 realizations are in very good agreement. Note, however, that the computation of the ensemble average with the statistical procedure takes as long as the computation of the vibration level for a single realization of the track unevenness. In the following, the ensemble average is therefore computed with the statistical procedure.

Computation of the vibration velocity level in MOTIV

In an alternative but broadly equivalent approach, MOTIV computes the vibration velocity level $\mathrm{L_v}(\mathbf{x}_1)$ with equation (12) using the velocity power spectral density of the ground calculated according to the formulation in [15]. At distance x from the track and for a train speed v, this results in:

$$\hat{S}_{\mathrm{d}zz}(x,\omega) = \frac{1}{2T_2}\sum_{m=1}^{n}\left[\left|\mathrm{i}\omega\tilde{u}^0_{zz}(x,\omega,\tilde{\omega}_m)\right|^2 + \left|\mathrm{i}\omega\tilde{u}^0_{zz}(x,\omega,-\tilde{\omega}_m)\right|^2\right]\tilde{S}_{\mathrm{r}zz}\left(\frac{|\tilde{\omega}_m|}{v}\right)\frac{\Delta\tilde{\omega}_m}{v} \tag{18}$$

where $\omega = \tilde{\omega}_m - k_y v$ is the receiver frequency accounting for the Doppler effect and $\tilde{\omega}_m$ is the excitation frequency due to the track unevenness of wavelength $\lambda_m = \frac{2\pi}{k_{ym}}$. The period T_2 is derived from the length of the train and the speed v. In equation (18), $\tilde{u}^0_{zz}(x,\omega,\tilde{\omega}_m)$ is the transfer function of the ground displacement:

$$\tilde{u}^0_{zz}(x,\omega,\tilde{\omega}_m) = \tilde{h}_{zz}(x,\omega,\tilde{\omega}_m)\sum_{k=1}^{n_\mathrm{a}}\hat{g}^0_{\mathrm{d}kz}(\tilde{\omega}_m)\exp\left[-\mathrm{i}\frac{\tilde{\omega}_m-\omega}{v}y_{k0}\right] \tag{19}$$

for dynamic loads $\hat{g}^0_{\mathrm{d}kz}(\tilde{\omega}_m)$ of unit amplitude unevenness $\frac{1}{v}\tilde{u}_{\mathrm{r}z}\left(-\frac{\tilde{\omega}_m}{v}\right) = 1$ calculated using equations (4) and (7) for $m = 1, \ldots, n$.

Figure 28 shows the comparison of the vibration velocity level $L_{\mathrm{v}}(\mathbf{x}_1)$ computed with TRAFFIC and MOTIV for the ballasted track on soft soil. The contribution of the quasi-static axle loads is accounted for. For a train speed of 50 km/h, the quasi-static contribution dominates the response close to the track at low frequencies. A peak is observed at the axle passage frequency f_{a} around 5.5 Hz. At high frequencies, the vibration velocity level predicted with TRAFFIC is higher than with MOTIV. This is due to the kinematic assumptions at the track-soil interface, and the observation is consistent with earlier observations for the transfer functions in figure 11 and line source transfer mobility in figure 15.

For a train speed of 150 km/h, the axle passage frequency increases to 16.6 Hz, where the vibration velocity level shows a peak. The vehicle passing frequency f_{v} is 1.8 Hz which explains the peak at low frequencies. At 300 km/h, the axle and vehicle passage frequencies are close to 33.3 Hz and 3.6 Hz, respectively (table 6). For both train speeds, the predicted vibration velocity level with MOTIV is lower than with TRAFFIC at high frequencies. Overall, results computed with TRAFFIC and MOTIV are in good agreement with differences up to 5 dB in most frequency bands.

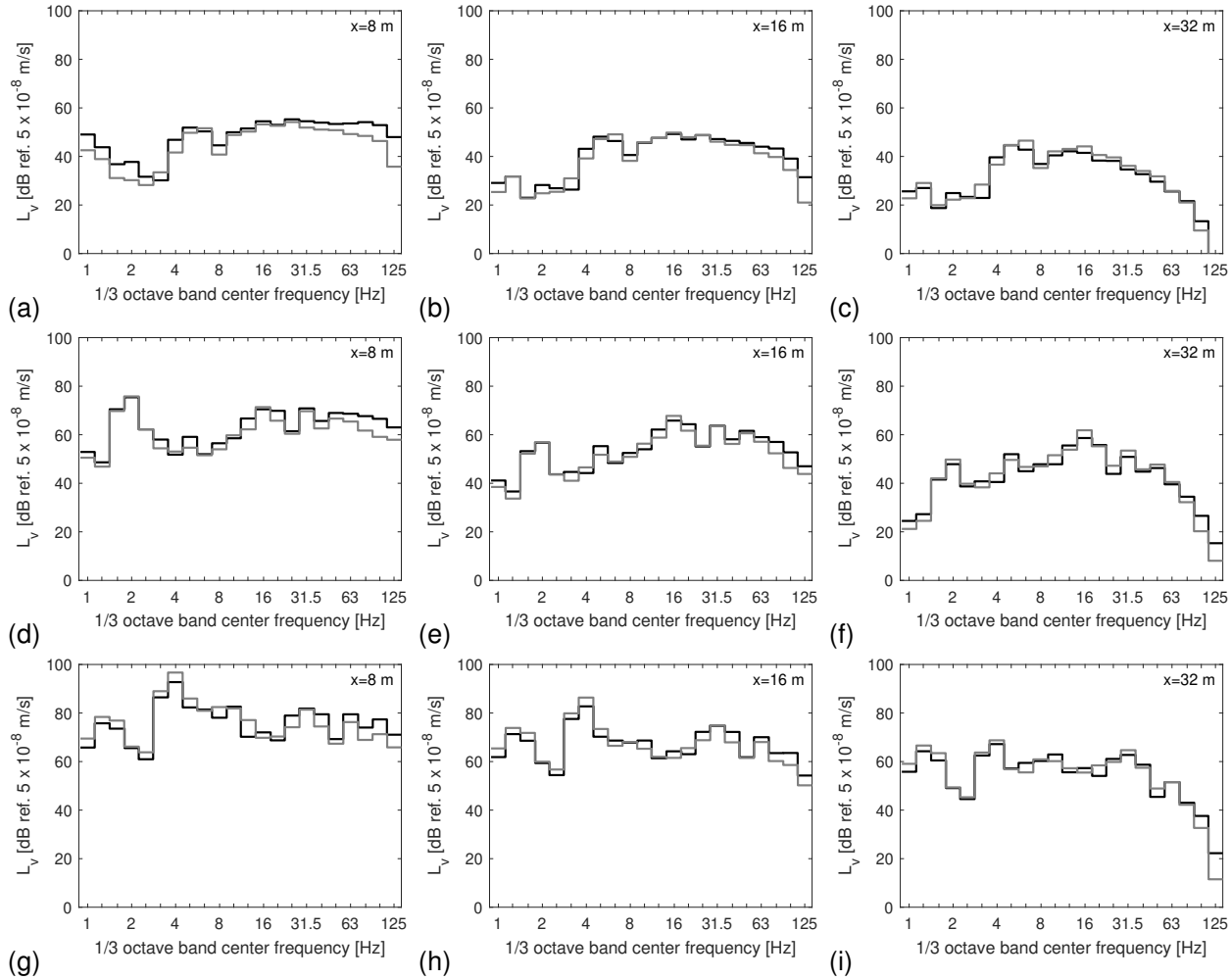

Figure 28: Vibration velocity level $\mathrm{L_v}(\mathbf{x}_1)$ during the passage of the IC train running at (a-c) 50 km/h, (d-f) 150 km/h and (g-i) 300 km/h on the ballasted track supported by soft soil. Receivers are located at (a,d,g) 8 m, (b,e,h) 16 m and (c,f,i) 32 m from the track. Results are computed with TRAFFIC (black line) and MOTIV (grey line).

Figure 29 shows the vibration velocity level for the ballasted track on medium soil. The response is characterized by the axle and vehicle passage frequencies, as discussed earlier for the soft soil. The vibration velocity level increases with increasing train speed for every receiver distance. The discrepancy between results computed with TRAFFIC and MOTIV is particularly evident for a train speed of 50 km/h; the discrepancy reduces at higher speeds. Overall, the predictions with the two models are in good agreement.

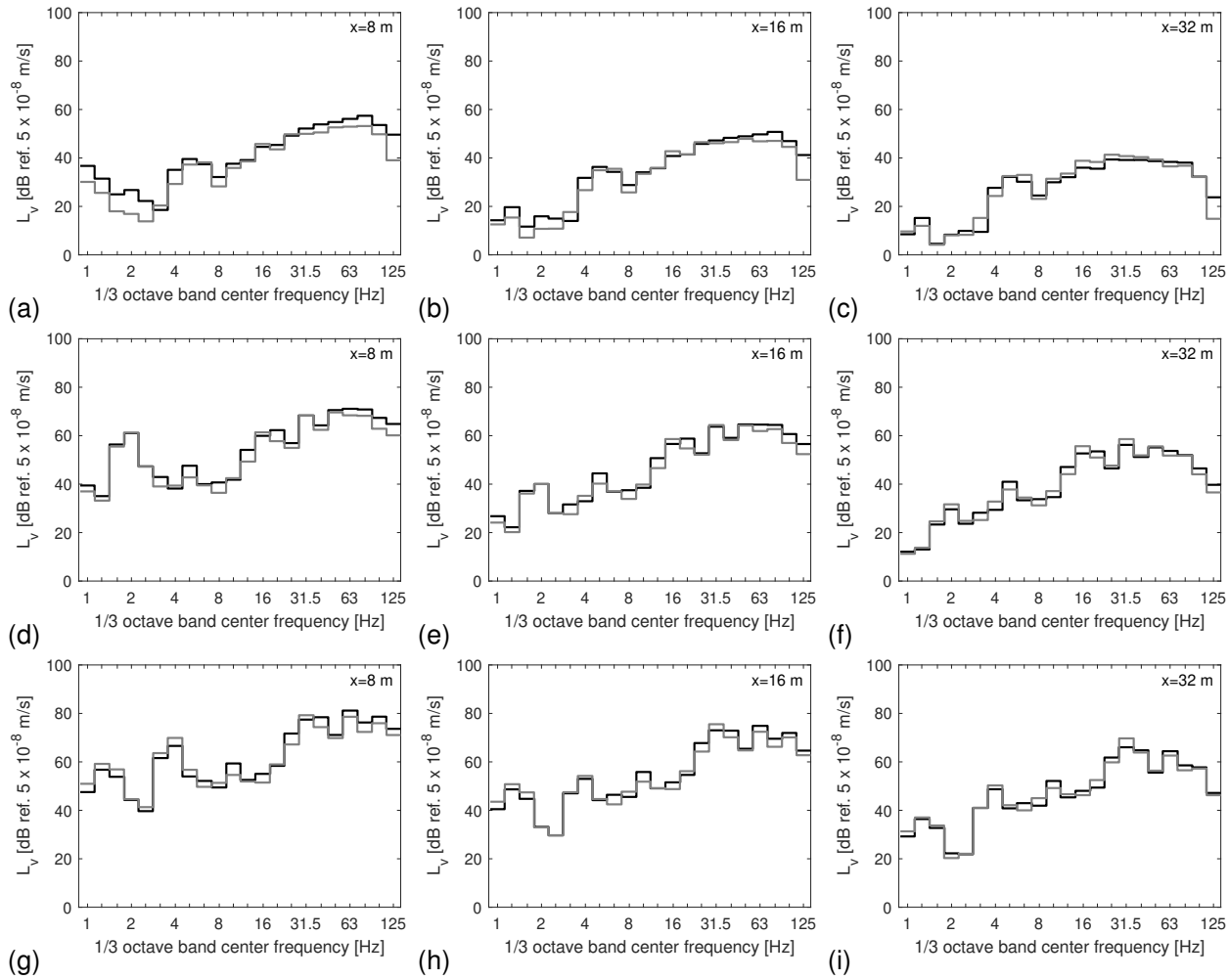

Figure 29: Vibration velocity level $\mathrm{L_v}(\mathbf{x}_1)$ during the passage of the IC train running at (a-c) 50 km/h, (d-f) 150 km/h and (g-i) 300 km/h on the ballasted track supported by medium soil. Receivers are located at (a,d,g) 8 m, (b,e,h) 16 m and (c,f,i) 32 m from the track. Results are computed with TRAFFIC (black line) and MOTIV (grey line).

Figure 30 shows the vibration velocity level for the ballasted track on stiff soil. The P2 resonance around 80 Hz is clearly observed in the response; around this frequency, the dynamic axle loads reach their maximum values (figure 23). For a train speed of 50 km/h, a discrepancy of 10 dB is observed at high frequencies between results obtained with TRAFFIC and MOTIV, which is consistent with observations for the soft and medium soil. The discrepancy reduces to a few dB for higher train speeds.

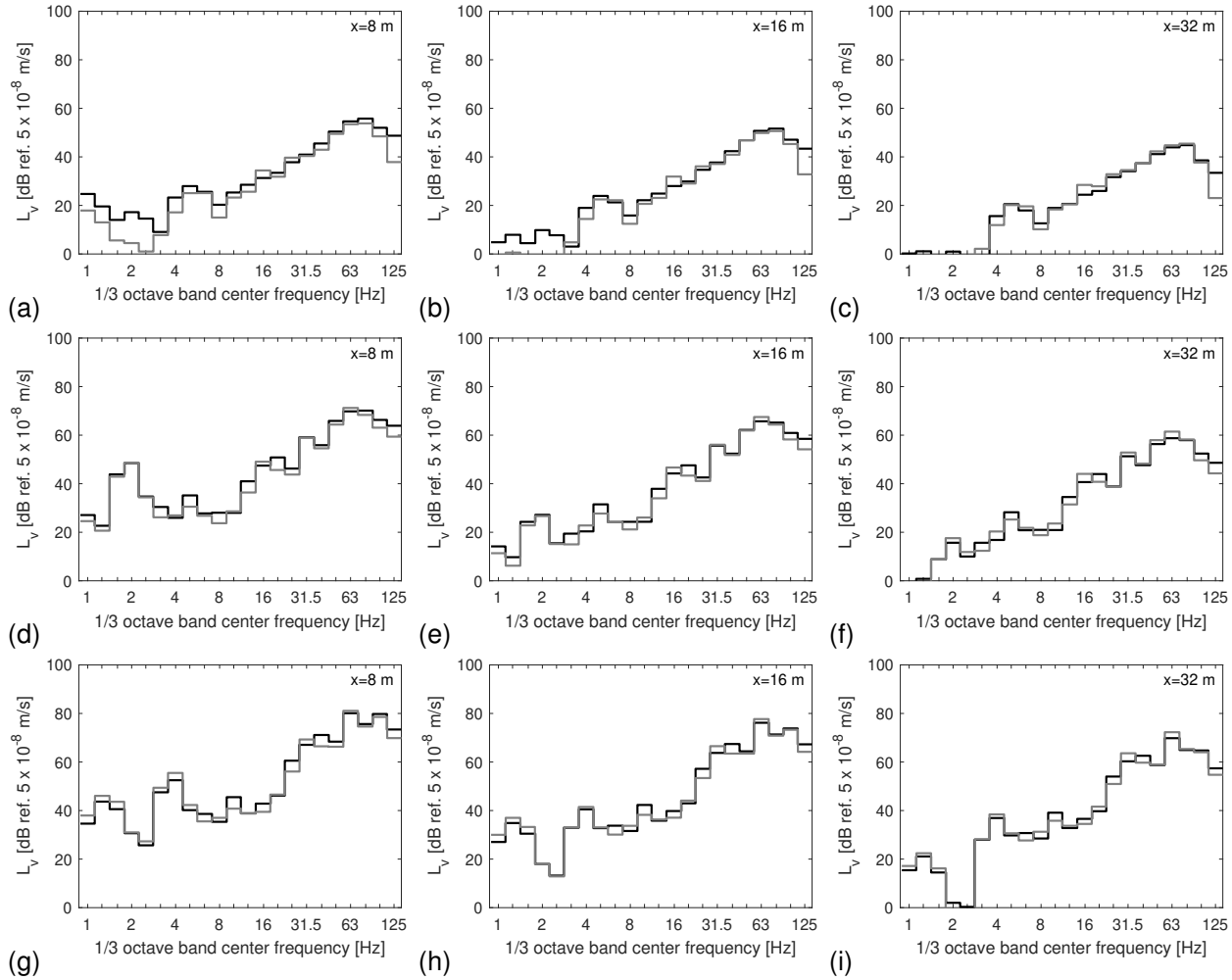

Figure 30: Vibration velocity level $\mathrm{L_v}(\mathbf{x}_1)$ during the passage of the IC train running at (a-c) 50 km/h, (d-f) 150 km/h and (g-i) 300 km/h on the ballasted track supported by stiff soil. Receivers are located at (a,d,g) 8 m, (b,e,h) 16 m and (c,f,i) 32 m from the track. Results are computed with TRAFFIC (black line) and MOTIV (grey line).

2.7.6 Force density

First, a summary is given on the computation of the force density. Subsequently, a comparison between results computed with TRAFFIC and MOTIV is presented.

Computation of the force density

Following the FRA procedure, the force density $\mathrm{L_F}(\mathbf{X}, \mathbf{x}_1)$ is estimated from the vibration velocity level $\mathrm{L_v}(\mathbf{x}_1)$ and the line source transfer mobility $\mathrm{TM_L}(\mathbf{X}, \mathbf{x}_1)$:

$$\mathrm{L_F}(\mathbf{X}, \mathbf{x}_1) \quad = \quad \mathrm{L_v}(\mathbf{x}_1) - \mathrm{TM_L}(\mathbf{X}, \mathbf{x}_1) \tag{20}$$

This excitation force term represents the equivalent fixed incoherent line source that results in the same vibration velocity level as the train passage, and can be determined experimentally or predicted with a numerical model. The force density is affected by the train characteristics as well as the track and soil properties and unevenness, and depends on the position of the source points $\mathbf{X}$ used for the computation of the line source transfer mobility as well as the receiver location $\mathbf{x}_1$.

Alternatively, the force density $\mathrm{L_F}$ can also be computed from the RMS value $\hat{g}_{z\mathrm{RMS}}$ of the dynamic axle load for a single uncoupled axle:

$$\mathrm{L_F} \quad = \quad 10 \log_{10} \left(\frac{n_\mathrm{a}}{L_\mathrm{t}} \hat{g}^2_{z\mathrm{RMS}} \right) \tag{21}$$

where $\hat{g}_{z\mathrm{RMS}}$ is computed from the one-sided PSD $\hat{S}_\mathrm{g}(\omega)$ for each one-third octave band as:

$$\hat{g}_{z\mathrm{RMS}} \quad = \quad \int_{\omega_{\mathrm{l}j}}^{\omega_{\mathrm{u}j}} \hat{S}_\mathrm{g}(\omega) \mathrm{d}\omega \tag{22}$$

The advantage of computing the force density from the axle loads is that the dependence on the position of the source points $\mathbf{X}$ and the receiver location $\mathbf{x}_1$ is removed.

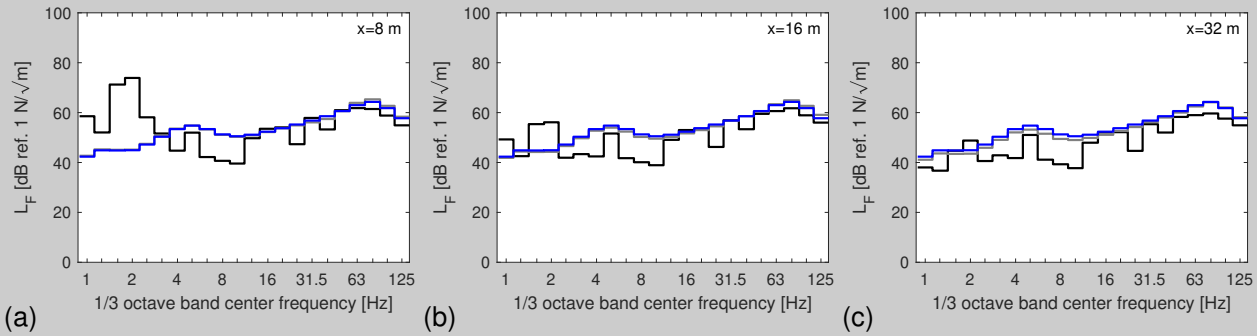

Figure 31: Force density $\mathrm{L_F}$ during the passage of the IC train running at 150 km/h on the ballasted track supported by medium soil. Receivers are located at (a) 8 m, (b) 16 m and (c) 32 m from the track. Results are computed with TRAFFIC based on the dynamic axle loads (blue line), and with the FRA procedure where $\mathrm{L_v}(\mathbf{x}_1)$ is computed for a moving train (black line) and for incoherent axle loads at fixed positions (grey line).

A comparison between both methods to compute the force density is shown in figure 31 for the IC train running at 150 km/h on the ballasted track supported by medium soil. At 8 m from the track, the discrepancy at low frequencies is due to the quasi-static contribution to the vibration velocity level $\mathrm{L_v}(\mathbf{x}_1)$, which is not accounted for in the RMS value of the axle load $\hat{g}_{z\mathrm{RMS}}$ in equation (21). At higher frequencies, the computation of the force density with the FRA procedure (equation (20)) and equation (21) yield similar results. The Doppler effect and the interaction between different axles is, however, not accounted for in equation (21). At 16 m and 32 m, similar observations can be made, but the quasi-static contribution to the vibration velocity level is much lower, which reduces the discrepancy at low frequencies. At high frequencies, the force density computed with the FRA procedure is very similar and is in good agreement with the force density computed from the dynamic axle loads.

In section 3, the vibration velocity level will be computed for dynamic axle loads at fixed positions (neglecting the Doppler effect) and incoherent axles, since these modelling simplifications are made in the prototype vibration prediction tool. In figure 31, the force density is also computed with the FRA procedure accounting for these simplifications. The result is in very good agreement with the force density computed from the dynamic axle loads (equation (21)).

Figure 32 shows the force density computed with TRAFFIC and MOTIV for the IC train running on the ballasted track supported by soft soil. The force density is computed with the FRA procedure (equation (20)). The force density increases with increasing train speed, which is consistent with observations for the dynamic axle loads shown in figure 21. For receivers at 16 m and 32 m from the track, where the quasi-static contribution to the vibration velocity level is limited, the force density is very similar and only differs by a few dB. The discrepancies between TRAFFIC and MOTIV are consistent with earlier observations for the vibration velocity level in figure 28.

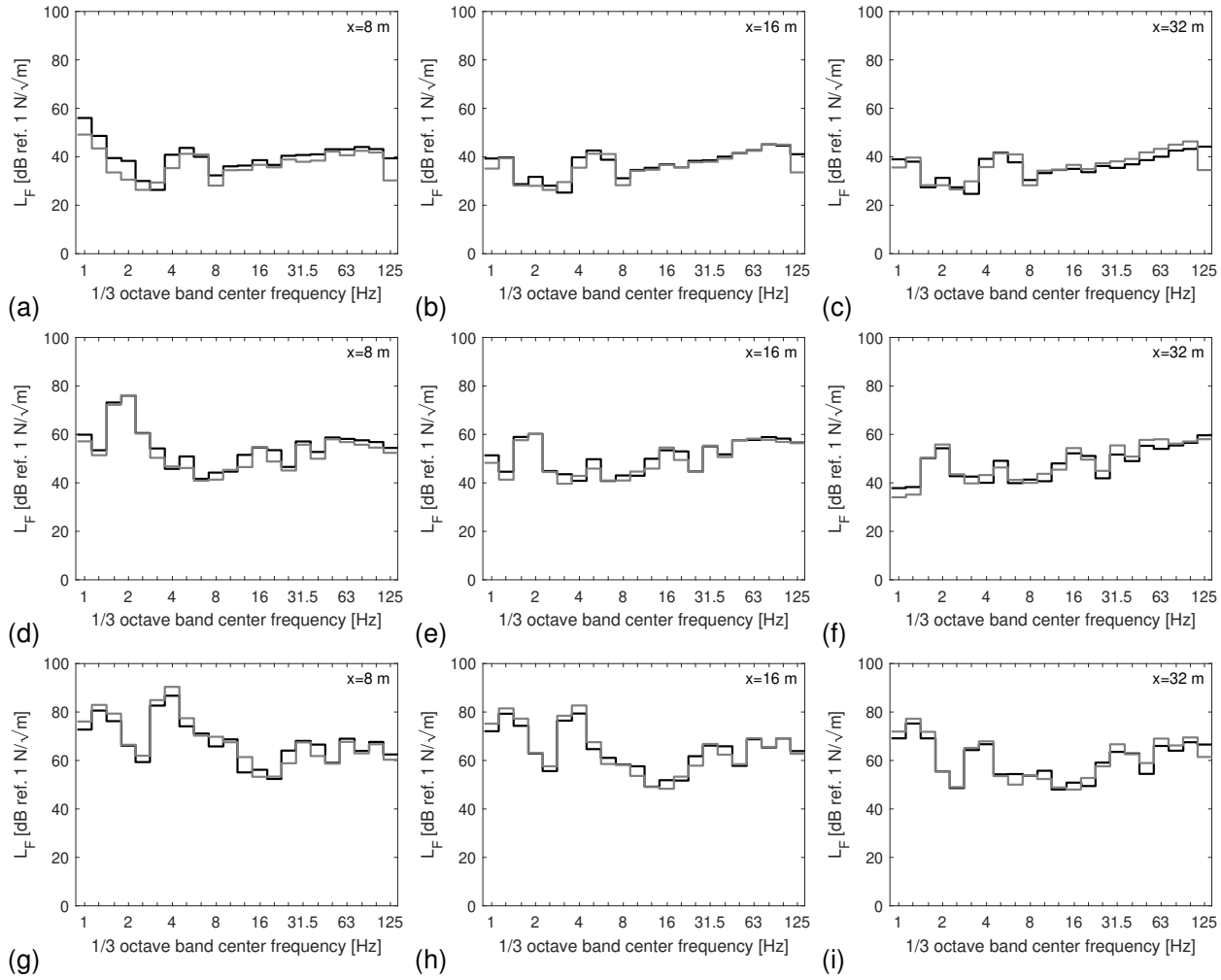

Figure 32: Force density $\mathrm{L_F}(\mathbf{X}, \mathbf{x}_1)$ during the passage of the IC train running at (a-c) 50 km/h, (d-f) 150 km/h and (g-i) 300 km/h on the ballasted track supported by soft soil. Receivers are located at (a,d,g) 8 m, (b,e,h) 16 m and (c,f,i) 32 m from the track. Results are computed with TRAFFIC (black line) and MOTIV (grey line).

Figure 33 shows the force density for the IC train running on the ballasted track supported by medium soil. The trend of the force density is very similar to that for the soft soil (figure 32), characterized by peaks at the axle and vehicle passage frequencies. The peak at the P2 resonance (around 80 Hz) is, however, more pronounced in the force density for the medium soil. The results computed with TRAFFIC and MOTIV are in good overall agreement. The largest discrepancy is found for the force density for a train speed of 50 km/h at 8 m from the track, showing differences up to 10 dB in some frequency bands.

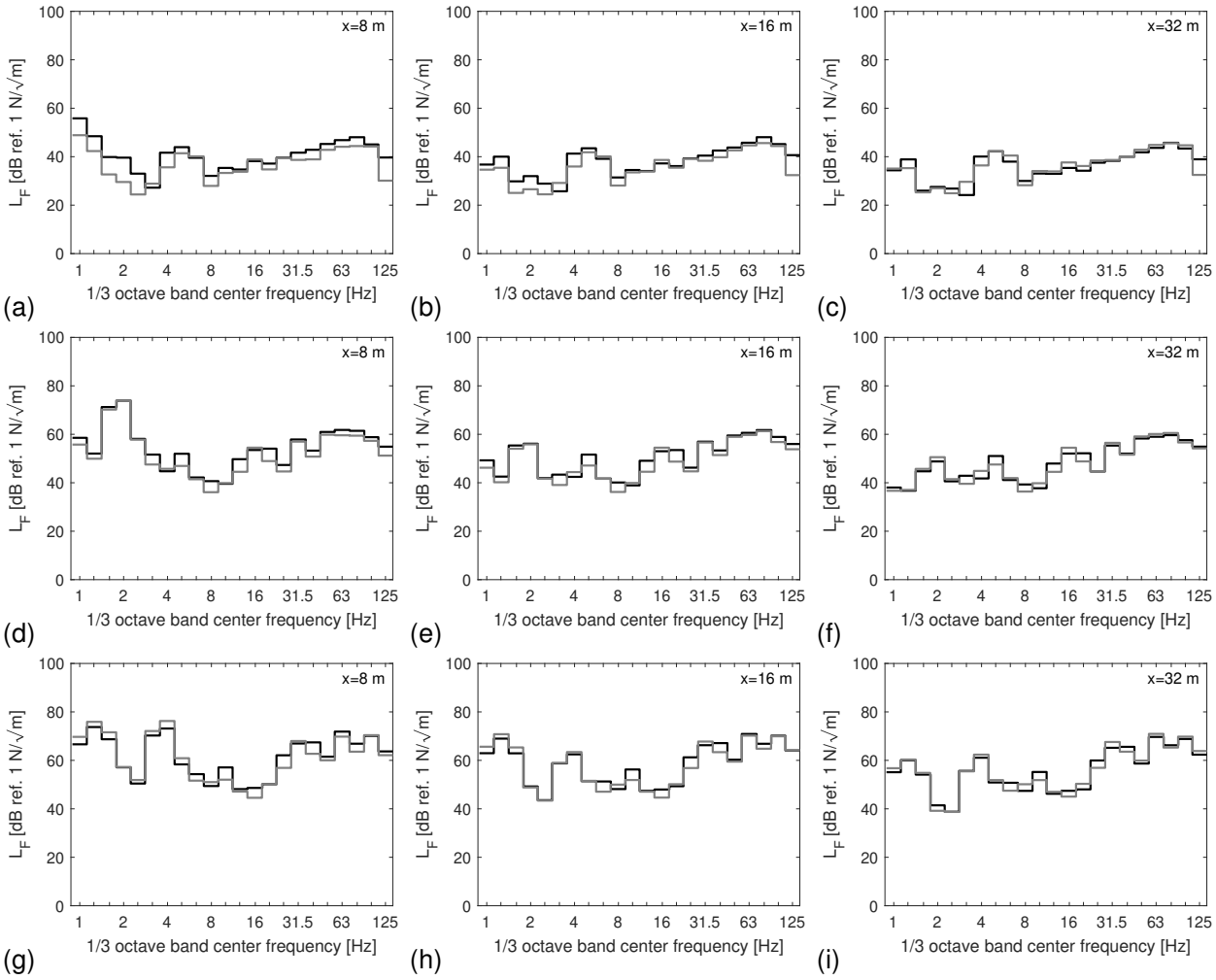

Figure 33: Force density $\mathrm{L_F}(\mathbf{X}, \mathbf{x}_1)$ during the passage of the IC train running at (a-c) 50 km/h, (d-f) 150 km/h and (g-i) 300 km/h on the ballasted track supported by medium soil. Receivers are located at (a,d,g) 8 m, (b,e,h) 16 m and (c,f,i) 32 m from the track. Results are computed with TRAFFIC (black line) and MOTIV (grey line).

For the stiff soil, the force density is shown in figure 34. A clear peak around the P2 resonance is observed. The results obtained with TRAFFIC and MOTIV are in good agreement, especially for train speeds of 150 km/h and 300 km/h where the discrepancy is limited to 5 dB in some frequency bands. For a speed of 50 km/h, the force density at high frequencies predicted with TRAFFIC at 8 m from the track is higher than with MOTIV due to the different kinematic assumptions at the track-soil interface.

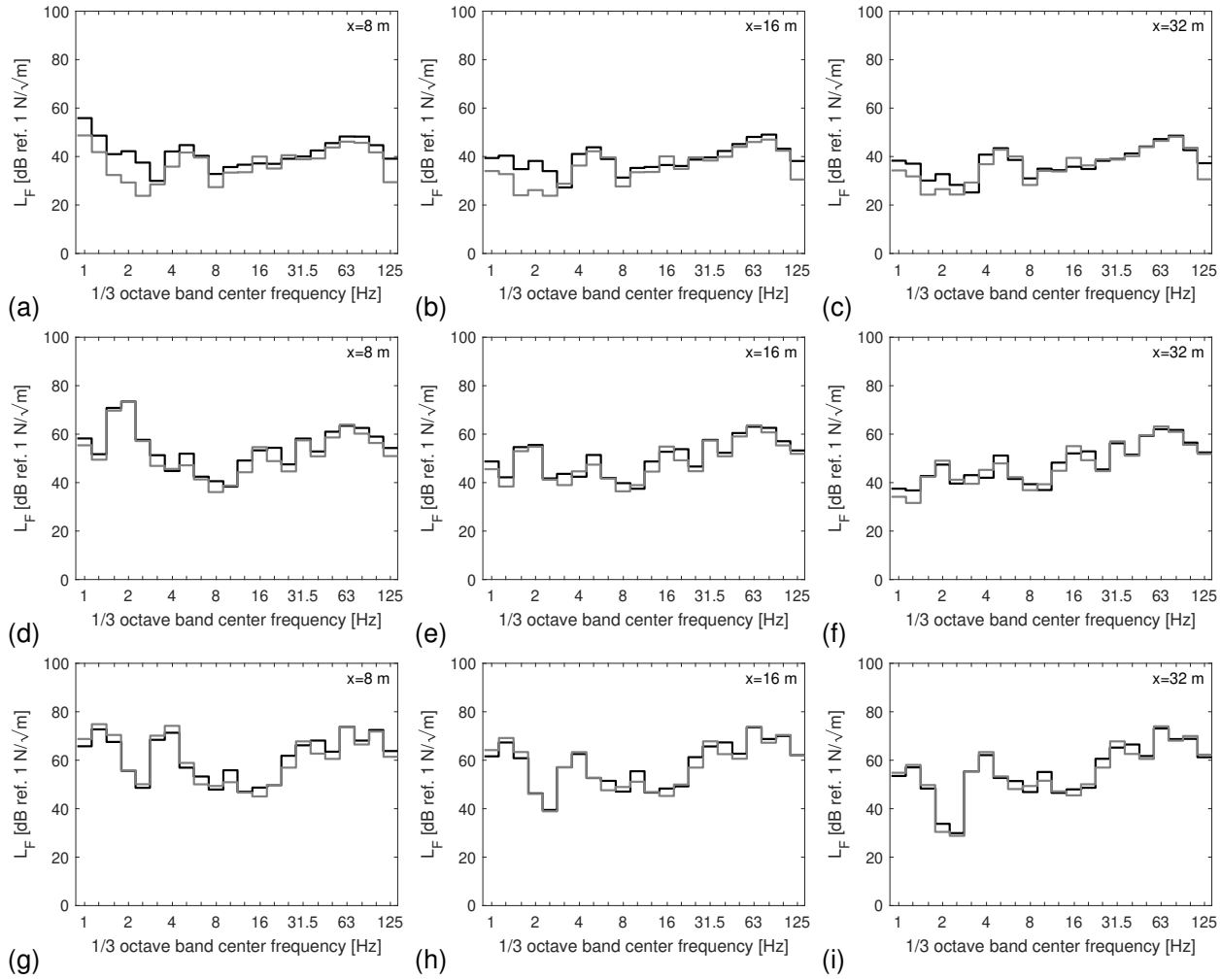

Figure 34: Force density $\mathrm{L_F}(\mathbf{X}, \mathbf{x}_1)$ during the passage of the IC train running at (a-c) 50 km/h, (d-f) 150 km/h and (g-i) 300 km/h on the ballasted track supported by stiff soil. Receivers are located at (a,d,g) 8 m, (b,e,h) 16 m and (c,f,i) 32 m from the track. Results are computed with TRAFFIC (black line) and MOTIV (grey line).

2.8 Comparison for the slab track

In the following, a comprehensive comparison between results obtained with TRAFFIC and MOTIV is presented for the slab track.

2.8.1 Track, vehicle and total compliance

Figure 35 shows the vertical component of the track compliance $\hat{\mathbf{C}}^{\mathrm{t}}(\omega)$ for a load moving at 150 km/h on the slab track supported by soft, medium and stiff soil. At low frequencies, the track compliance decreases with increasing soil stiffness and is lower compared to the ballasted track (figure 9). Above 63 Hz, the track compliance is very close for the three soil types. The results obtained with TRAFFIC and MOTIV are in excellent agreement.

The vehicle compliance $\hat{\mathbf{C}}^{\mathrm{v}}(\omega)$ for the IC train shown in figure 8 is independent from the track type. The discussion of the vehicle compliance is therefore not repeated here.

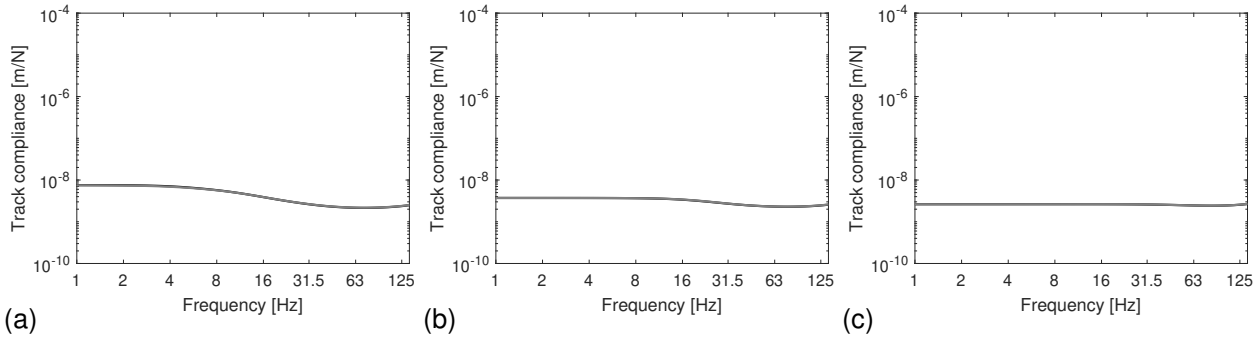

Figure 35: Vertical track compliance $\hat{\mathrm{C}}^{\mathrm{t}}_{11}(\omega)$ for the slab track supported by (a) soft, (b) medium and (c) stiff soil for a load moving at 150 km/h. Results are computed with TRAFFIC (black line) and MOTIV (grey line).

The total compliance $\hat{\mathbf{C}}(\omega)$ is shown in figure 36 for a load moving at 150 km/h. The track and vehicle compliance (computed with the 10-DOF model) are also shown in the figure. The total compliance is

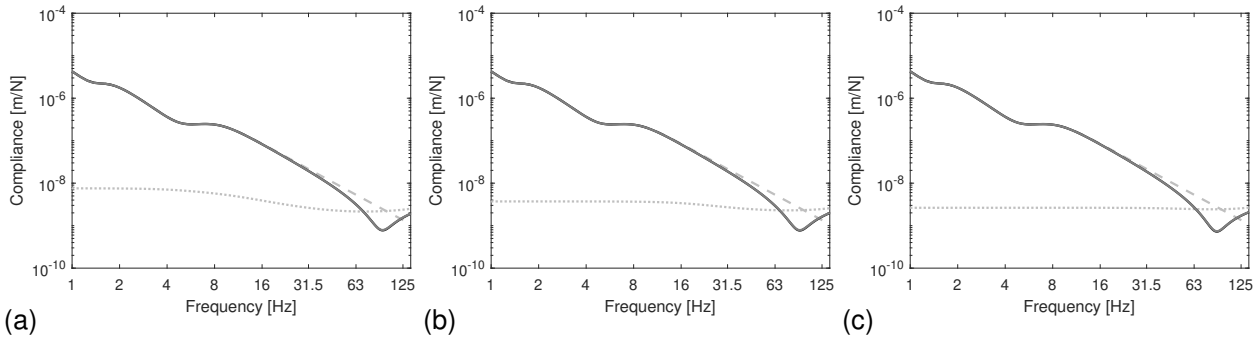

Figure 36: Total compliance $\hat{\mathrm{C}}_{11}(\omega)$ for the slab track supported by (a) soft, (b) medium and (c) stiff soil for a load moving at 150 km/h. Results are computed with TRAFFIC (black line) and MOTIV (grey line). The light grey lines correspond to the track (dotted line) and vehicle (dashed line) compliance.

dominated by the vehicle compliance at low frequencies. The total compliance has its minimum value around 90 Hz, corresponding to a slightly higher P2 resonance frequency than for the ballasted track (80 Hz). The results obtained with TRAFFIC and MOTIV are in excellent agreement.

2.8.2 Track response and transfer functions

The vertical response at the centre of the slab due to a unit axle load distributed equally across both rails at $y = 0$ m is shown in figure 37 for the soft, medium and stiff soil. The results computed with TRAFFIC and MOTIV are in excellent agreement. Below 8 Hz, the slab response is highest for the soft soil.

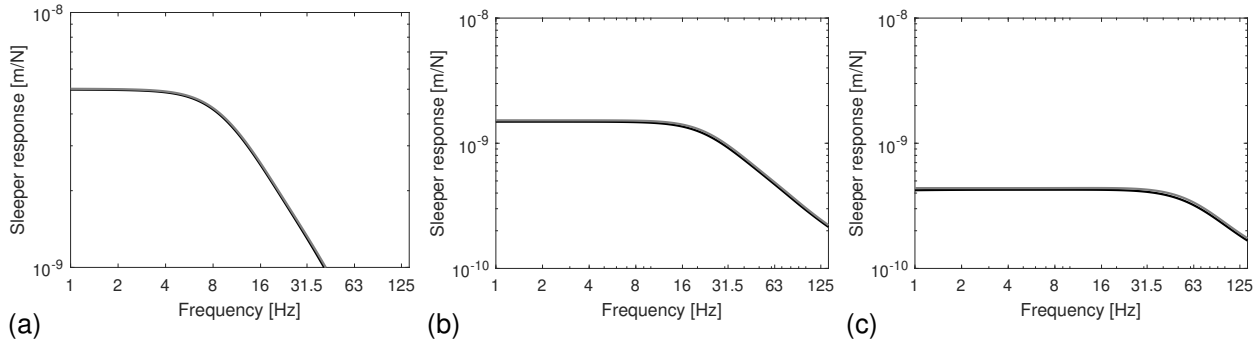

Figure 37: Vertical response at the center of the slab due to a unit axle load for the slab track on (a) soft, (b) medium and (c) stiff soil. Results are computed with TRAFFIC (black line) and MOTIV (grey line).

Next, the vertical track-soil transfer function $\hat{h}_{zz}(\mathbf{x}_1, \omega)$ is discussed. This is the free field displacement along a line perpendicular to the track at $y = 0$ m due to a unit axle load distributed equally to both rails. Figures 38, 39 and 40 show the track-soil transfer functions at 8 m, 16 m and 32 m from the track for the slab track on soft, medium and stiff soil, respectively. The highest free field response is found for the soft soil at low frequencies (38). At high frequencies, the effect of material damping is largest for the soft soil, resulting in the lowest track-soil transfer function. The results computed with TRAFFIC and MOTIV are in very good agreement in the entire frequency range, which was not the case for the ballasted track. This is due to the fact that the slab-soil interface is assumed to be rigid in the track cross-section in both TRAFFIC and MOTIV.

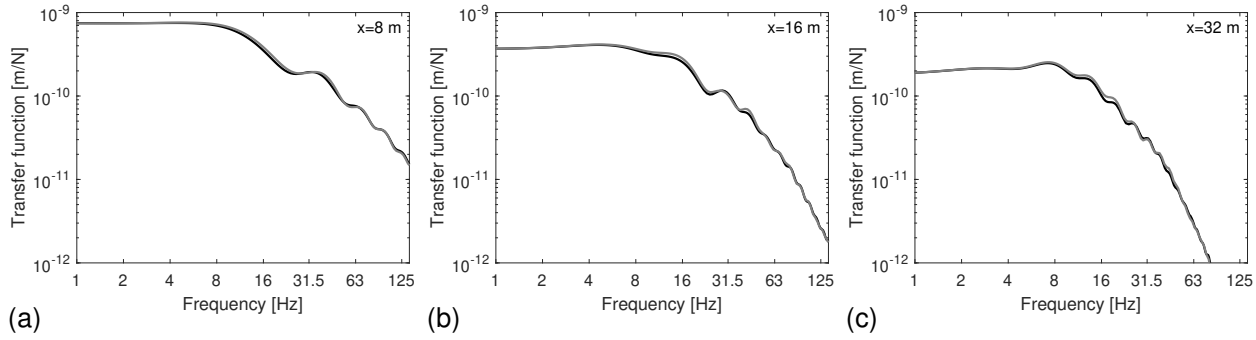

Figure 38: Track-soil transfer function at $y = 0$ m for the slab track on soft soil at (a) 8 m, (b) 16 m and (c) 32 m from the track. Results are computed with TRAFFIC (black line) and MOTIV (grey line).

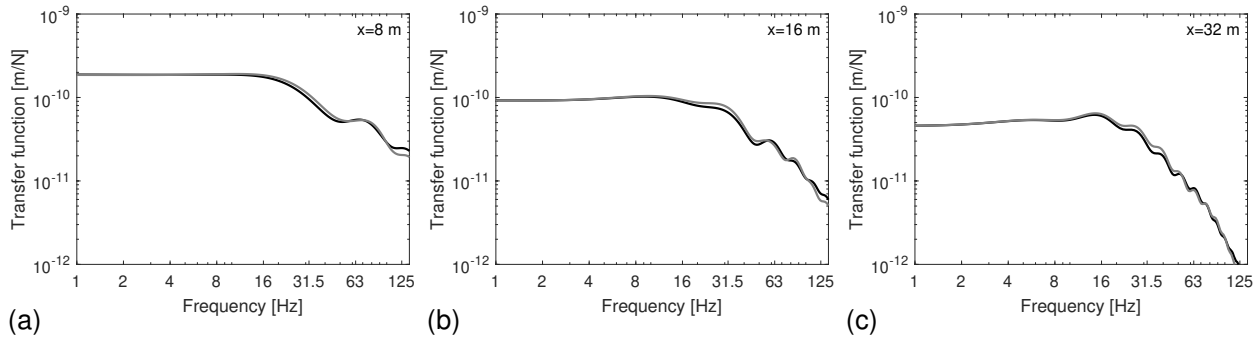

Figure 39: Track-soil transfer function at $y = 0$ m for the slab track on medium soil at (a) 8 m, (b) 16 m and (c) 32 m from the track. Results are computed with TRAFFIC (black line) and MOTIV (grey line).

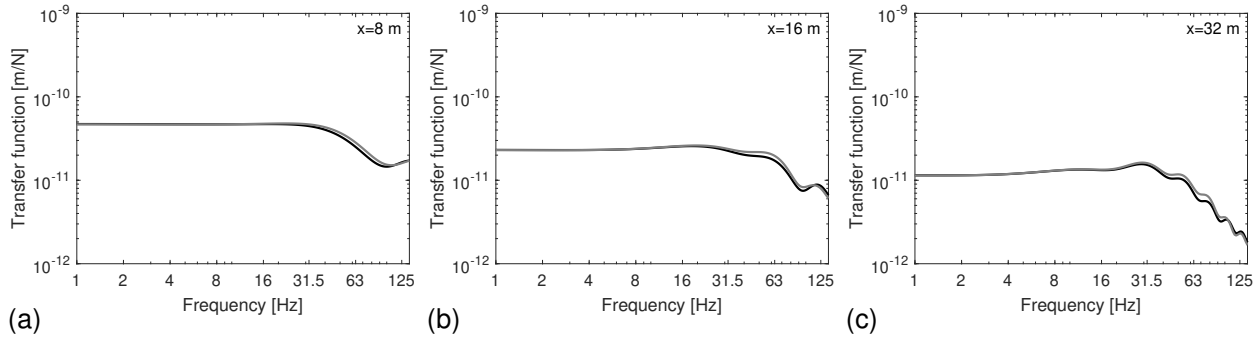

Figure 40: Track-soil transfer function at $y = 0$ m for the slab track on stiff soil at (a) 8 m, (b) 16 m and (c) 32 m from the track. Results are computed with TRAFFIC (black line) and MOTIV (grey line).

2.8.3 Line source transfer mobility

The line source transfer mobility $\mathrm{TM_L}(\mathbf{X}, \mathbf{x}_1)$ is computed for 21 source points located at the rail heads (0.5 N on each rail) with equidistant spacing $h' = 10$ m (see equation (11)). Figures 41, 42 and 43 show the line source transfer mobility at 8 m, 16 m and 32 m from the track supported by soft, medium and stiff soil, respectively. The maximum value is reached around 10 Hz for the soft soil, 30 Hz for the medium soil and between 50 Hz and 63 Hz for the stiff soil. Above these frequencies, the line source transfer mobility rapidly decreases, particularly for receivers far from the track.

The discrepancy between results predicted with TRAFFIC and MOTIV is limited to 1 dB, which is much lower than for the ballasted track (differences up to 5 dB). This is explained by the fact that the slab is assumed to be rigid in the cross-section by both models.

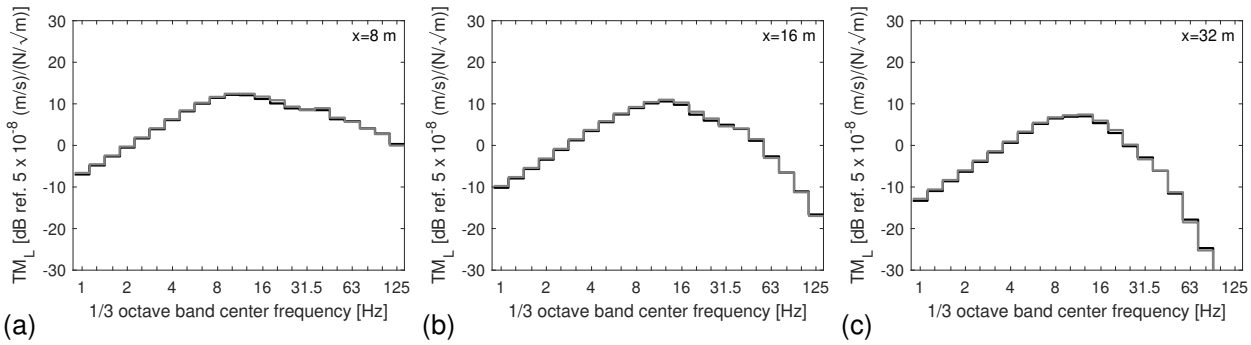

Figure 41: Line source transfer mobility $\mathrm{TM_L}(\mathbf{X}, \mathbf{x}_1)$ of the slab track supported by soft soil for receivers at (a) 8 m, (b) 16 m and (c) 32 m from the track. Results are computed with TRAFFIC (black line) and MOTIV (grey line).

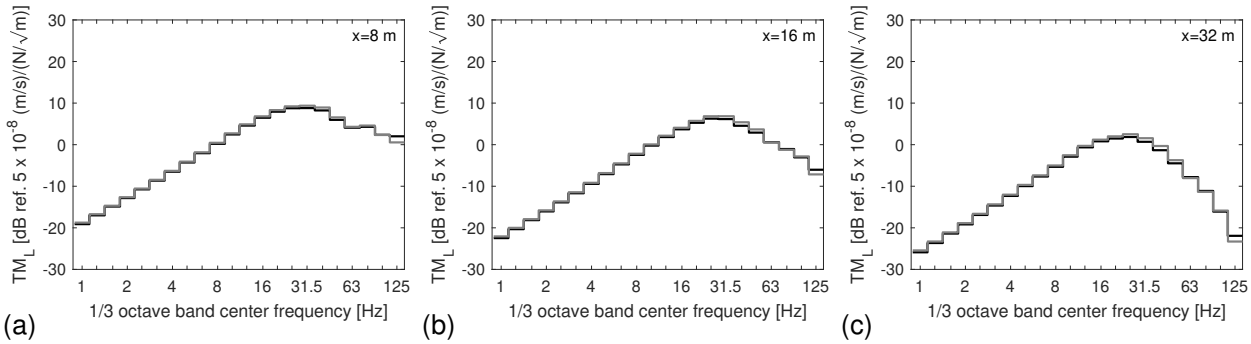

Figure 42: Line source transfer mobility $\mathrm{TM_L}(\mathbf{X}, \mathbf{x}_1)$ of the slab track supported by medium soil for receivers at (a) 8 m, (b) 16 m and (c) 32 m from the track. Results are computed with TRAFFIC (black line) and MOTIV (grey line).

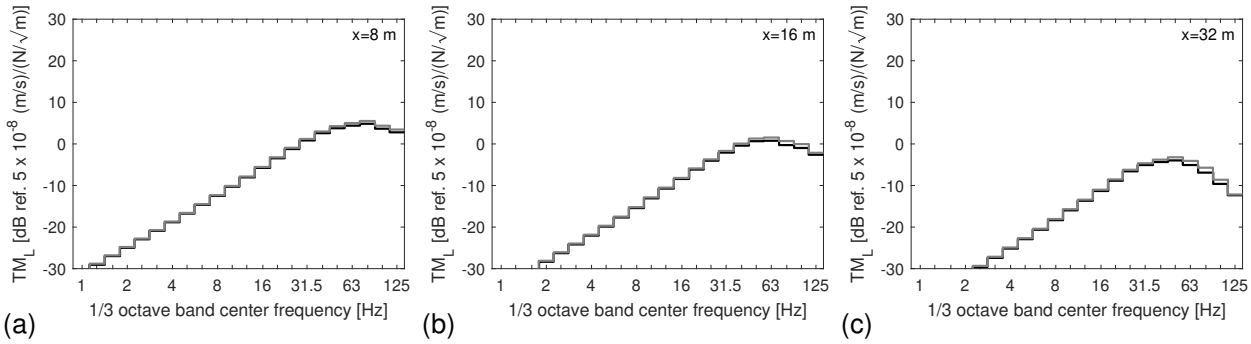

Figure 43: Line source transfer mobility $\mathrm{TM_L}(\mathbf{X}, \mathbf{x}_1)$ of the slab track supported by stiff soil for receivers at (a) 8 m, (b) 16 m and (c) 32 m from the track. Results are computed with TRAFFIC (black line) and MOTIV (grey line).

2.8.4 Dynamic axle loads

First, the dynamic axle loads are computed using equation (7), considering unit track unevenness by setting the term $\frac{1}{v}\tilde{u}_{\mathrm{r}z}(-\frac{\omega}{v})$ in equation (4) equal to unity. The vehicle compliance is computed with the 10-DOF model, and the track compliance is evaluated in the moving frame of reference.

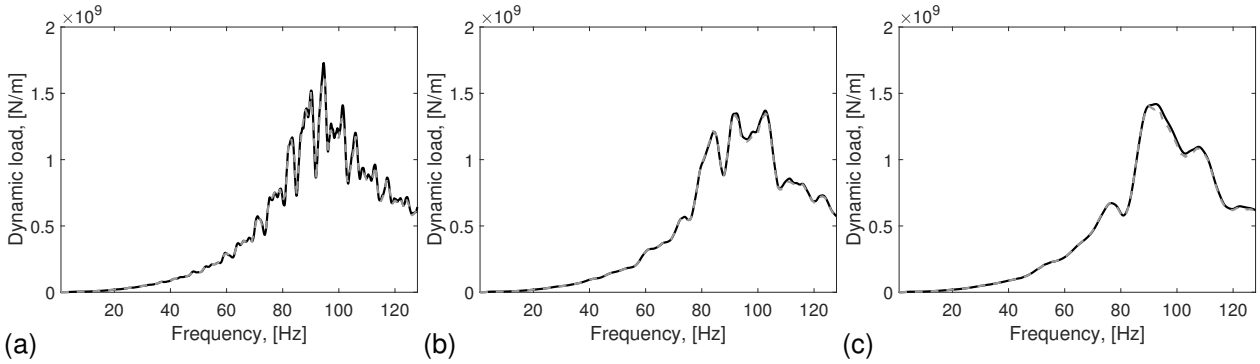

Figure 44: First dynamic axle load of the IC train running at (a) 50 km/h, (b) 150 km/h and (c) 300 km/h on the slab track supported by soft soil. Results are computed with TRAFFIC (black line) and MOTIV (grey dashed line) for unit track unevenness.

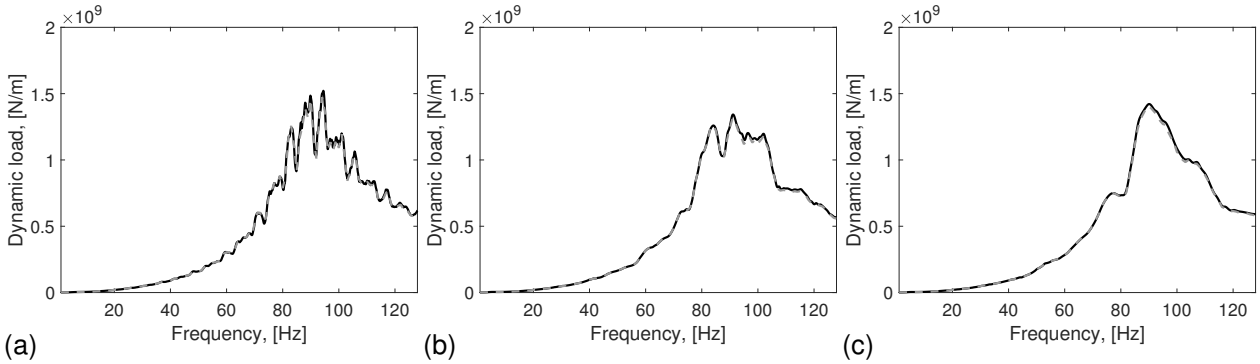

Figure 45: First dynamic axle load of the IC train running at (a) 50 km/h, (b) 150 km/h and (c) 300 km/h on the slab track supported by medium soil. Results are computed with TRAFFIC (black line) and MOTIV (grey dashed line) for unit track unevenness.

Figure 44 shows the first dynamic axle load of the IC train running at 50 km/h, 150 km/h and 300 km/h on the slab track supported by soft soil. A peak due to the P2 resonance of the unsprung axle mass on the track stiffness around 90 Hz is clearly observed for each train speed. Furthermore, smaller peaks are observed related to the axle and vehicle passages (table 6). Compared to the ballasted track (figure 18), the dynamic axle load above 60 Hz is significantly higher for the slab track. The axle loads computed with TRAFFIC and MOTIV are in excellent agreement in the entire frequency range.

Figure 45 shows that the maximum amplitude of the first axle load for the track on medium soil is slightly lower than for the soft soil, particularly for a train speed of 50 km/h, but the trend is very similar. For the stiff soil, figure 49 shows that the first axle load reaches its maximum value around the P2 resonance and is similar to the axle loads for the soft and medium soil. Overall, the influence of the soil stiffness on the dynamic axle loads is limited.

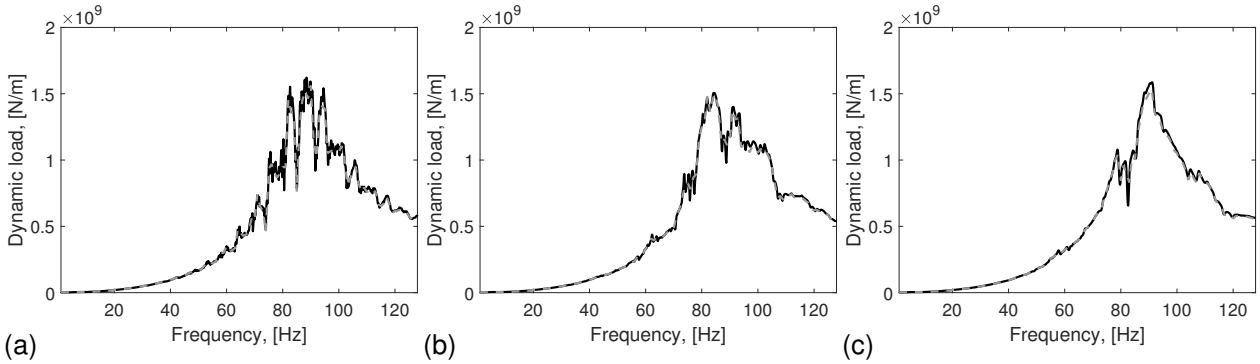

Figure 46: First dynamic axle load of the IC train running at (a) 50 km/h, (b) 150 km/h and (c) 300 km/h on the slab track supported by stiff soil. Results are computed with TRAFFIC (black line) and MOTIV (grey dashed line) for unit track unevenness.

Next, the dynamic axle loads for unit unevenness are multiplied by the actual track unevenness $\frac{1}{v}\tilde{u}_{\mathrm{rz}}(-\frac{\omega}{v})$ corresponding to FRA class 6. Figure 47 shows the first dynamic axle load of the IC train running on the slab track supported by soft soil. The maximum amplitude of the axle load increases from around 1000 N for a train speed of 50 km/h to above 10000 N for a train speed of 300 km/h. Similar observations can be made for the medium (figure 48) and stiff (figure 49) soil. The dynamic axle loads computed with TRAFFIC and MOTIV are generally in very good agreement.

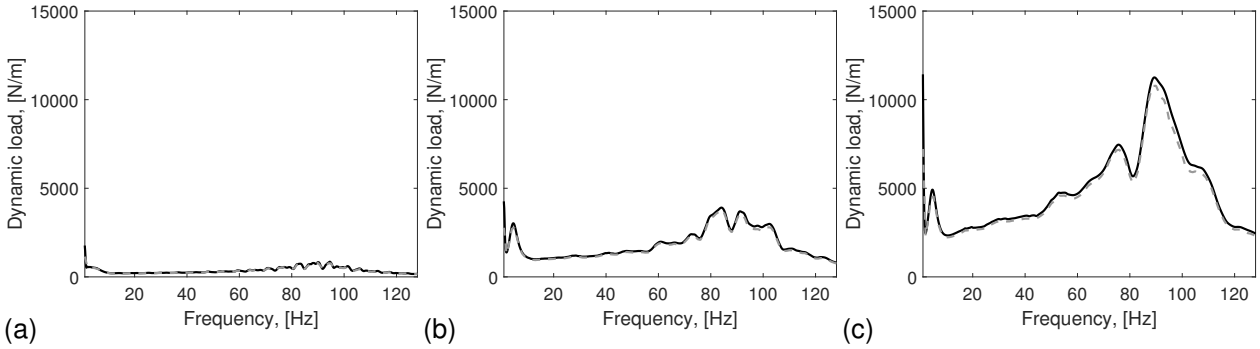

Figure 47: First dynamic axle load of the IC train running at (a) 50 km/h, (b) 150 km/h and (c) 300 km/h on the slab track supported by soft soil. Results are computed with TRAFFIC (black line) and MOTIV (grey dashed line) with track unevenness according to FRA class 6.

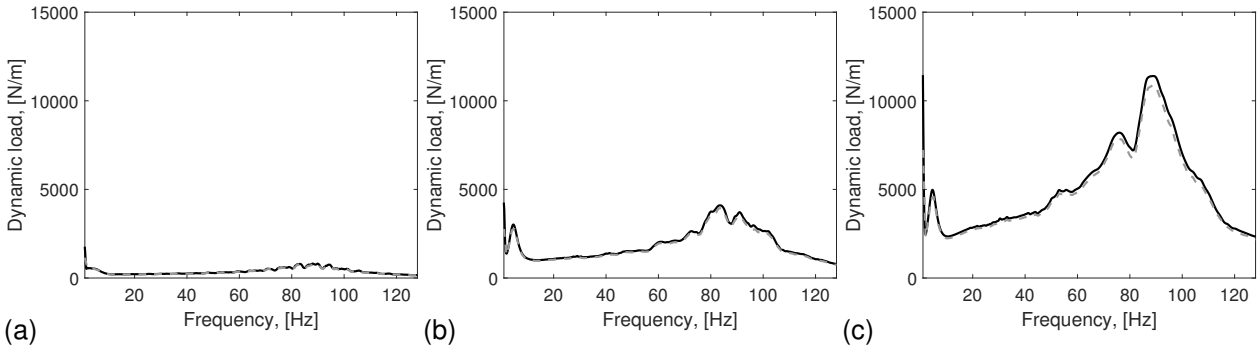

Figure 48: First dynamic axle load of the IC train running at (a) 50 km/h, (b) 150 km/h and (c) 300 km/h on the slab track supported by medium soil. Results are computed with TRAFFIC (black line) and MOTIV (grey dashed line) with track unevenness according to FRA class 6.

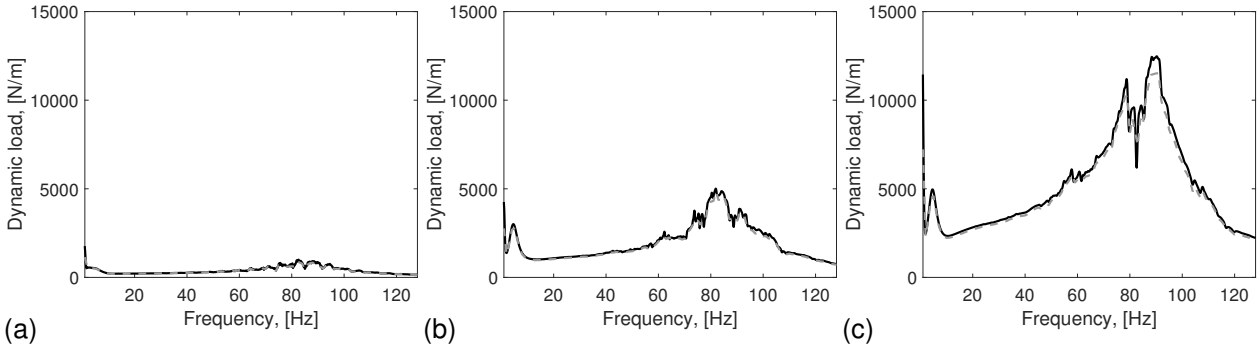

Figure 49: First dynamic axle load of the IC train running at (a) 50 km/h, (b) 150 km/h and (c) 300 km/h on the slab track supported by stiff soil. Results are computed with TRAFFIC (black line) and MOTIV (grey dashed line) with track unevenness according to FRA class 6.

2.8.5 Vibration velocity level

The vibration velocity level $\mathrm{L_v}(\mathbf{x}_1)$ during the passage of the IC train on the slab track supported by soft soil is shown in figure 50. A peak is observed around the axle passage frequency f_a, which is equal to 5.6 Hz, 16.7 Hz and 33.3 Hz for train speeds of 50 km/h, 150 km/h and 300 km/h, respectively (table 6). At lower frequencies, peaks are observed around the vehicle passage frequency f_v. For a train speed of 50 km/h, the vehicle passage frequency is below 1 Hz, and the peak is therefore not clearly visible. For train speeds of 150 km/h and 300 km/h, the vehicle passage frequency equals 1.8 Hz and 3.6 Hz, respectively. The discrepancy between results obtained with TRAFFIC and MOTIV is limited to 5 dB in most frequency bands. The largest discrepancy is observed at frequencies below 30 Hz. At high frequencies, the results are generally in good agreement.

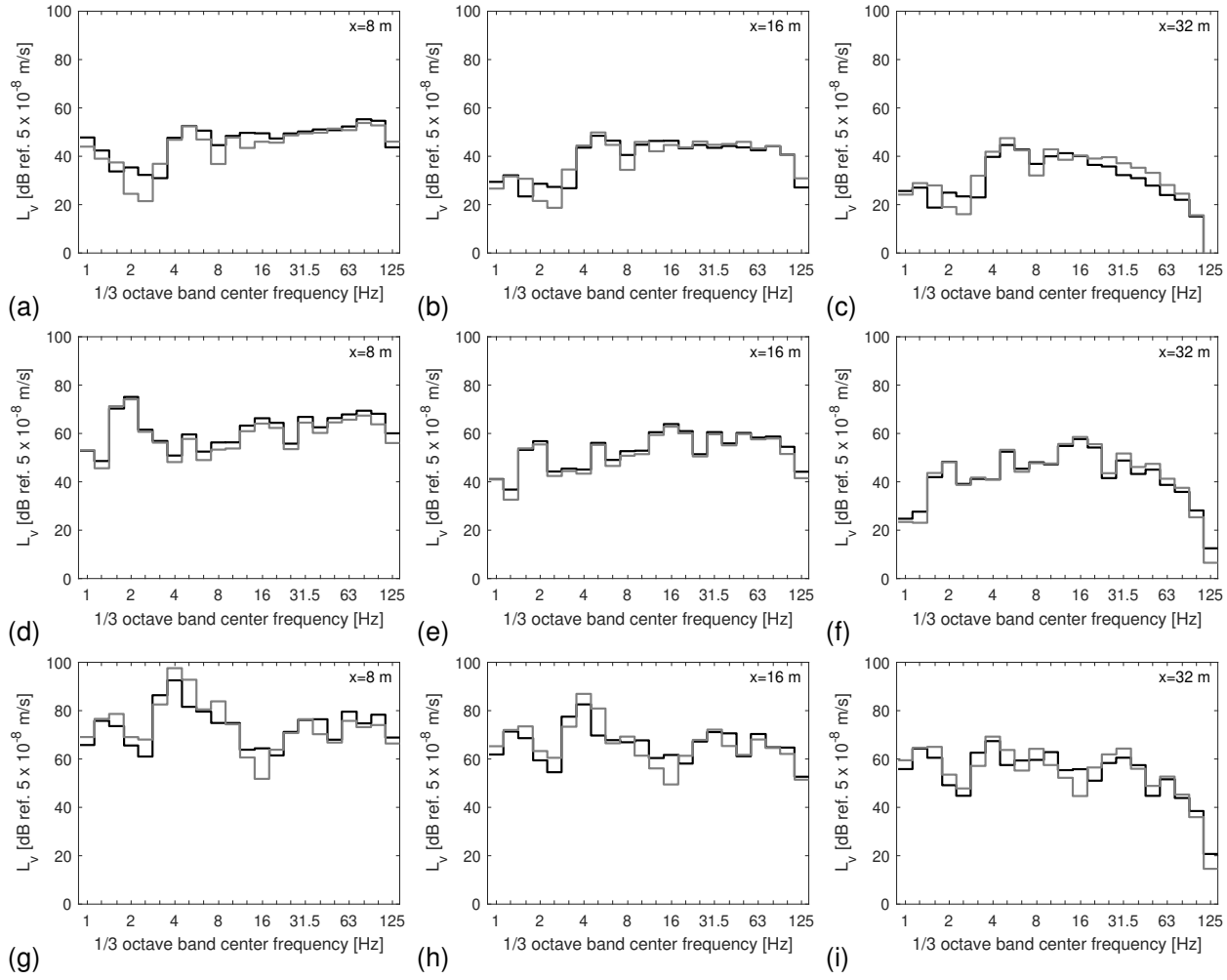

Figure 50: Vibration velocity level $\mathrm{L_v}(\mathbf{x}_1)$ during the passage of the IC train running at (a-c) 50 km/h, (d-f) 150 km/h and (g-i) 300 km/h on the slab track supported by soft soil. Receivers are located at (a,d,g) 8 m, (b,e,h) 16 m and (c,f,i) 32 m from the track. Results are computed with TRAFFIC (black line) and MOTIV (grey line).

Figure 51 shows the vibration velocity level for the slab track on medium soil. Besides peaks due to the axle and vehicle passages, an additional peak is observed around the P2 resonance frequency where the vibration velocity level reaches its maximum value. The largest discrepancy between TRAFFIC and MOTIV is observed below 30 Hz, where differences up to 15 dB are observed in some frequency bands. At high frequencies, the vibration velocity level predicted with the two models is in very good agreement (differences up to 3 dB).

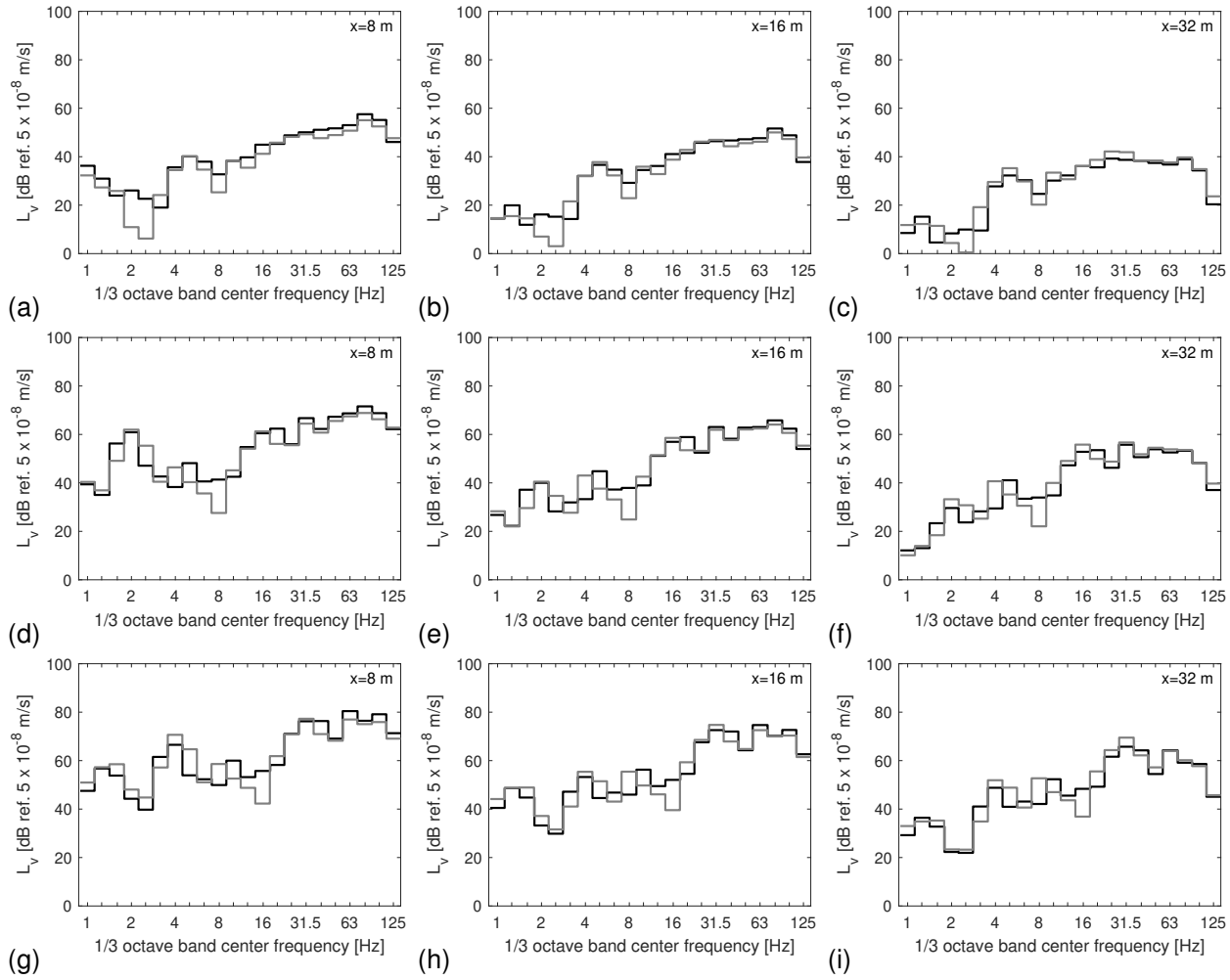

Figure 51: Vibration velocity level $\mathrm{L_v}(\mathbf{x}_1)$ during the passage of the IC train running at (a-c) 50 km/h, (d-f) 150 km/h and (g-i) 300 km/h on the slab track supported by medium soil. Receivers are located at (a,d,g) 8 m, (b,e,h) 16 m and (c,f,i) 32 m from the track. Results are computed with TRAFFIC (black line) and MOTIV (grey line).

In figure 52, the vibration velocity level is shown for the slab track on stiff soil. The P2 resonance around 90 Hz dominates the response. Again, the discrepancy below 30 Hz is significant in some frequency bands, while at high frequencies, the results are in very good agreement.

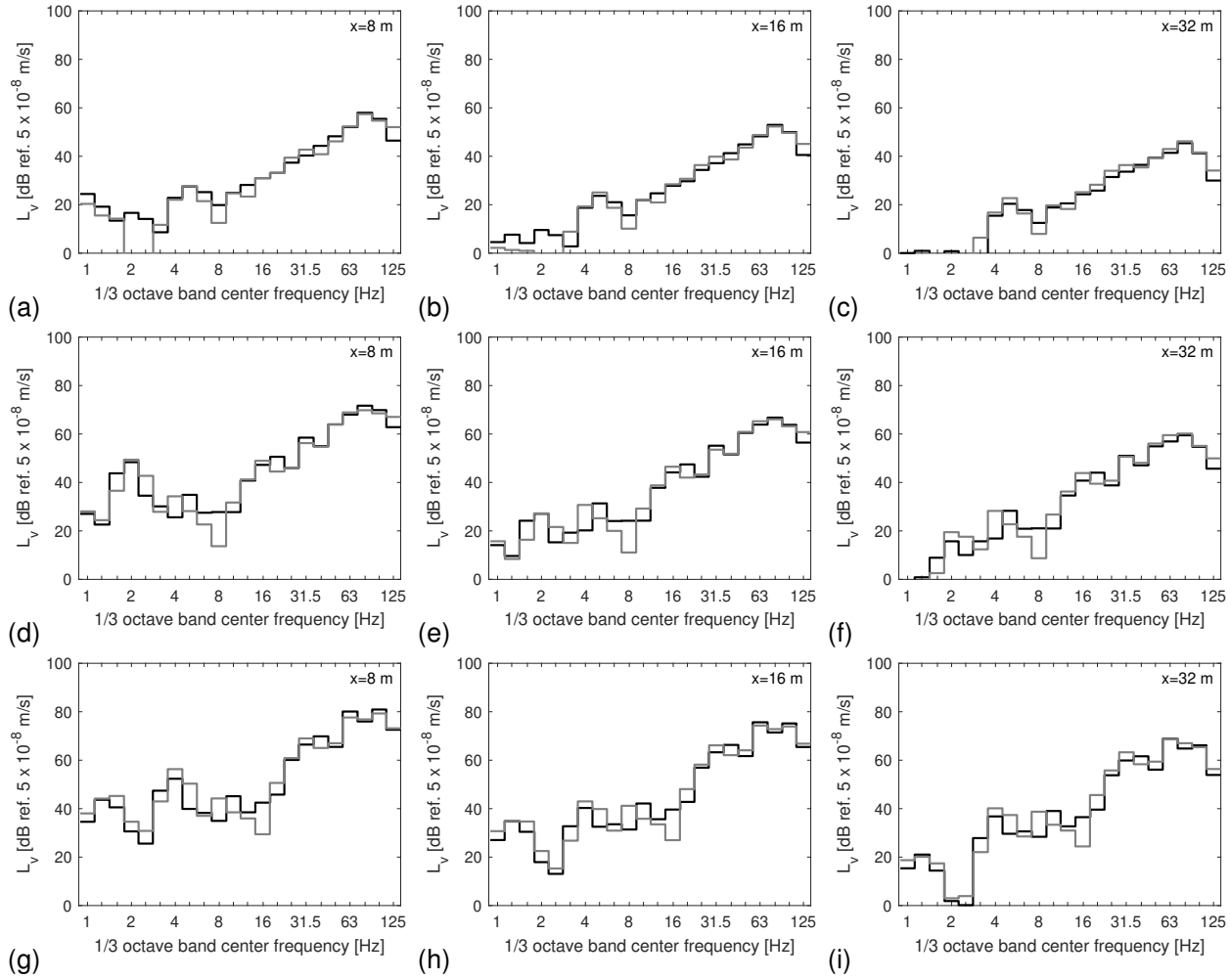

Figure 52: Vibration velocity level $\mathrm{L_v}(\mathbf{x}_1)$ during the passage of the IC train running at (a-c) 50 km/h, (d-f) 150 km/h and (g-i) 300 km/h on the slab track supported by stiff soil. Receivers are located at (a,d,g) 8 m, (b,e,h) 16 m and (c,f,i) 32 m from the track. Results are computed with TRAFFIC (black line) and MOTIV (grey line).

2.8.6 Force density

The force density $\mathrm{L_F}(\mathbf{X}, \mathbf{x}_1)$ is computed using the FRA procedure given in equation (20). Figure 53 shows the force density computed for the slab track on soft soil. The force density is characterized by peaks at the axle and vehicle passage frequencies, as well as a peak around the P2 resonance. The force density increases with increasing train speed, since the dynamic axle loads are higher. At 8 m from the track, the influence of the quasi-static axle loads is observed at low frequencies, resulting in a high force density. At 16 m and 32 m, the quasi-static axle loads do not contribute significantly to the free field response, and the force density is very similar at both distances. The discrepancies between TRAFFIC and MOTIV are mainly due to differences in the vibration velocity level, and are largest in frequency bands below 30 Hz.

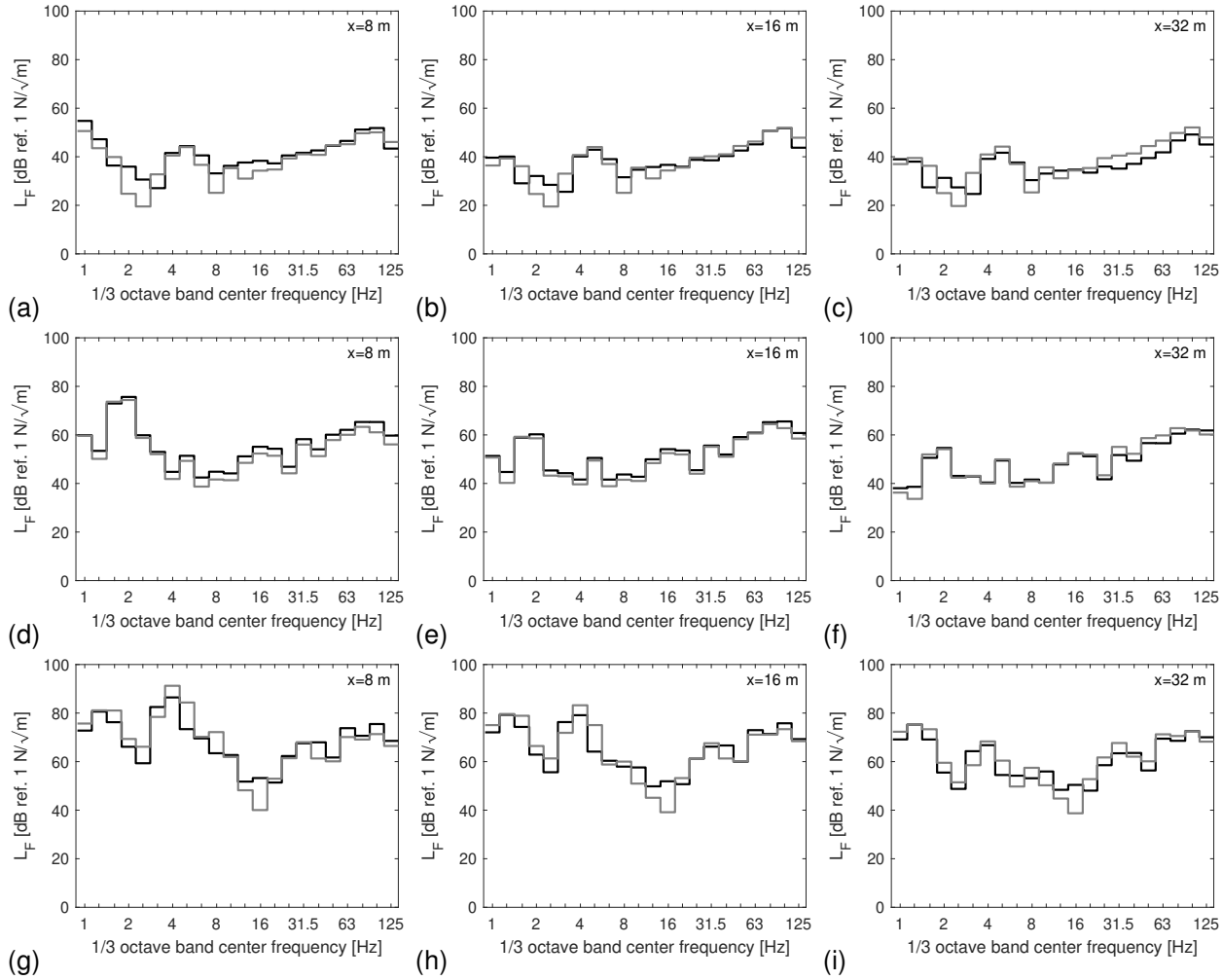

Figure 53: Force density $\mathrm{L_F}(\mathbf{X}, \mathbf{x}_1)$ during the passage of the IC train running at (a-c) 50 km/h, (d-f) 150 km/h and (g-i) 300 km/h on the slab track supported by soft soil. Receivers are located at (a,d,g) 8 m, (b,e,h) 16 m and (c,f,i) 32 m from the track. Results are computed with TRAFFIC (black line) and MOTIV (grey line).

For the track on medium soil, figure 54 shows that the force density is maximum around the P2 resonance, except at 8 m from the track where the quasi-static axle loads result in a high force density at low frequencies. At 16 m and 32 m, the force density is very similar. The results obtained with TRAFFIC and MOTIV are in good agreement at high frequencies, while discrepancies up to 15 dB are observed in some frequency bands below 30 Hz.

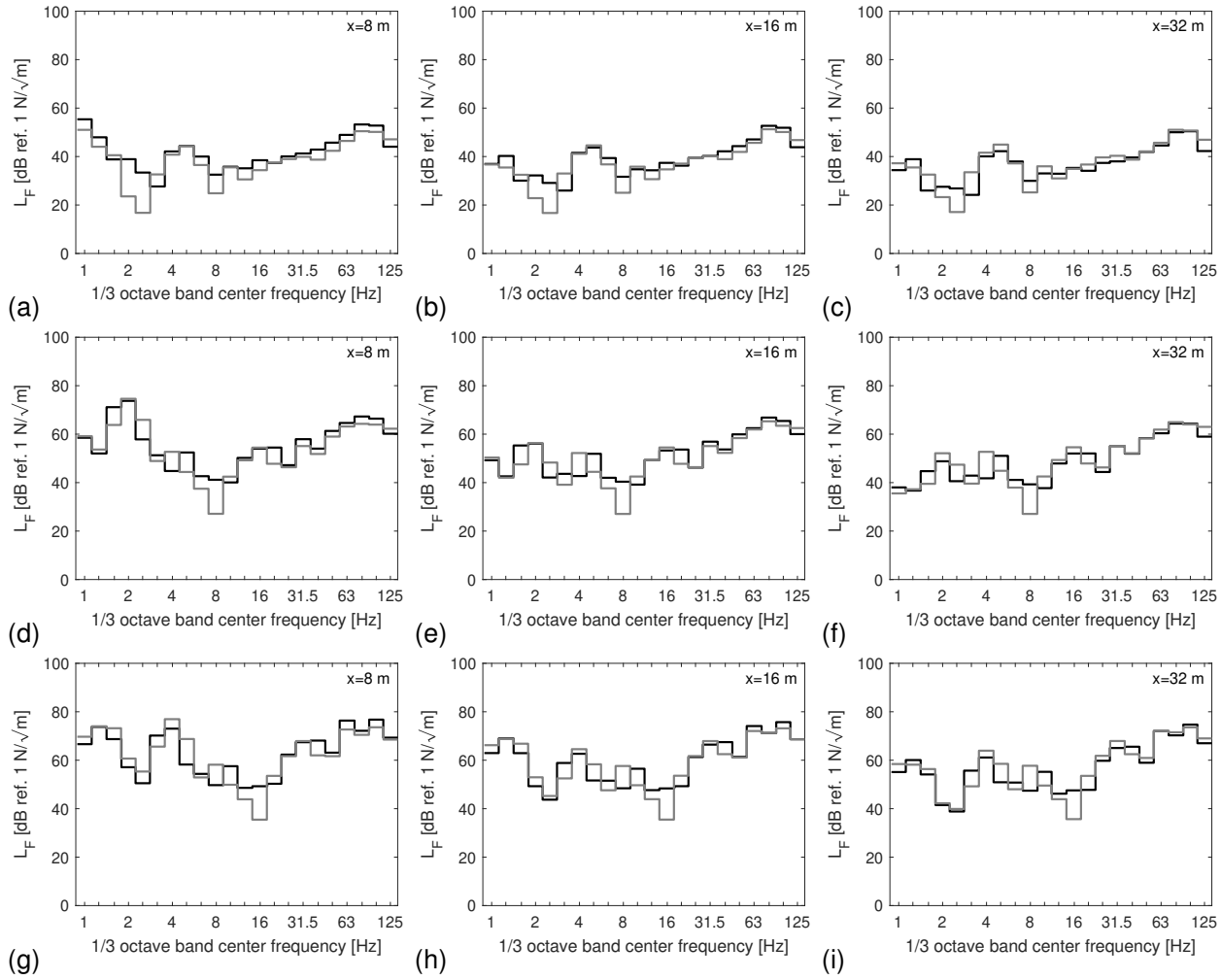

Figure 54: Force density $\mathrm{L_F}(\mathbf{X}, \mathbf{x}_1)$ during the passage of the IC train running at (a-c) 50 km/h, (d-f) 150 km/h and (g-i) 300 km/h on the slab track supported by medium soil. Receivers are located at (a,d,g) 8 m, (b,e,h) 16 m and (c,f,i) 32 m from the track. Results are computed with TRAFFIC (black line) and MOTIV (grey line).

Figure 55 shows the force density for the slab track on stiff soil. The P2 resonance around 90 Hz is clearly observed. The discrepancy between TRAFFIC and MOTIV is limited to a few dB at high frequencies, while considerable differences are observed below 30 Hz.

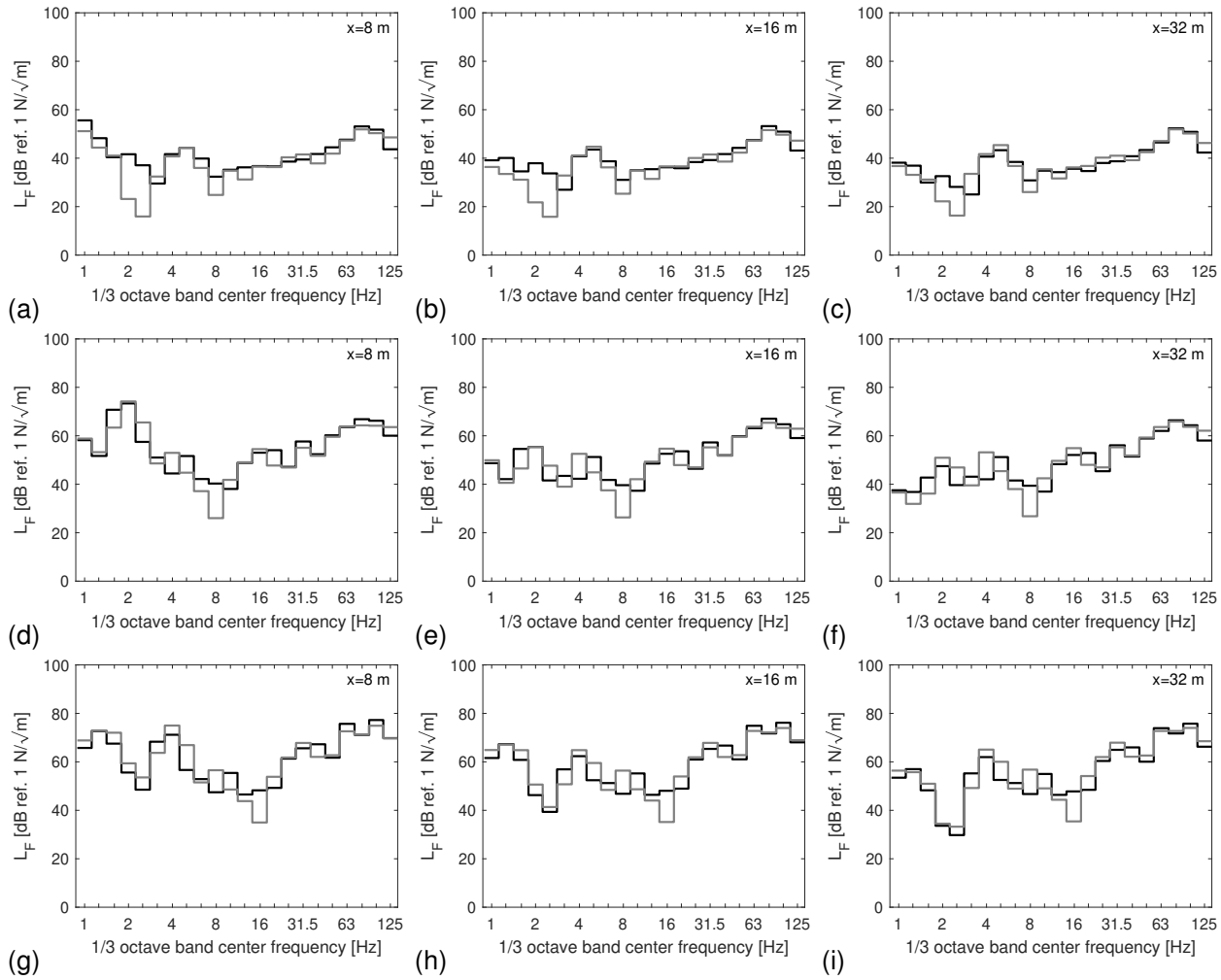

Figure 55: Force density $\mathrm{L_F}(\mathbf{X}, \mathbf{x}_1)$ during the passage of the IC train running at (a-c) 50 km/h, (d-f) 150 km/h and (g-i) 300 km/h on the slab track supported by stiff soil. Receivers are located at (a,d,g) 8 m, (b,e,h) 16 m and (c,f,i) 32 m from the track. Results are computed with TRAFFIC (black line) and MOTIV (grey line).

2.9 Conclusions

This section presents an extensive comparison of state-of-the-art models TRAFFIC and MOTIV for 18 numerical cases: an IC train running at 50 km/h, 150 km/h and 300 km/h on a slab and ballasted track supported by soft, medium and stiff soil. The track and vehicle compliance computed with the two models are in excellent agreement. Hence, the dynamic axle loads, which depend on the track and vehicle compliance as well as the track unevenness (FRA class 6), are also in very good agreement. The track free-field transfer functions differ at high frequencies for the ballasted track due to different kinematic assumptions at the track-soil interface in both models: the transfer functions predicted with TRAFFIC are generally higher than predicted with MOTIV. This also results in higher amplitudes for the line source transfer mobility and the vibration velocity level at high frequencies (differences up to 10 dB). For the slab track, the track free-field transfer functions are in very good agreement in the entire frequency range, which is also reflected in the line source transfer mobility. The vibration velocity level corresponds well at high frequencies (differences up to 5 dB), but larger discrepancies are observed below 30 Hz. For the force density, similar deviations are observed since it is computed from the vibration level and the line source transfer mobility using the FRA procedure.

3. ASSESSMENT OF MODELLING ASSUMPTIONS

3.1 Introduction

The prototype vibration prediction tool uses specific modelling assumptions in order to reduce the computation time. In this section, these assumptions are assessed using TRAFFIC for the ballasted track case described in section 2.2.1. In section 2.7.5, the track compliance was computed in a moving frame of reference, and the vibration velocity level was computed for moving, coherent axle loads. In this section, the following modelling simplifications will be introduced step-by-step:

1. The effect of train speed on the track compliance $\hat{\mathbf{C}}^{\mathrm{t}}(\omega)$ is disregarded and the track compliance $\hat{\mathbf{C}}^{\mathrm{t}}(\omega)$ is computed for a stationary load.
2. The dynamic axle loads are applied at fixed positions instead of moving along the track with the train speed v. This corresponds to a low-speed approximation for which the Doppler effect is neglected.
3. The axle loads are assumed to be incoherent by neglecting the cross-PSD terms $\hat{S}_{gkl}(\omega)$ of the dynamic axle loads.

The influence of these simplifications is assessed in terms of vibration velocity level difference $\Delta \mathrm{L_v}(\mathbf{x}_1)$:

$$\Delta \mathrm{L_v}(\mathbf{x}_1) \quad = \quad \mathrm{L_v^{approx}}(\mathbf{x}_1) - \mathrm{L_v^{ref}}(\mathbf{x}_1) \tag{23}$$

where $\mathrm{L_v^{approx}}(\mathbf{x}_1)$ is the vibration velocity level accounting for the simplification, and $\mathrm{L_v^{ref}}(\mathbf{x}_1)$ is the reference vibration velocity level. Note that, as the simplifications are introduced step-by-step, the reference $\mathrm{L_v^{ref}}(\mathbf{x}_1)$ is taken as the vibration velocity level $\mathrm{L_v^{approx}}(\mathbf{x}_1)$ from the previous step. For the first step, the reference vibration velocity level $\mathrm{L_v^{ref}}(\mathbf{x}_1)$ corresponds to the vibration velocity level (computed with TRAFFIC) presented in section 2. Note that the contribution of the quasi-static axle loads to the vibration velocity level is disregarded in this section.

In the following, the theoretical background for each simplification is discussed first, followed by its effect on the vibration velocity level $\mathrm{L_v}(\mathbf{x}_1)$. Results are shown in terms of $\Delta \mathrm{L_v}(\mathbf{x}_1)$ for the IC train consisting of 4 vehicles (each represented by a 10-DOF vehicle model) running at 50 km/h, 150 km/h and 300 km/h on the ballasted track supported by soft, medium and stiff soil. The section is concluded with a summary comparing the vibration velocity level from section 2.7.5 (moving train, coherent axle loads) to the vibration velocity level accounting for all modelling assumptions. In order to assess and compare the overall vibration velocity level summed over all frequency bands, the global vibration velocity level $\mathrm{L_v^{global}}(\mathbf{x}_1)$ is also presented in subsection 3.5, calculated by summing the contributions in each one-third frequency band j:

$$\mathrm{L_v^{global}}(\mathbf{x}_1) \quad = \quad 10 \log_{10} \left(\sum_j 10^{\frac{\mathrm{L_v^j}(\mathbf{x}_1)}{10}} \right) \tag{24}$$

3.2 Track compliance in a moving versus a stationary frame of reference

The vertical components $\hat{C}^{\mathrm{t}}_{kl}(\omega)$ of the track compliance matrix $\hat{\mathbf{C}}^{\mathrm{t}}(\omega)$ correspond to the vertical displacement at the position of axle l due to a unit vertical load at the position of axle k, and is calculated in a moving frame of reference as:

$$\hat{C}^{\mathrm{t}}_{kl}(\omega) \quad = \quad \frac{1}{2\pi} \int_{-\infty}^{+\infty} \tilde{h}^{\mathrm{t}}_{zz}(k_y, \omega + k_y v) \exp\left[-\mathrm{i} k_y (y_{l0} - y_{k0})\right] \mathrm{d}k_y \tag{25}$$

where $\tilde{h}^{\mathrm{t}}_{zz}(k_y, \omega + k_y v)$ denotes the track-to-track transfer function in the wavenumber-frequency domain in a frame of reference moving with speed v. By setting the train speed equal to zero, the effect of the train speed on the transfer function $\tilde{h}^{\mathrm{t}}_{zz}(k_y, \omega)$, and thus the track compliance, is disregarded. With this simplification, the transfer function $\tilde{h}^{\mathrm{t}}_{zz}(k_y, \omega)$ becomes an even function of the wavenumber k_y and the computational effort to calculate the integrals in equation (25) is reduced.

Figure 56a shows the magnitude of the vertical track compliance function $\hat{C}^{\mathrm{t}}_{11}(\omega)$ computed for a non-moving load and for a load moving at 50 km/h, 150 km/h and 300 km/h on the ballasted track on medium soil. It can be seen that the effect of speed on the track compliance is limited. In addition, figure 56b shows the effect of the speed on the coupling term $\hat{C}^{\mathrm{t}}_{12}(\omega)$ (i.e. the response at the position of the second wheelset due to a load at the first wheelset). A dip is observed around 75 Hz for the non-moving load; the dip shifts to lower frequencies with increasing train speed. However, as the amplitude of the coupling term $\hat{C}^{\mathrm{t}}_{12}(\omega)$ is much lower than $\hat{C}^{\mathrm{t}}_{11}(\omega)$, the overall effect of speed on the track compliance, and hence on the dynamic axle loads and vibration velocity level, is expected to be limited.

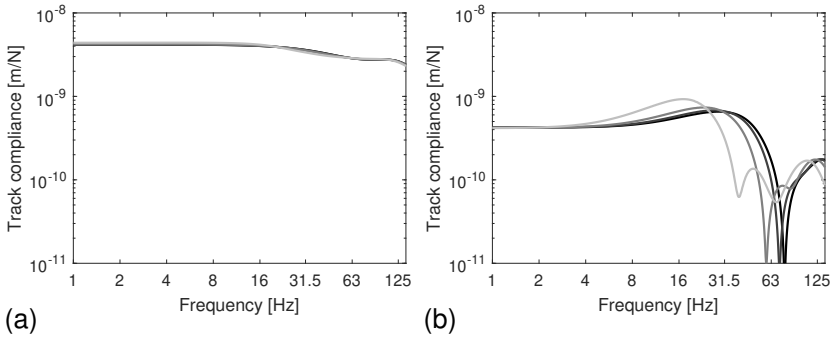

Figure 56: Vertical track compliance (a) $\hat{C}^{\mathrm{t}}_{11}(\omega)$ and (b) $\hat{C}^{\mathrm{t}}_{12}(\omega)$ for the ballasted track on medium soil computed in a stationary frame of reference (black line) and a moving frame of reference for speeds of 50 km/h, 150 km/h and 300 km/h (dark to light grey lines).

Figure 57 shows the vibration velocity level difference $\Delta \mathrm{L_v}(\mathbf{x}_1)$ between the free-field response at distances 8 m, 16 m and 32 m from the track calculated using the track compliance due to the non-moving loads and that for moving loads. Results are shown for train speeds of 50 km/h, 150 km/h and 300 km/h, and for the three soil types.

A very good agreement is shown in figure 57 between results computed with the track compliance in a moving and non-moving frame of reference. Some small differences can be seen for the train speed of 300 km/h in figures 57g to 57i. As these level differences are less than 1 dB, the influence of the moving load on the track compliance does not affect the vibration predictions in the free field. This is also

demonstrated from the global vibration velocity levels reported in tables 7 to 9 of section 3.5, where almost no difference is reported between the global vibration velocity level from the nominal case and the current approximation (defined as approximation A1 in the tables).

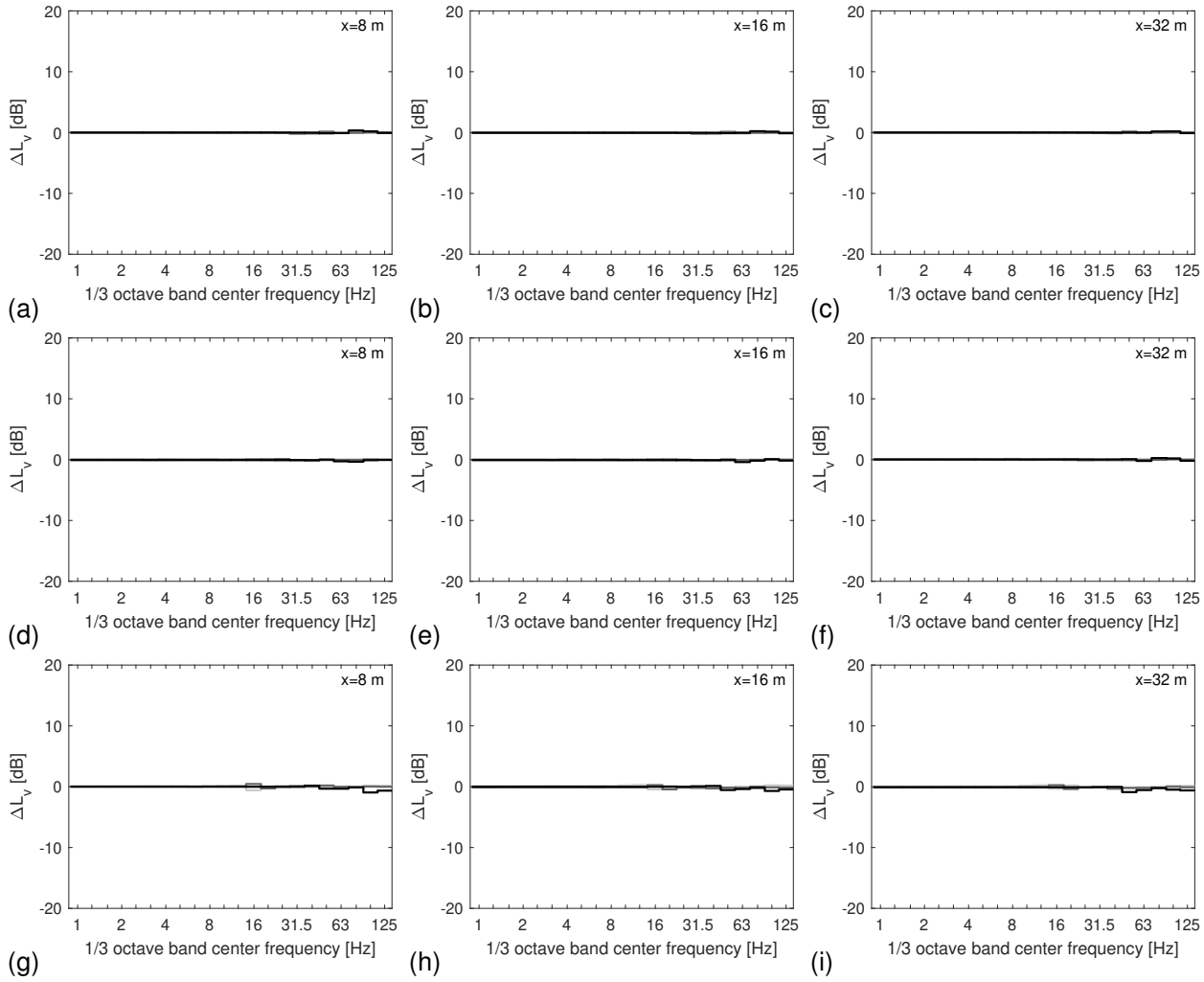

Figure 57: Vibration velocity level difference $\Delta \mathrm{L_v}(\mathbf{x}_1)$ due to the computation of the track compliance in a stationary instead of moving frame of reference. Results are shown for the IC train running at (a-c) 50 km/h, (d-f) 150 km/h and (g-i) 300 km/h on the ballasted track supported by soft (light grey line), medium (dark grey line) and stiff (black line) soil. Receivers are located at (a,d,g) 8 m, (b,e,h) 16 m and (c,f,i) 32 m from the track.

3.3 Low-speed approximation

The free field response increases when the train approaches, is almost stationary during the train passage, and decreases once the train has passed. This is illustrated by the RMS velocity shown in figure 26. The duration of the stationary part depends on the train length and the train speed. It is expected that the low-speed approximation yields accurate results for long trains and low train speeds.

The low-speed approximation aims to predict the vibration velocity level $\mathrm{L_v}(\mathbf{x}_1)$ during the stationary part of the response by assuming fixed axle positions. This is achieved by considering the speed v equal to zero in equation (13), which results in:

$$\begin{aligned}\hat{v}_z(x,y,\omega) &= \sum_{k=1}^{n_\mathrm{a}} \frac{1}{2\pi} \int_{-\infty}^{+\infty} \mathrm{i}\omega \tilde{h}_{\mathrm{zz}}\left(x,k_y,\omega\right) \exp\left[-\mathrm{i}k_y(y-y_{k0})\right] \hat{g}_{\mathrm{d}kz}(\omega)\mathrm{d}k_y \\ &= \sum_{k=1}^{n_\mathrm{a}} \mathrm{i}\omega \hat{h}_{\mathrm{zz}}\left(x,y-y_{k0},\omega\right) \hat{g}_{\mathrm{d}kz}(\omega) \end{aligned} \tag{26}$$

by evaluating the inverse Fourier transform from the wavenumber domain k_y to the coordinate y. As a result, the frequency shift between the receiver and the source due to the Doppler effect is disregarded.

Since the dynamic axle loads $\hat{g}_{\mathrm{d}kz}(\omega)$ are determined by random track unevenness, they represent a random process. The free field response $\hat{v}_z(x,y,\omega)$ due to random axle loads is a random process as well, characterized by the one-sided PSD $\hat{S}_\mathrm{v}(x,y,\omega)$:

$$\hat{S}_\mathrm{v}(x,y,\omega) = \sum_{k=1}^{n_\mathrm{a}} \sum_{l=1}^{n_\mathrm{a}} \omega^2 \hat{h}_{\mathrm{zz}}\left(x,y-y_{k0},\omega\right) \hat{S}_{\mathrm{g}kl}(\omega) \hat{h}^*_{\mathrm{zz}}\left(x,y-y_{l0},\omega\right) \tag{27}$$

The vibration velocity level $\mathrm{L_v}(\mathbf{x}_1)$ is subsequently obtained by integrating the PSD $\hat{S}_\mathrm{v}(x,y,\omega)$ in each one-third octave band.

Figure 58 shows the vibration velocity level difference $\Delta\mathrm{L_v}(\mathbf{x}_1)$ between the response calculated with the low-speed approximation (26) and the moving train response for the three trains speeds 50 km/h, 150 km/h and 300 km/h. Results are shown for receivers at different distances from the track and for the three soil types.

It is observed that the differences increase when the train speed increases with respect to the dominant wave speed in the soil; deviations of more than 10 dB are found in individual frequency bands at the highest speed of 300 km/h. Nevertheless, these differences mainly correspond to a redistribution of energy into different frequency bands due to the Doppler effect, and hence, the overall vibration level summed over all frequency bands is affected much less. This can be seen in the global vibration levels reported in tables 7 to 9 of section 3.5 where the differences between the nominal case of a moving train (case A1) and the current approximation (defined as case A1+A2) show differences of 1 dB to 3 dB.

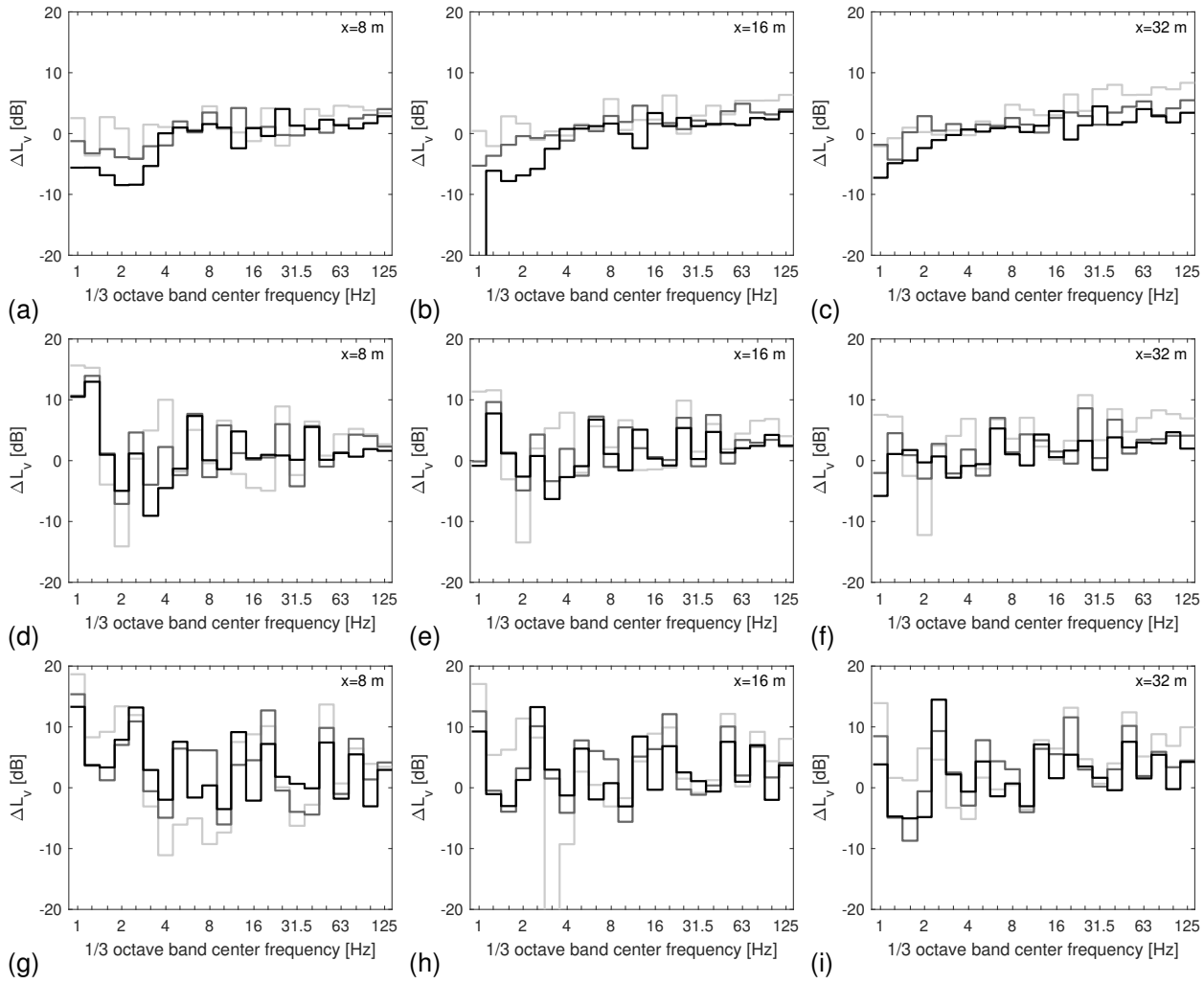

Figure 58: Vibration velocity level difference $\Delta \mathrm{L_v}(\mathbf{x}_1)$ due to the low-speed approximation. Results are shown for the IC train running at (a-c) 50 km/h, (d-f) 150 km/h and (g-i) 300 km/h on the ballasted track supported by soft (light grey line), medium (dark grey line) and stiff (black line) soil. Receivers are located at (a,d,g) 8 m, (b,e,h) 16 m and (c,f,i) 32 m from the track.

3.4 Coherent versus incoherent axle loads

The final simplification is the assumption of incoherent axle loads. This means that the coherence between two axles k and l, included through the cross-PSD $\hat{S}_{gkl}(\omega)$, is not taken into account. As the cross-PSD terms $\hat{S}_{gkl}(\omega)$ are oscillating functions with a period determined by the time lag $(y_{k0} - y_{l0})/v$, they give rise to an oscillating PSD $\hat{S}_{\mathrm{v}}(\omega)$ as well. It is expected that these oscillations cancel out when integrating in sufficiently wide frequency bands to obtain the vibration velocity level $\mathrm{L}_{\mathrm{v}}(\mathbf{x}_1)$. Hence, it is expected that the assumption of incoherent axle loads will mostly affect the vibration velocity level at low frequencies where the one-third octave bands are narrower. Assuming incoherent axle loads, equation (27) becomes:

$$\hat{S}_{\mathrm{v}}(x, y, \omega) \quad = \quad \sum_{k=1}^{n_{\mathrm{a}}} \omega^2 |\hat{h}_{\mathrm{zz}}\left(x, y - y_{k0}, \omega\right)|^2 \hat{S}_{gkk}(\omega) \tag{28}$$

The vibration velocity level difference $\Delta\mathrm{L}_{\mathrm{v}}(\mathbf{x}_1)$ between results based on this approximation and the reference case (non-moving, but coherent axle loads) is shown in figure 59 for the three train speeds 50 km/h, 150 km/h and 300 km/h. Results are shown for receivers at different distances from the track and for the three soil types.

Most of the differences in the response due to this approximation occur for frequencies below 4 Hz for a train speed of 50 km/h (figures 59a to 59c). Above 4 Hz, the differences are small (less than 5 dB). For higher train speeds of 150 km/h and 300 km/h (figures 59d to 59f and 59g to 59i), there is a good agreement in the response above 10 Hz and 20 Hz respectively, which is where the highest response generally occurs (see figures 28 to 30).

The overall vibration velocity level considering all the frequencies bands of the current approximation is denoted as case A1+A2+A3 in tables 7 to 9 of section 3.5. The differences are less than 3 dB from the nominal case (no simplifications), and less than 1 dB from case A1+A2 (non-moving, but coherent axle loads).

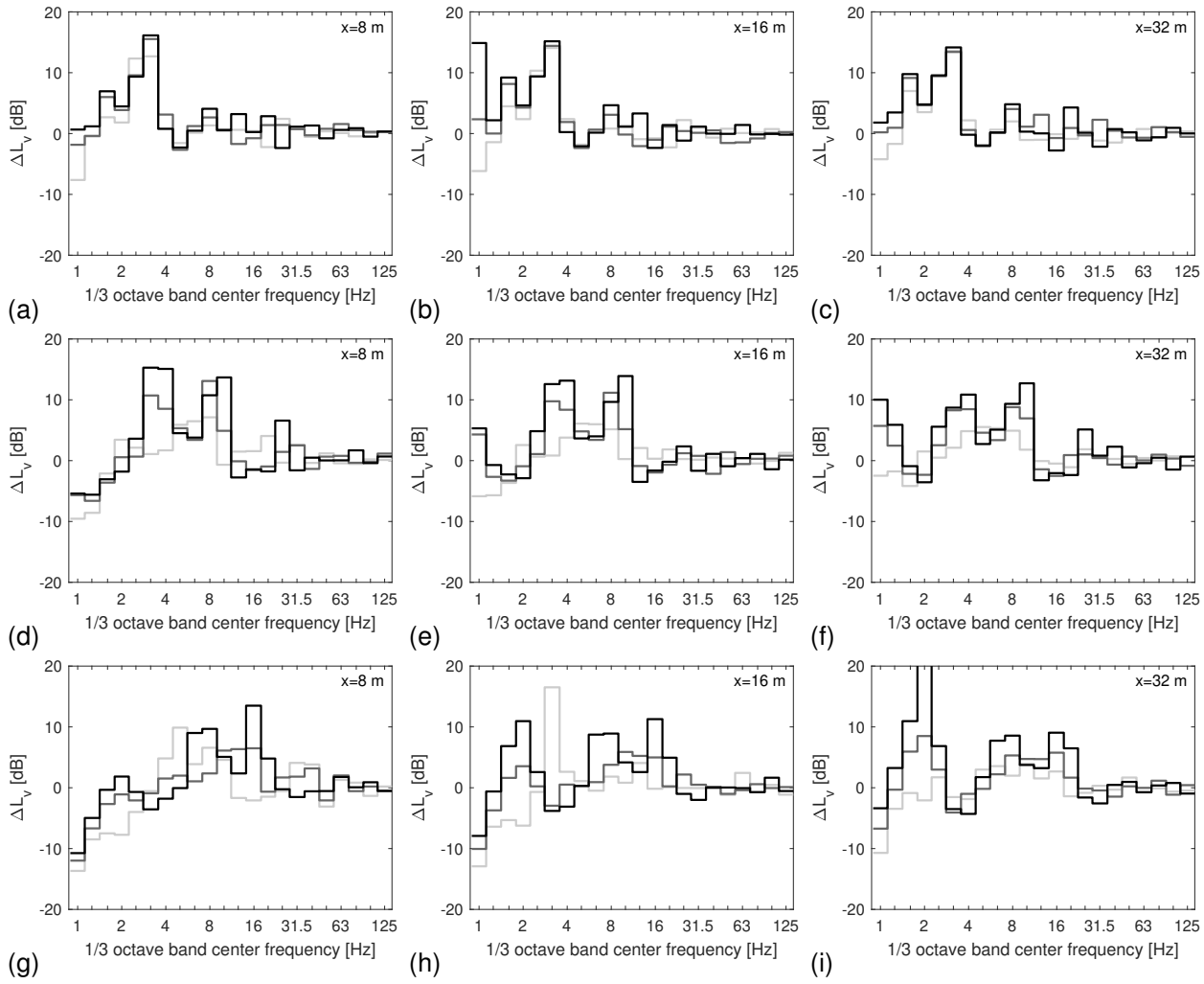

Figure 59: Vibration velocity level difference $\Delta \mathrm{L_v}(\mathbf{x}_1)$ due to the assumption of incoherent instead of coherent axle loads. Results are shown for the IC train running at (a-c) 50 km/h, (d-f) 150 km/h and (g-i) 300 km/h on the ballasted track supported by soft (light grey line), medium (dark grey line) and stiff (black line) soil. Receivers are located at (a,d,g) 8 m, (b,e,h) 16 m and (c,f,i) 32 m from the track.

3.5 Summary

The effect of three modelling simplifications on the vibration velocity level was studied in this section: (1) track compliance in a stationary versus moving frame of reference, (2) fixed (non-moving) positions for the dynamic axle loads (i.e. low-speed approximation) and (3) incoherent versus coherent axle loads. Of these three approximations, the low-speed approximation has the largest influence on the vibration velocity level, whereas the assumption of incoherent axle loads mainly affects the response at low frequencies. The effect of the train speed on the track compliance is negligible.

The combined effect of all three approximations is shown in figures 60 (soft soil), 61 (medium soil) and 62 (stiff soil) for the IC train running at 50 km/h, 150 km/h and 300 km/h on the ballasted track. Although there are significant differences in individual frequency bands, the spectrum shape is closely followed.

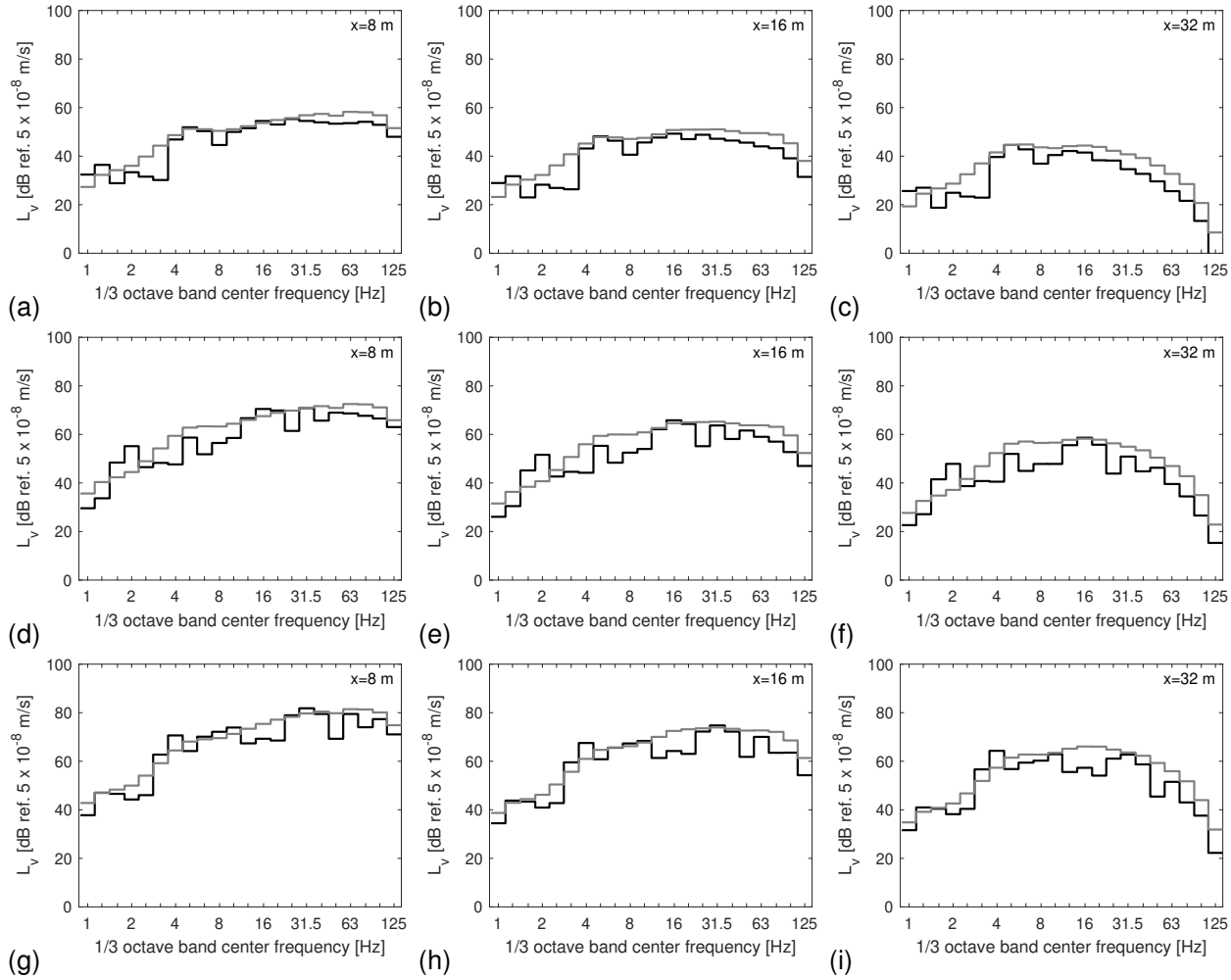

Figure 60: Free field vibration velocity level $\mathrm{L_v}(\mathbf{x}_1)$ for the IC train running at (a-c) 50 km/h, (d-f) 150 km/h and (g-i) 300 km/h on the ballasted track supported by soft soil. Receivers are located at (a,d,g) 8 m, (b,e,h) 16 m and (c,f,i) 32 m from the track. Results are computed with TRAFFIC for a moving train (black line) and using a low-speed approximation where the track compliance is computed in the stationary frame of reference assuming incoherent axle loads (grey line).

Generally, the vibration level is overestimated by a few dB when the modelling simplifications are taken into account.

In figure 63, the vibration velocity level difference $\Delta \mathrm{L_v}(\mathbf{x}_1)$ is presented for every case. It can be seen that despite the differences in individual frequency bands shown in figure 63, mainly in the low and mid frequency range, the overall spectrum shape in figures 60 to 62 is closely followed.

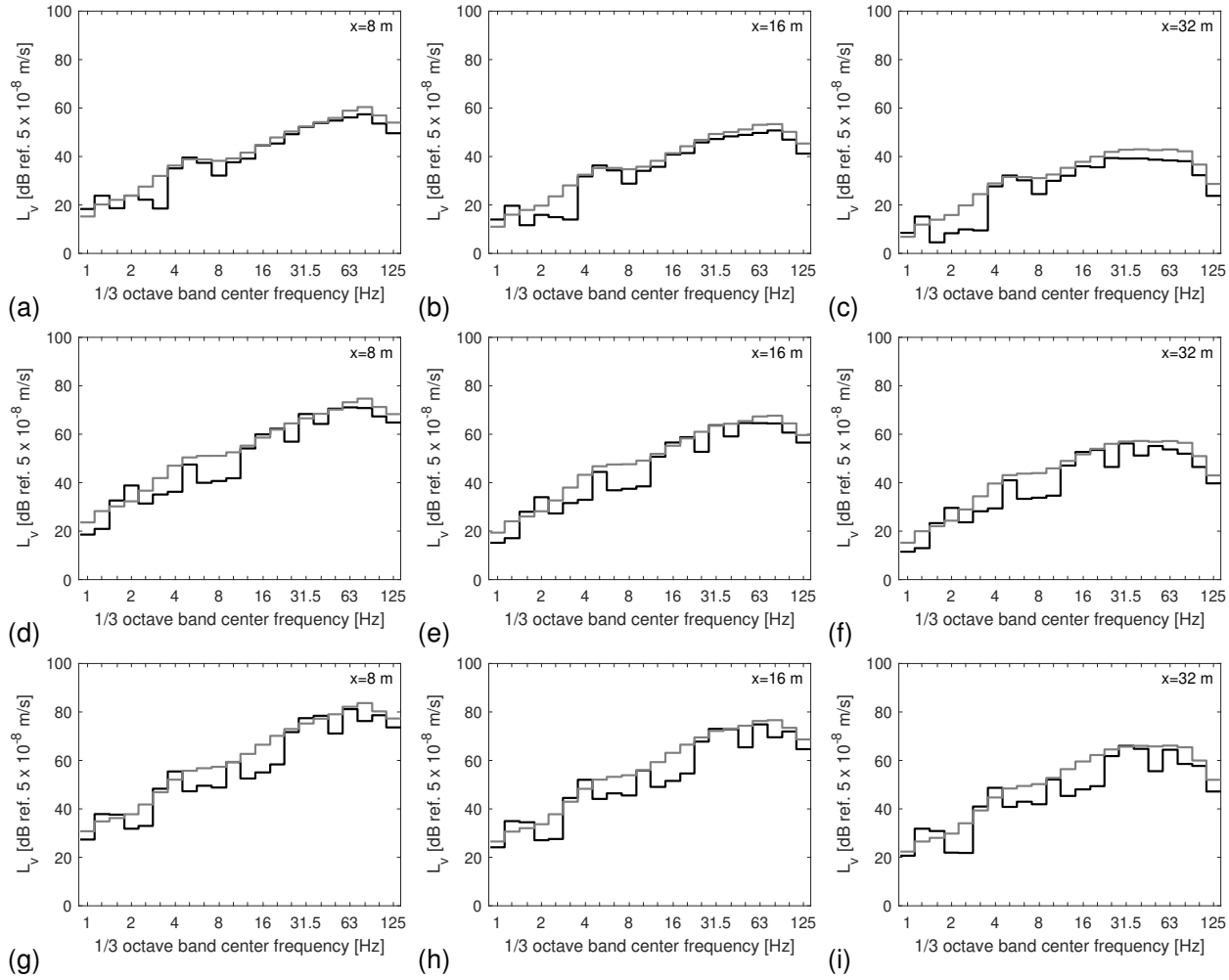

Figure 61: Free field vibration velocity level $\mathrm{L_v}(\mathbf{x}_1)$ for the IC train running at (a-c) 50 km/h, (d-f) 150 km/h and (g-i) 300 km/h on the ballasted track supported by medium soil. Receivers are located at (a,d,g) 8 m, (b,e,h) 16 m and (c,f,i) 32 m from the track. Results are computed with TRAFFIC for a moving train (black line) and using a low-speed approximation where the track compliance is computed in the stationary frame of reference assuming incoherent axle loads (grey line).

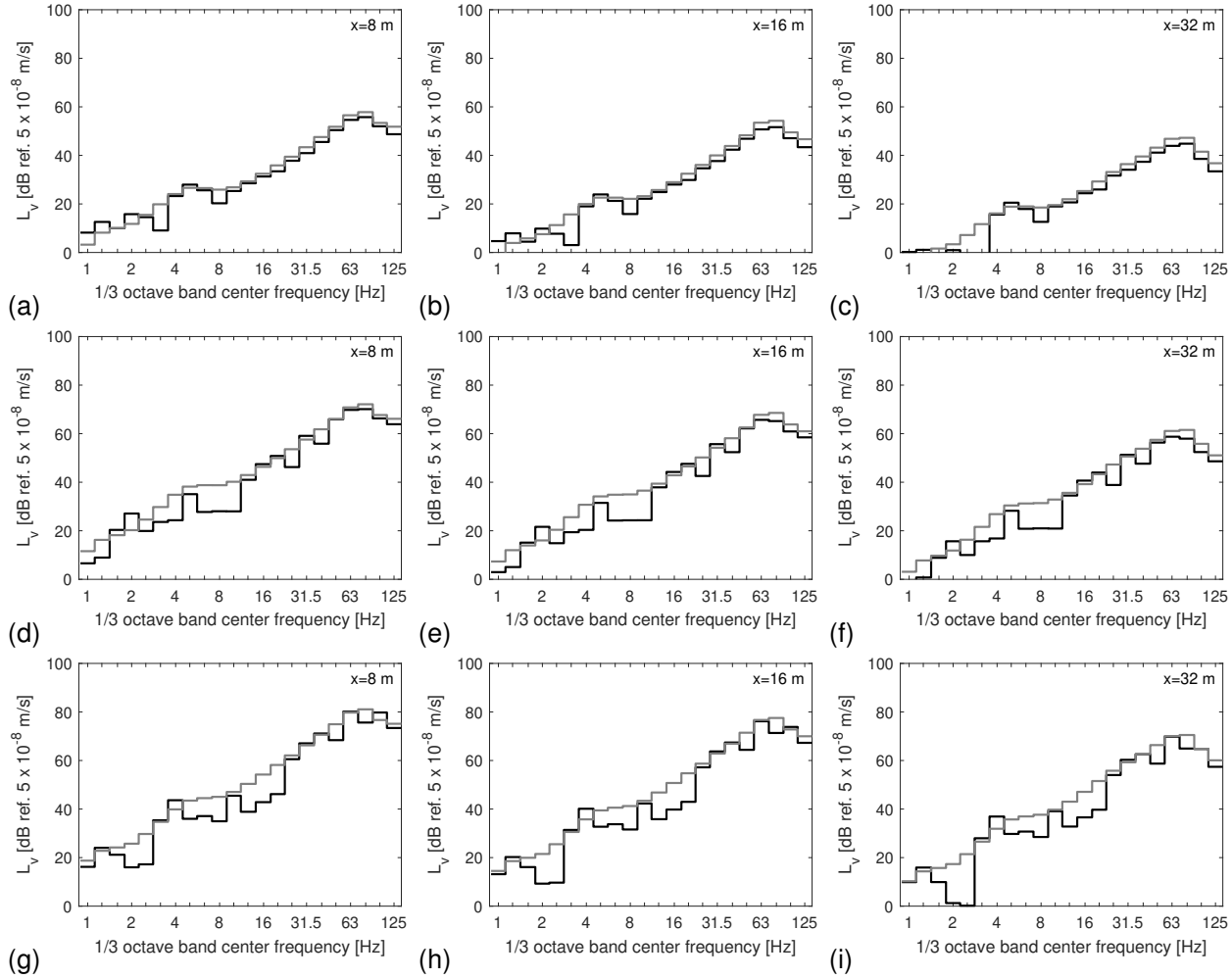

Figure 62: Free field vibration velocity level $\mathrm{L_v}(\mathbf{x}_1)$ for the IC train running at (a-c) 50 km/h, (d-f) 150 km/h and (g-i) 300 km/h on the ballasted track supported by stiff soil. Receivers are located at (a,d,g) 8 m, (b,e,h) 16 m and (c,f,i) 32 m from the track. Results are computed with TRAFFIC for a moving train (black line) and using a low-speed approximation where the track compliance is computed in the stationary frame of reference assuming incoherent axle loads (grey line).

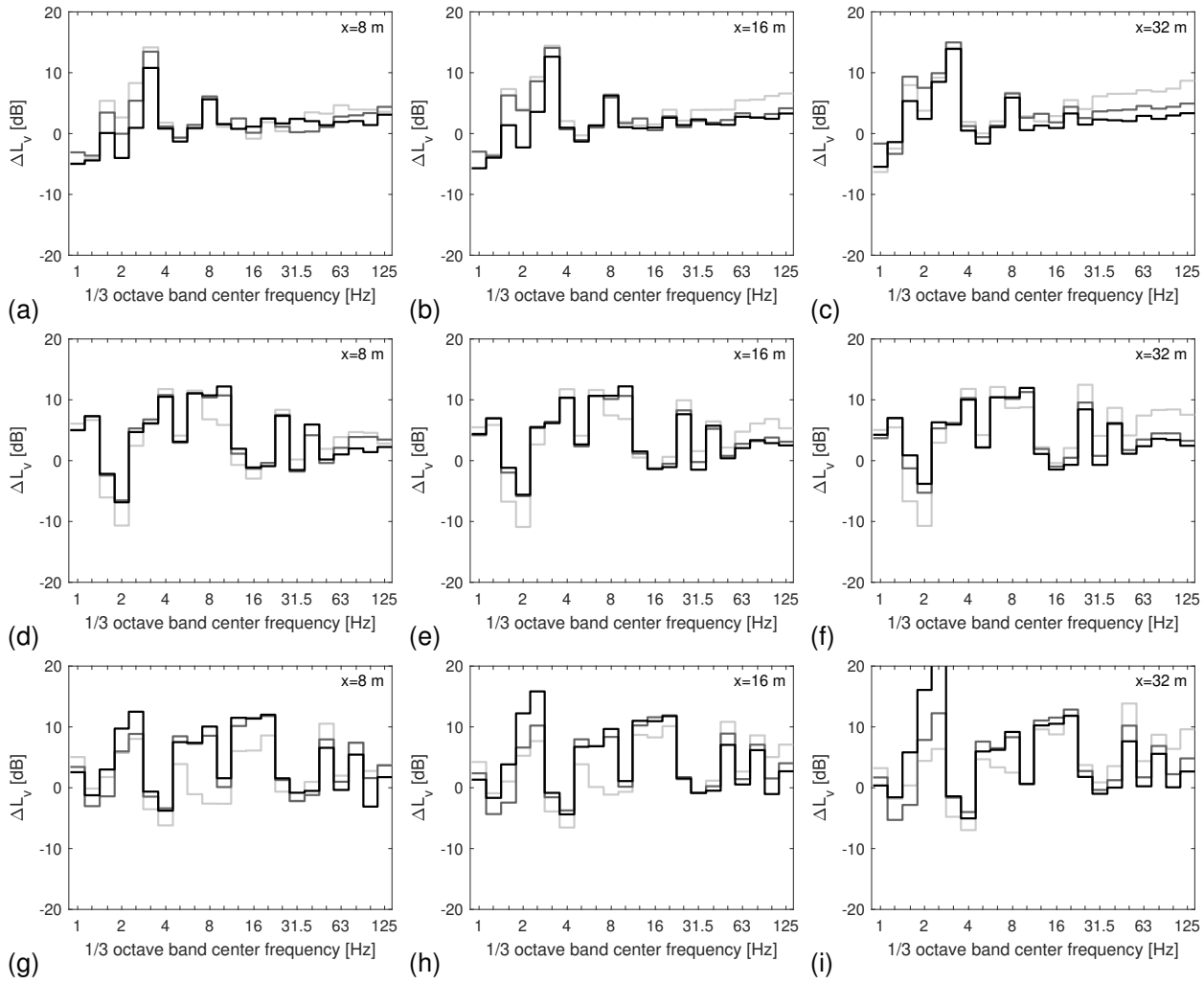

Figure 63: Vibration velocity level difference $\Delta L_v(\mathbf{x}_1)$ between predictions with the full (moving loads) and simplified model. Resuls are shown for the IC train running at (a-c) 50 km/h, (d-f) 150 km/h and (g-i) 300 km/h on the ballasted track supported by soft (light grey line), medium (dark grey line) and stiff (black line) soil. Receivers are located at (a,d,g) 8 m, (b,e,h) 16 m and (c,f,i) 32 m from the track.

In order to assess and compare the overall vibration velocity level summed over all frequency bands, the global vibration velocity level $\mathrm{L}_{\mathrm{v}}^{\mathrm{global}}(\mathbf{x}_1)$ is presented in tables 7, 8 and 9 for receivers at distances 8 m, 16 m and 32 m, respectively. In these tables, column A1 reports the global vibration level neglecting the load speed in the calculation of the track compliance; column A1+A2 reports the global vibration level when, additionally to A1, a low-speed approximation is used; column A1+A2+A3 reports the global vibration level when, additionally to A1+A2, incoherent axle loads are assumed. The results from the full model (section 2) are also given as reference, together with the vibration level difference.

The low-speed approximation (A2) leads to the largest differences between the full model and the simplified model. The vibration level difference is generally highest for the soft soil, and increases with increasing distance to the track. The overall vibration velocity level is on average 2 dB to 3 dB higher for the simplified model (A1+A2+A3) than for the full model (None). This is consistent with results presented by Verbraken [18] and demonstrates that, although the proposed modelling simplifications are a compromise to achieve efficient calculations, the differences introduced by these approximations, and shown in figure 63, are stronger in individual frequency bands, but have much less effect on the overall vibration spectrum.

Table 7: Global vibration velocity level $\mathrm{L}_{\mathrm{v}}^{\mathrm{global}}(\mathbf{x}_1)$ [dB ref. 5×10^{-8} m/s] at 8 m from the ballasted track on soft, medium and stiff soil during the passage of the IC train at 50 km/h, 150 km/h and 300 km/h. Results are computed for combinations of the three modelling assumptions: track compliance in the stationary frame of reference (A1), low-speed approximation (A2) and incoherent axle loads (A3).

Train speed	Soil type	Modelling assumptions				
		None	A1	A1+A2	A1+A2+A3	Difference
50 km/h	Soft	64.6	64.6	67.0	67.1	+2.5
	Medium	63.4	63.3	65.0	65.7	+2.3
	Stiff	60.3	60.4	61.9	62.2	+1.9
150 km/h	Soft	78.6	78.6	80.5	81.1	+2.5
	Medium	77.6	77.6	79.8	79.9	+2.3
	Stiff	75.0	74.8	76.0	76.5	+1.5
300 km/h	Soft	87.8	87.8	89.6	89.7	+1.9
	Medium	86.3	86.3	88.7	88.8	+2.5
	Stiff	84.5	84.0	85.1	85.5	+1.0

Table 8: Global vibration velocity level $\mathrm{L}_{\mathrm{v}}^{\mathrm{global}}(\mathbf{x}_1)$ [dB ref. 5×10^{-8} m/s] at 16 m from the ballasted track on soft, medium and stiff soil during the passage of the IC train at 50 km/h, 150 km/h and 300 km/h. Results are computed for combinations of the three modelling assumptions: track compliance in the stationary frame of reference (A1), low-speed approximation (A2) and incoherent axle loads (A3).

Train speed	Soil type	Modelling assumptions				
		None	A1	A1+A2	A1+A2+A3	Difference
50 km/h	Soft	58.0	58.0	61.0	61.0	+3.0
	Medium	57.4	57.4	60.6	59.9	+2.5
	Stiff	56.2	56.2	58.4	58.7	+2.5
150 km/h	Soft	71.9	71.9	73.9	74.7	+2.8
	Medium	74.7	71.7	74.2	74.2	+2.5
	Stiff	70.5	70.3	72.7	72.9	+2.4
300 km/h	Soft	80.4	80.4	82.8	83.0	+2.6
	Medium	80.4	80.2	82.9	83.0	+2.6
	Stiff	79.8	79.4	82.1	81.9	+2.1

Table 9: Global vibration velocity level $\mathrm{L}_{\mathrm{v}}^{\mathrm{global}}(\mathbf{x}_1)$ [dB ref. 5×10^{-8} m/s] at 32 m from the ballasted track on soft, medium and stiff soil during the passage of the IC train at 50 km/h, 150 km/h and 300 km/h. Results are computed for combinations of the three modelling assumptions: track compliance in the stationary frame of reference (A1), low-speed approximation (A2) and incoherent axle loads (A3).

Train speed	Soil type	Modelling assumptions				
		None	A1	A1+A2	A1+A2+A3	Difference
50 km/h	Soft	51.0	50.9	54.2	53.9	+2.9
	Medium	47.9	47.9	51.2	51.5	+3.6
	Stiff	49.4	49.5	52.5	52.0	+2.6
150 km/h	Soft	63.3	63.2	65.9	67.1	+3.8
	Medium	62.7	62.6	65.3	65.6	+2.9
	Stiff	63.6	63.6	66.4	66.3	+2.7
300 km/h	Soft	71.1	71.1	73.8	74.5	+3.4
	Medium	71.3	71.1	74.2	74.2	+2.9
	Stiff	73.0	72.6	75.2	75.2	+2.2

4. NUMERICAL VALIDATION

4.1 Introduction

In this section, a numerical validation of the prototype vibration prediction tool is presented. The line source transfer mobility, vibration velocity level and force density are computed for the 18 cases introduced in section 2. This validation focuses on the correct implementation and solution of the train-track-soil interaction problem in the prototype tool, and therefore results are compared with predictions with TRAFFIC taking all modelling simplifications from section 3 into account. Hence, the comparison presented in this section is expected to be good, and the differences between the full and simplified model presented in section 3 should be kept in mind while reading.

Contrary to TRAFFIC, the prototype vibration prediction tool uses pre-computed soil impedance and transfer functions in the frequency-wavenumber domain from the numerical database presented in Deliverable D2.1 [17]. These pre-computed functions are available for the soft, medium and stiff soil, and for track widths of 3 m, 4.5 m and 6 m. As the width of the track-soil interface for the ballasted and slab track equals 3.6 m and 3.4 m respectively, the pre-computed functions for a track width of 3 m are used, while the actual track width is used in TRAFFIC.

The section is organized as follows. First, the influence of the width of the track-soil interface on the soil impedance and transfer functions is presented. Next, the line source transfer mobility, vibration velocity level and force density computed with the prototype vibration prediction tool and TRAFFIC are compared for the ballasted track and the slab track. We also take the opportunity in this section to highlight the influence of soil stiffness on the line source transfer mobility, as well as the influence of soil stiffness and train speed on the vibration velocity level and force density.

4.2 Pre-computed soil impedance and transfer functions

For the numerical validation of the prototype vibration prediction tool, the modelling simplifications discussed in section 3 are also included in TRAFFIC. Hence, differences in the results obtained with both models are mostly due to the fact that pre-computed soil impedance and transfer functions are used by the prototype vibration prediction tool. These functions are computed in the frequency-wavenumber domain for fixed widths of the track-soil interface (3 m, 4.5 m and 6 m for single tracks), as discussed in section 5 of Deliverable D2.1 [17]. The width of the track-soil interface equals 3.6 m for the ballasted track (table 1) and 3.4 m for the slab track (table 2). In TRAFFIC, the soil impedance and transfer functions are computed with the actual track width, while in the prototype vibration prediction tool, pre-computed values are used for a width of 3 m (closest to the actual width).

The 2×2 soil stiffness matrix $\tilde{\mathbf{K}}_{\mathrm{s}}(k_y, \omega)$ contains the reaction forces due to a unit vertical displacement and unit rotation of the track-soil interface and is computed in the frequency-wavenumber domain (see section 4.2.3 in Deliverable D1.1 [2]). As the vertical and rotational motion are uncoupled, $\tilde{\mathbf{K}}_{\mathrm{s}}(k_y, \omega)$ is a diagonal matrix. We focus on the vertical soil stiffness $\tilde{k}_{\mathrm{s}zz}(k_y, \omega)$ [N/m] defined as the total vertical reaction force due to a unit vertical displacement of the track-soil interface.

The vertical soil mobility is obtained as $\mathrm{i}\omega / \tilde{k}_{\mathrm{s}zz}(k_y, \omega)$ [(m/s)/N] and is shown in figure 64 at 1 Hz, 10 Hz and 100 Hz as a function of the dimensionless wavenumber $\bar{k}_y = k_y C_{\mathrm{s}} / \omega$. The soil mobility is computed

for the soft, medium and stiff soil, and for track widths equal to 3 m, 3.4 m and 3.6 m. The peak in the soil mobility around $\bar{k}_y = 1$ is due to the propagation of Rayleigh waves in the soil. For $\bar{k}_y > 1$, all waves are evanescent and the soil mobility rapidly decreases. Furthermore, the soil mobility increases with decreasing soil stiffness and increasing frequency. Regardless of the soil stiffness, the soil mobility always decreases with increasing track width. However, since the vertical soil mobilities for track widths equal to 3 m, 3.4 m and 3.6 m are very similar, only a slight increase of the dynamic axle loads is expected with increasing track width.

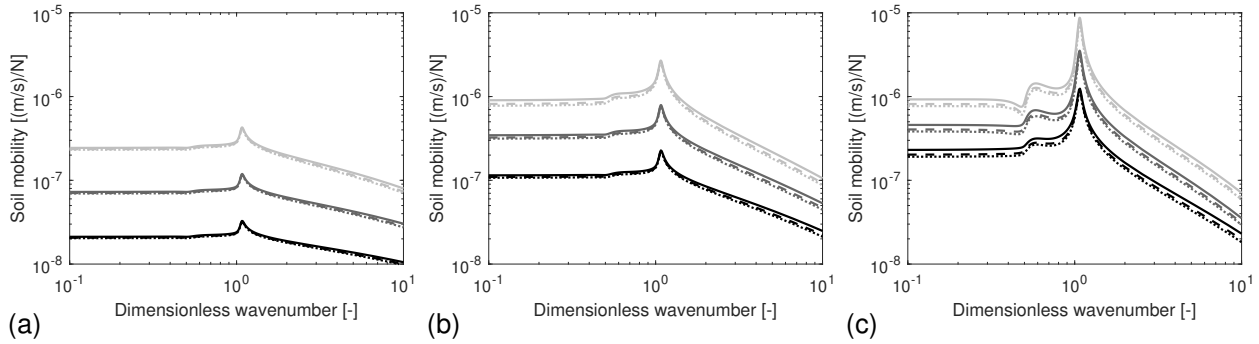

Figure 64: Vertical soil mobility $\mathrm{i}\omega/\tilde{k}_{szz}(k_y,\omega)$ as a function of the dimensionless wavenumber $\bar{k}_y$ at (a) 1 Hz, (b) 10 Hz and (c) 100 Hz. Results are computed for the soft, medium and stiff soil (light grey to black lines) and for track widths equal to 3 m (solid line), 3.4 m (dashed line) and 3.6 m (dotted line).

The vertical track-soil transfer mobility $\tilde{h}_{szz}(x,k_y,\omega)$ [(m/s)/N] is defined as the vertical free field velocity due to a unit vertical load applied to the track-soil interface and is computed in the frequency-wavenumber domain (see section 4.2.4 in Deliverable D1.1 [2]).

Figure 65 shows the transfer mobility at $x = 8$ m as a function of the dimensionless wavenumber $\bar{k}_y$ at 1 Hz, 10 Hz and 100 Hz. The peak in the transfer mobility around $\bar{k}_y = 1$ is due to the propagation of Rayleigh waves in the soil, and the peak around $\bar{k}_y = 0.5$ is observed because the dilatational wave becomes evanescent. At 1 Hz, the transfer mobility is highest for the soft soil and the influence of the track width is very limited. At 10 Hz and 100 Hz, the transfer mobility becomes negligible above $\bar{k}_y = 1$ since all waves are evanescent. At 10 Hz, the influence of the track width is limited, while at 100 Hz the transfer mobility decreases with increasing track width.

Similar observations can be made on figures 66 and 67, which show the transfer mobility at $x = 16$ m and $x = 32$ m, respectively. Due to material damping, the transfer mobility decreases rapidly with increasing distance from the track for the soft soil at 100 Hz.

It can be concluded that a slight change in the width of the track-soil interface does not much affect the soil impedance and transfer functions. Generally, the soil mobility and transfer mobility decrease with increasing track width, particularly at high frequencies. The effect of the track width on the vibration velocity level during a train passage is, however, difficult to predict, as it depends on the dynamic axle loads (which increase with increasing track width) and the transfer mobility (which decreases with increasing track width).

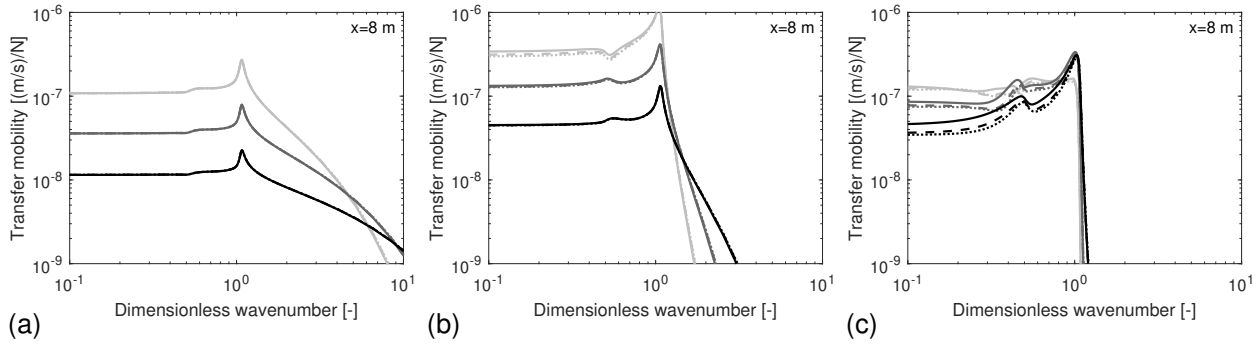

Figure 65: Vertical track-soil transfer mobility $\tilde{h}_{szz}(x, k_y, \omega)$ as a function of the dimensionless wavenumber $\bar{k}_y$ at (a) 1 Hz, (b) 10 Hz and (c) 100 Hz for a receiver at 8 m from the centre of the track-soil interface. Results are computed for the soft, medium and stiff soil (light grey to black lines) and for track widths equal to 3 m (solid line), 3.4 m (dashed line) and 3.6 m (dotted line).

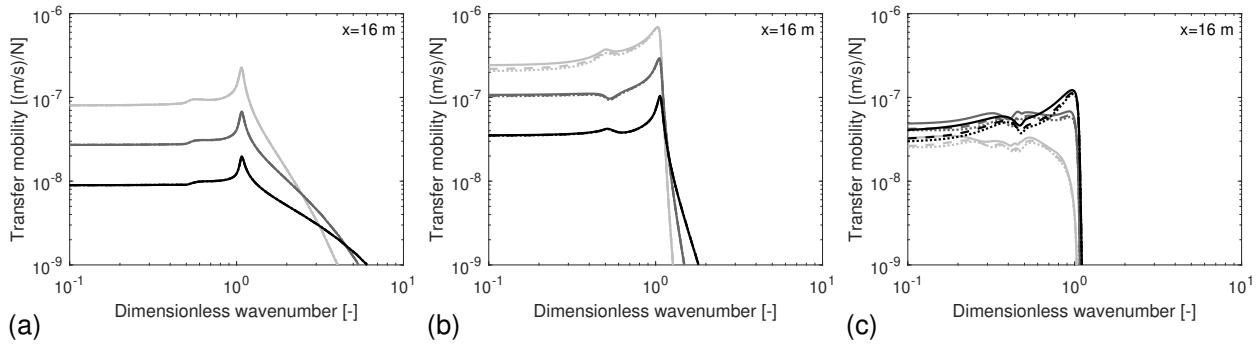

Figure 66: Vertical track-soil transfer mobility $\tilde{h}_{szz}(x, k_y, \omega)$ as a function of the dimensionless wavenumber $\bar{k}_y$ at (a) 1 Hz, (b) 10 Hz and (c) 100 Hz for a receiver at 16 m from the centre of the track-soil interface. Results are computed for the soft, medium and stiff soil (light grey to black lines) and for track widths equal to 3 m (solid line), 3.4 m (dashed line) and 3.6 m (dotted line).

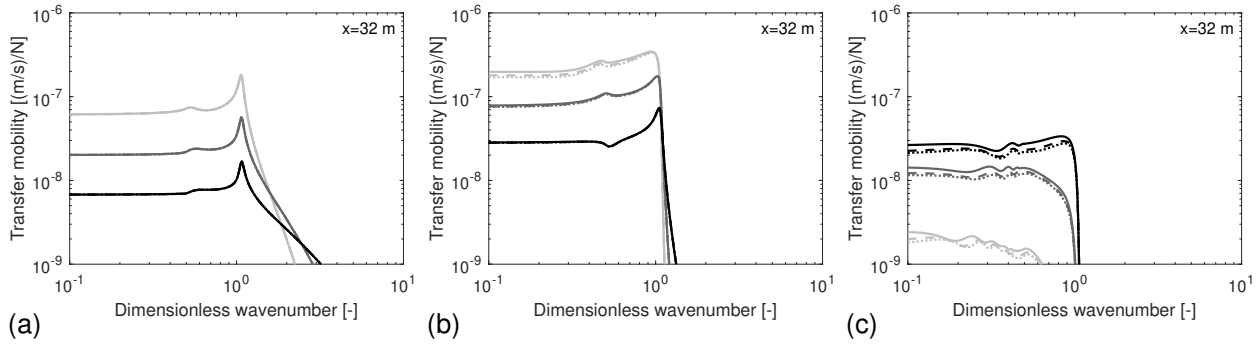

Figure 67: Vertical track-soil transfer mobility $\tilde{h}_{szz}(x, k_y, \omega)$ as a function of the dimensionless wavenumber $\bar{k}_y$ at (a) 1 Hz, (b) 10 Hz and (c) 100 Hz for a receiver at 32 m from the centre of the track-soil interface. Results are computed for the soft, medium and stiff soil (light grey to black lines) and for track widths equal to 3 m (solid line), 3.4 m (dashed line) and 3.6 m (dotted line).

4.3 Validation for the ballasted track

In the following, results obtained with the prototype vibration prediction tool are compared to TRAFFIC; identical modelling assumptions (see section 3) are made in both models. The prototype tool, however, uses pre-computed soil impedance and transfer functions for a track width of 3 m, while TRAFFIC considers the actual track width equal to 3.6 m. The comparison is presented in terms of line source transfer mobility, vibration velocity level and force density for the ballasted track (subsection 2.2.1).

4.3.1 Line source transfer mobility

The line source transfer mobility $\mathrm{TM_L}(\mathbf{X}, \mathbf{x}_1)$ is shown in figure 68 at 8 m, 16 m and 32 m from the track on soft, medium and stiff soil. At low frequencies, the line source transfer mobility is highest for the soft soil and reaches its maximum around 20 Hz at 8 m, 16 Hz at 16 m and 12.5 Hz at 32 m. Above these frequencies, the line source transfer mobility decreases rapidly due to material damping in the soil. For the medium and stiff soil, similar trends are observed, but compared to the soft soil, the maximum value is reached at twice and four times the respective frequencies. As the wavelength in the soil at a particular frequency increases with increasing soil stiffness, the effect of material damping is less pronounced for the medium and stiff soil due to the lower number of dissipative cycles.

The results computed with the prototype tool and TRAFFIC are in excellent agreement up to 10 Hz. At higher frequencies, slightly higher values (1 dB to 3 dB) are predicted with the prototype tool due to the lower track width; the discrepancy is larger at 32 m than at 8 m from the track. Overall, the line source transfer mobility computed with the two models is in very good agreement, which proves that the track-soil system is correctly modelled in the prototype vibration prediction tool.

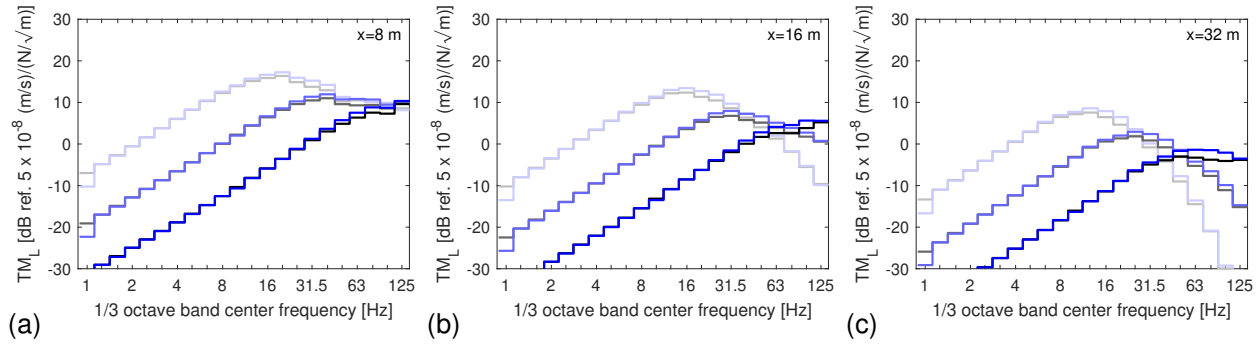

Figure 68: Line source transfer mobility $\mathrm{TM_L}(\mathbf{X}, \mathbf{x}_1)$ of the ballasted track supported by soft, medium and stiff soil (light to dark lines) for receivers at (a) 8 m, (b) 16 m and (c) 32 m from the track. Results are computed with TRAFFIC (grey lines) and the prototype vibration prediction tool (blue lines).

4.3.2 Vibration velocity level

Figure 69 shows the vibration velocity level $\mathrm{L_v}(\mathbf{x}_1)$ at 8 m, 16 m and 32 m from the track during the passage of the IC train at 50 km/h, 150 km/h and 300 km/h. The vibration velocity levels for the soft, medium and stiff soil are shown on the same figure. For a train speed equal to 50 km/h, the vibration velocity level is highest for the soft soil up to 30 Hz. For the medium and stiff soil, the vibration velocity level reaches its

maximum value at the P2 resonance close to 80 Hz. Around this frequency, the vibration velocity level is similar for the three soils at 8 m, while at 16 m the vibration velocity level is lower for the soft soil due to the influence of material damping. At 32 m, the highest vibration velocity level is predicted for the stiff soil at the P2 resonance, which is approximately 8 dB higher than the level for the medium soil and 22 dB higher than that for the soft soil.

For higher train speeds, the vibration velocity level increases, but the trends are very similar to those found for the vibration velocity level for a train speed of 50 km/h. This is illustrated by figure 70, which shows the vibration velocity level for the three train speeds on the same figure. It is concluded that between 30 Hz and 125 Hz the vibration velocity level increases by approximately 16 dB when increasing the train speed from 50 km/h to 150 km/h, independent of the soil stiffness and the receiver location. An additional increase of approximately 8 dB is observed by increasing the train speed to 300 km/h.

The results computed with the prototype tool and TRAFFIC are in very good agreement. Below 30 Hz, the

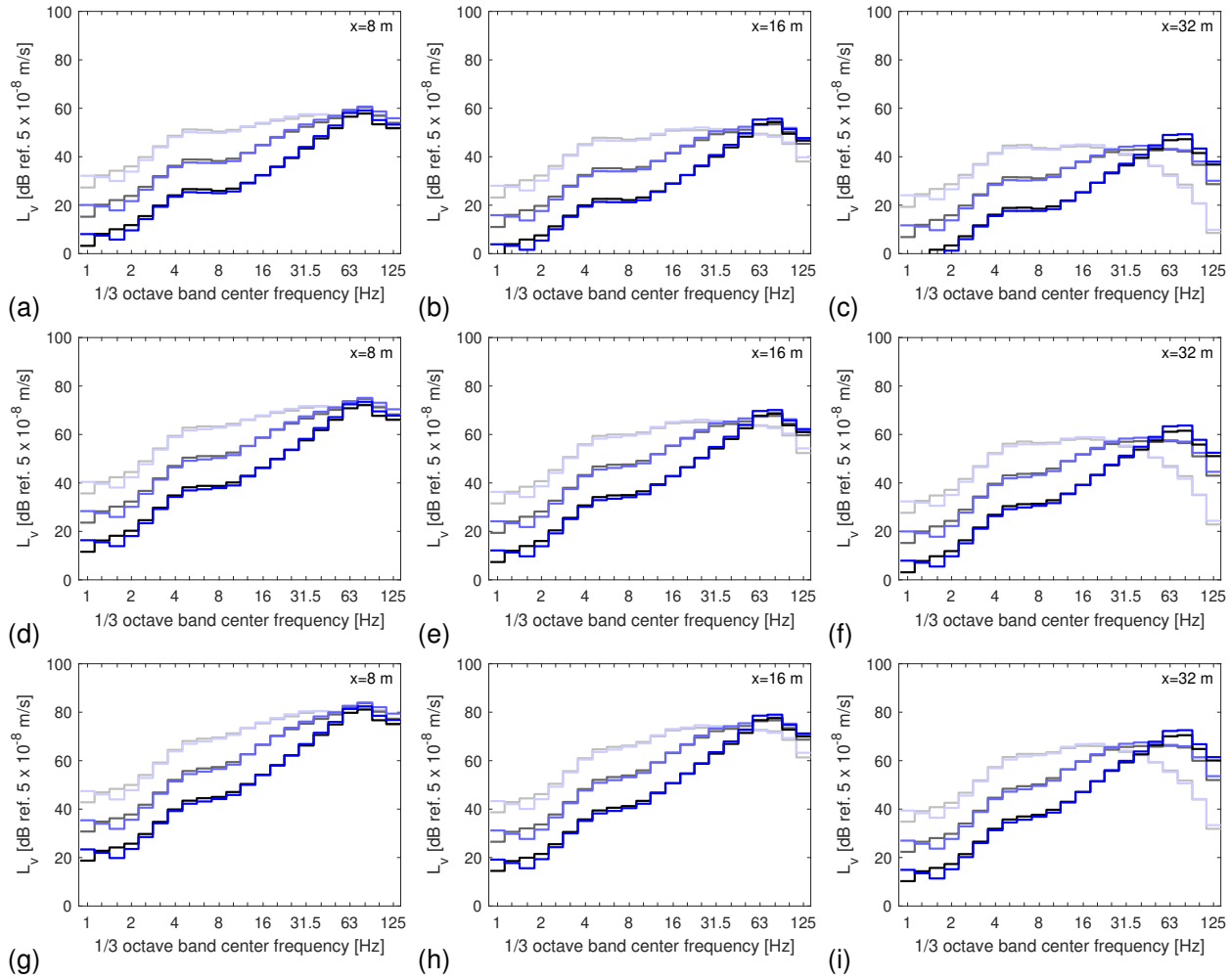

Figure 69: Vibration velocity level $\mathrm{L_v}(\mathbf{x}_1)$ for the IC train running at (a-c) 50 km/h, (d-f) 150 km/h and (g-i) 300 km/h on the ballasted track supported by soft, medium and stiff soil (light to dark lines). Receivers are located at (a,d,g) 8 m, (b,e,h) 16 m and (c,f,i) 32 m from the track. Results are computed with TRAFFIC (grey lines) and the prototype vibration prediction tool (blue lines).

vibration velocity level predicted with TRAFFIC is 1 dB to 2 dB higher than found using the prototype tool. At high frequencies, the prototype tool tends to predict a slightly higher vibration velocity level.

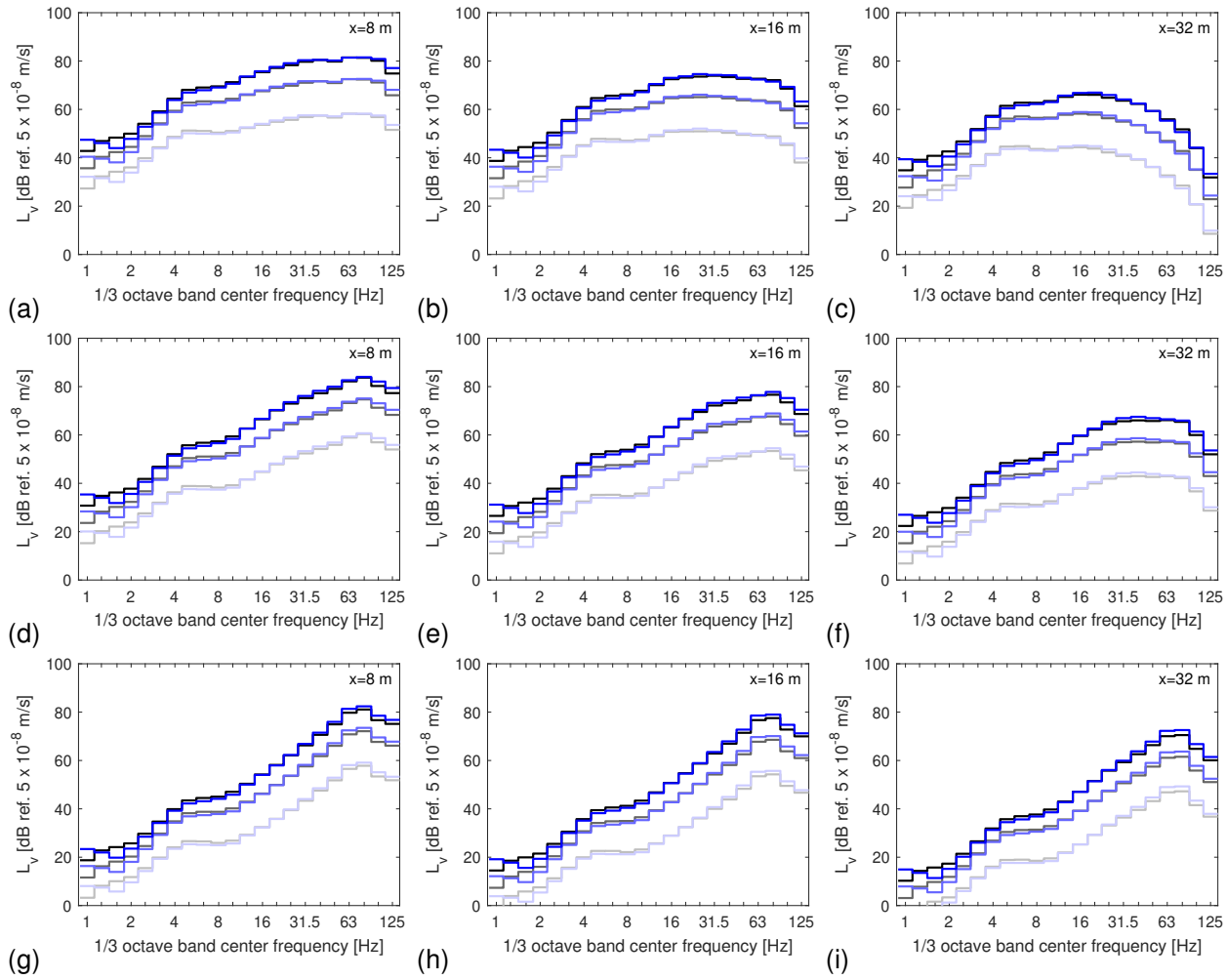

Figure 70: Vibration velocity level $\mathrm{L_v}(\mathbf{x}_1)$ for the IC train running at 50 km/h, 150 km/h and 300 km/h (light to dark lines) on the ballasted track supported by (a-c) soft, (d-f) medium and (g-i) stiff soil. Receivers are located at (a,d,g) 8 m, (b,e,h) 16 m and (c,f,i) 32 m from the track. Results are computed with TRAFFIC (grey lines) and the prototype vibration prediction tool (blue lines).

4.3.3 Force density

The force density $\mathrm{L_F}(\mathbf{X}, \mathbf{x}_1)$ is estimated using the FRA procedure (equation (20)). Figure 71 shows the force density $\mathrm{L_F}(\mathbf{X}, \mathbf{x}_1)$ at 8 m, 16 m and 32 m from the track during the passage of the IC train at 50 km/h, 150 km/h and 300 km/h. The force density for the soft, medium and stiff soil is shown in the same figure. Since the influence of the soil stiffness on the dynamic axle loads is limited below 50 Hz (figures 21 to 23), the force density is almost identical for the three soil types up to this frequency. At high frequencies, the force density is higher for the soft soil. Furthermore, the force density is almost identical for the three receiver locations up to 80 Hz. The peaks around 5 Hz and 80 Hz correspond to dips in the

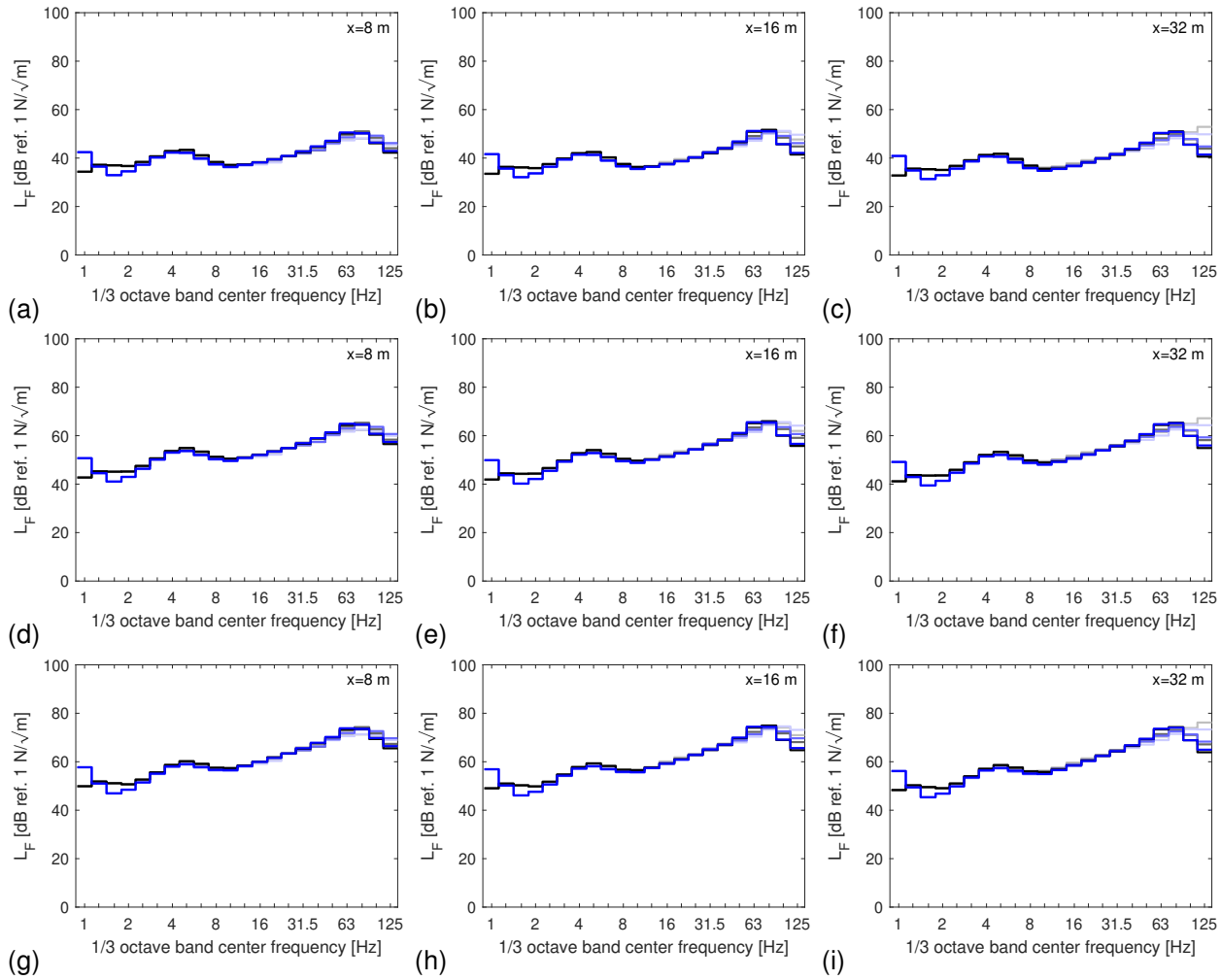

Figure 71: Force density $\mathrm{L_F}(\mathbf{X}, \mathbf{x}_1)$ for the IC train running at (a-c) 50 km/h, (d-f) 150 km/h and (g-i) 300 km/h on the ballasted track supported by soft, medium and stiff soil (light to dark lines). Receivers are located at (a,d,g) 8 m, (b,e,h) 16 m and (c,f,i) 32 m from the track. Results are computed with TRAFFIC (grey lines) and the prototype vibration prediction tool (blue lines).

vehicle compliance and total compliance, respectively.

The aforementioned observations are independent of the train speed. The influence of the train speed on the force density is shown in figure 72. Since the line source transfer mobility $\mathrm{TM_L}(\mathbf{X}, \mathbf{x}_1)$ is not affected by the train speed, the differences are solely due to the increasing vibration velocity level $\mathrm{L_v}(\mathbf{x}_1)$ with increasing speed, as was discussed in figure 70.

The force densities computed with the prototype vibration prediction tool and TRAFFIC are in very good agreement. The discrepancy is limited to 3 dB in each frequency band and is due to the selected track width for the pre-computed soil impedance and transfer functions.

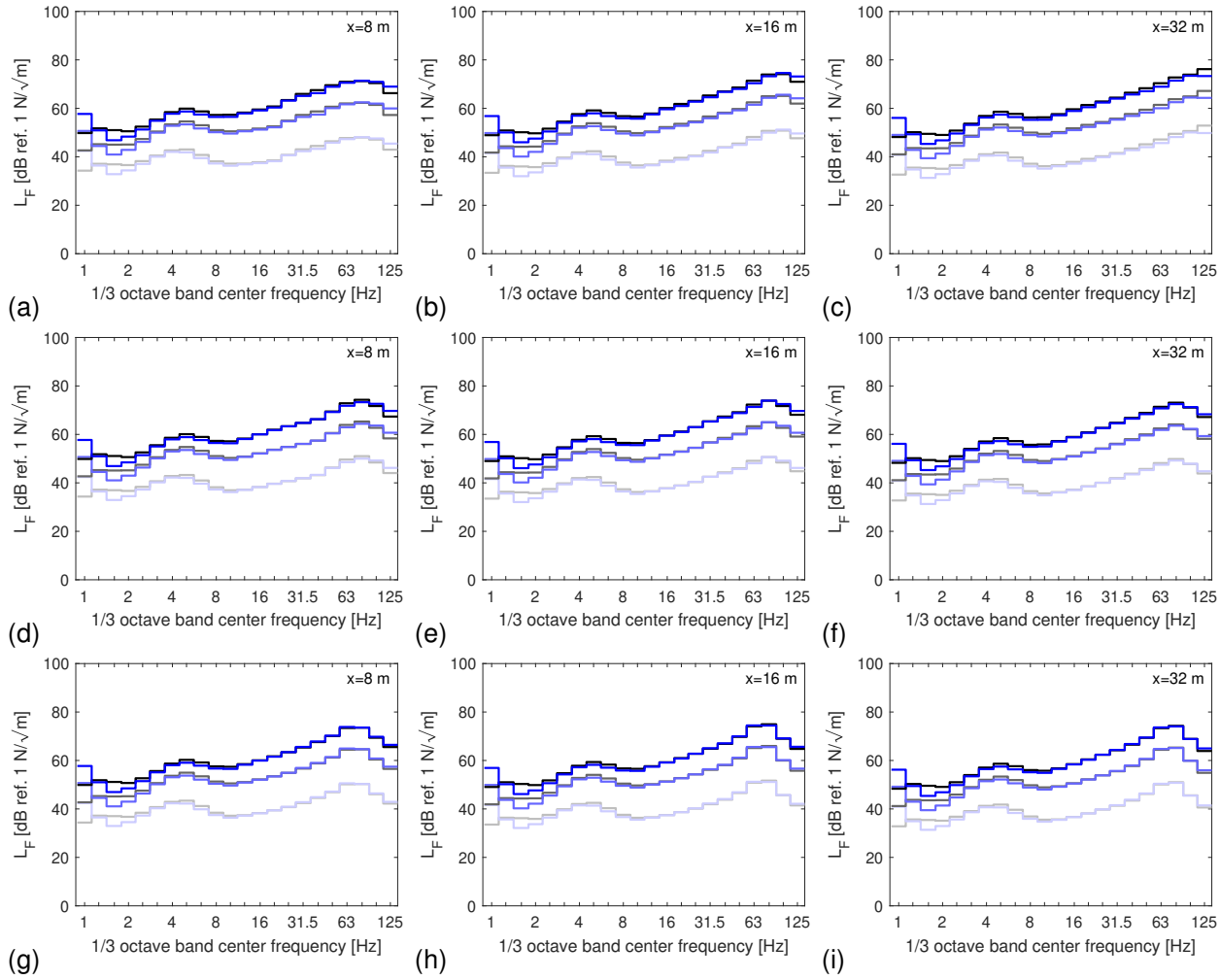

Figure 72: Force density $\mathrm{L_F}(\mathbf{X}, \mathbf{x}_1)$ for the IC train running at 50 km/h, 150 km/h and 300 km/h (light to dark lines) on the ballasted track supported by (a-c) soft, (d-f) medium and (g-i) stiff soil. Receivers are located at (a,d,g) 8 m, (b,e,h) 16 m and (c,f,i) 32 m from the track. Results are computed with TRAFFIC (grey lines) and the prototype vibration prediction tool (blue lines).

4.4 Validation for the slab track

The comparison between results obtained with the prototype vibration prediction tool and TRAFFIC is performed for the slab track. The prototype tool uses pre-computed soil impedance and transfer functions for a width of the track-soil interface equal to 3 m, while the actual track width of 3.4 m is used in the TRAFFIC computations. The comparison between the two models is presented in terms of line source transfer mobility, vibration velocity level and force density.

4.4.1 Line source transfer mobility

The line source transfer mobility $\mathrm{TM_L}(\mathbf{X}, \mathbf{x}_1)$ is shown in figure 73 at 8 m, 16 m and 32 m from the track on soft, medium and stiff soil. At low frequencies, the line source transfer mobility is highest for the soft soil and reaches its maximum around 12.5 Hz, after which it decreases rapidly due to material damping in the soil. For the medium soil, the line source transfer mobility has its maximum around 25 Hz, while for the stiff soil the maximum is found around 80 Hz at 8 m, 63 Hz at 16 m and 50 Hz at 32 m.

The results obtained with the prototype vibration prediction tool and TRAFFIC are in very good agreement. At high frequencies, the difference is around 1 dB for the stiff soil, while there is no noticeable difference for the medium and soft soil.

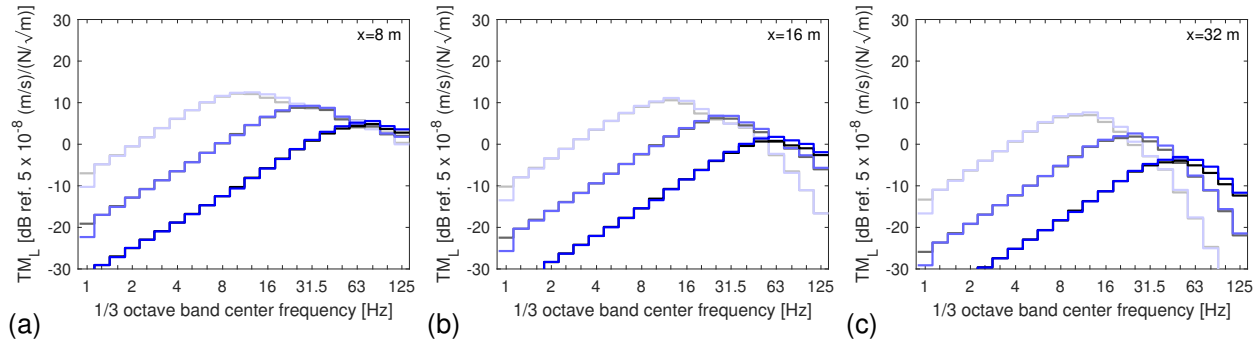

Figure 73: Line source transfer mobility $\mathrm{TM_L}(\mathbf{X}, \mathbf{x}_1)$ of the slab track supported by soft, medium and stiff soil (light to dark lines) for receivers at (a) 8 m, (b) 16 m and (c) 32 m from the track. Results are computed with TRAFFIC (grey lines) and the SILVARSTAR prototype vibration prediction tool (blue lines).

4.4.2 Vibration velocity level

Figure 74 shows the vibration velocity level $\mathrm{L_v}(\mathbf{x}_1)$ at 8 m, 16 m and 32 m from the track during the passage of the IC train at 50 km/h, 150 km/h and 300 km/h. The vibration velocity levels for the soft, medium and stiff soil are shown on the same figure. The P2 resonance of the unsprung mass on the track is clearly observed for the medium and stiff soil around 90 Hz, which is slightly higher than for the ballasted track. At 8 m, the vibration velocity level around the P2 resonance is similar for each soil type and increases with increasing train speed. At 16 m and 32 m, the effect of material damping in the soil is observed at high frequencies, particularly for the soft soil, resulting in significantly lower vibration velocity levels.

The effect of the train speed on the vibration velocity level is shown in figure 75, where results for the three train speeds are grouped together in one figure. The train speed mainly affects the amplitude of the

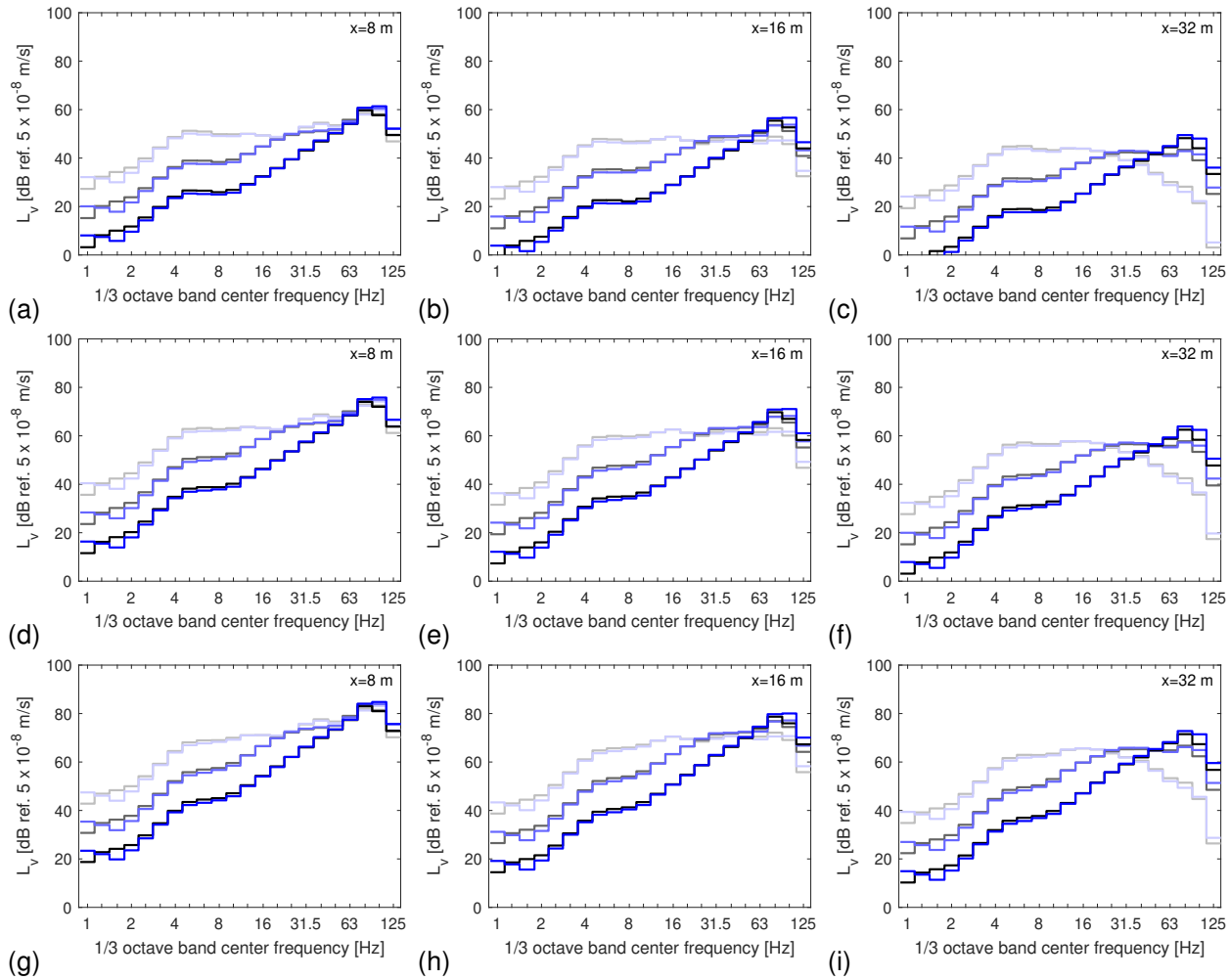

Figure 74: Vibration velocity level $\mathrm{L_v}(\mathbf{x}_1)$ for the IC train running at (a-c) 50 km/h, (d-f) 150 km/h and (g-i) 300 km/h on the slab track supported by soft, medium and stiff soil (light to dark lines). Receivers are located at (a,d,g) 8 m, (b,e,h) 16 m and (c,f,i) 32 m from the track. Results are computed with TRAFFIC (grey lines) and the prototype vibration prediction tool (blue lines).

vibration velocity level at high frequencies. Increasing the train speed from 50 km/h to 150 km/h results in an increase of 16 dB on the vibration velocity level. An additional 8 dB is added by increasing the train speed to 300 km/h. Similar observations were made for the ballasted track in figure 70.

The results computed with the prototype vibration prediction tool and TRAFFIC are in very good agreement. The prototype tool tends to predict higher vibration velocity levels at high frequencies (differences up to 4 dB).

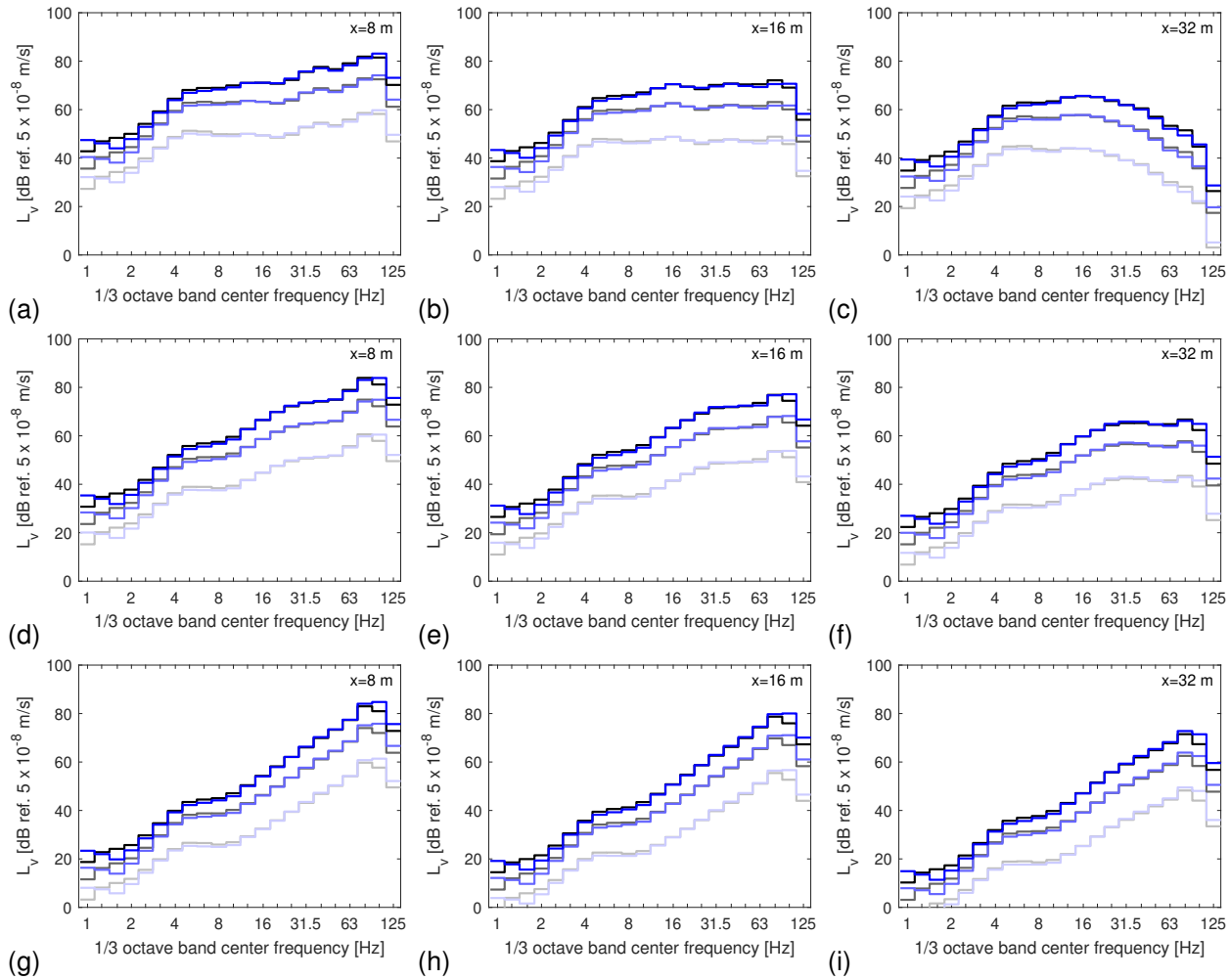

Figure 75: Vibration velocity level $\mathrm{L_v}(\mathbf{x}_1)$ for the IC train running at 50 km/h, 150 km/h and 300 km/h (light to dark lines) on the slab track supported by (a-c) soft, (d-f) medium and (g-i) stiff soil. Receivers are located at (a,d,g) 8 m, (b,e,h) 16 m and (c,f,i) 32 m from the track. Results are computed with TRAFFIC (grey lines) and the prototype vibration prediction tool (blue lines).

4.4.3 Force density

The force density is shown in figure 76 based on the responses at 8 m, 16 m and 32 m from the track. The results for the soft, medium and stiff soil are shown on the same figure. The peak around 5 Hz corresponds to a local minimum in the vehicle compliance related to the suspension stiffness of the vehicle, and was also observed in the force density for the ballasted track. The peak around 90 Hz corresponds to the P2 resonance where the total compliance has its minimum. Below 30 Hz, the force density is nearly identical for the three soils. At higher frequencies, deviations up to 5 dB are observed between the force density for the soft and the stiff soil. Furthermore, a good agreement is found between the force density at three distances from the track.

The influence of the train speed is shown in figure 77. Differences of approximately 16 dB are observed in every frequency band above 10 Hz between the force density for the IC train running at 150 km/h compared to a train speed of 50 km/h. For 300 km/h the corresponding difference is 24 dB.

The force density computed with the prototype vibration prediction tool is a few dB lower at low frequencies than the TRAFFIC results, while at high frequencies differences between -1 dB and +3 dB are observed. The discrepancies are attributed to the different track width assumed in the prototype vibration prediction tool by using pre-computed soil impedance and transfer functions.

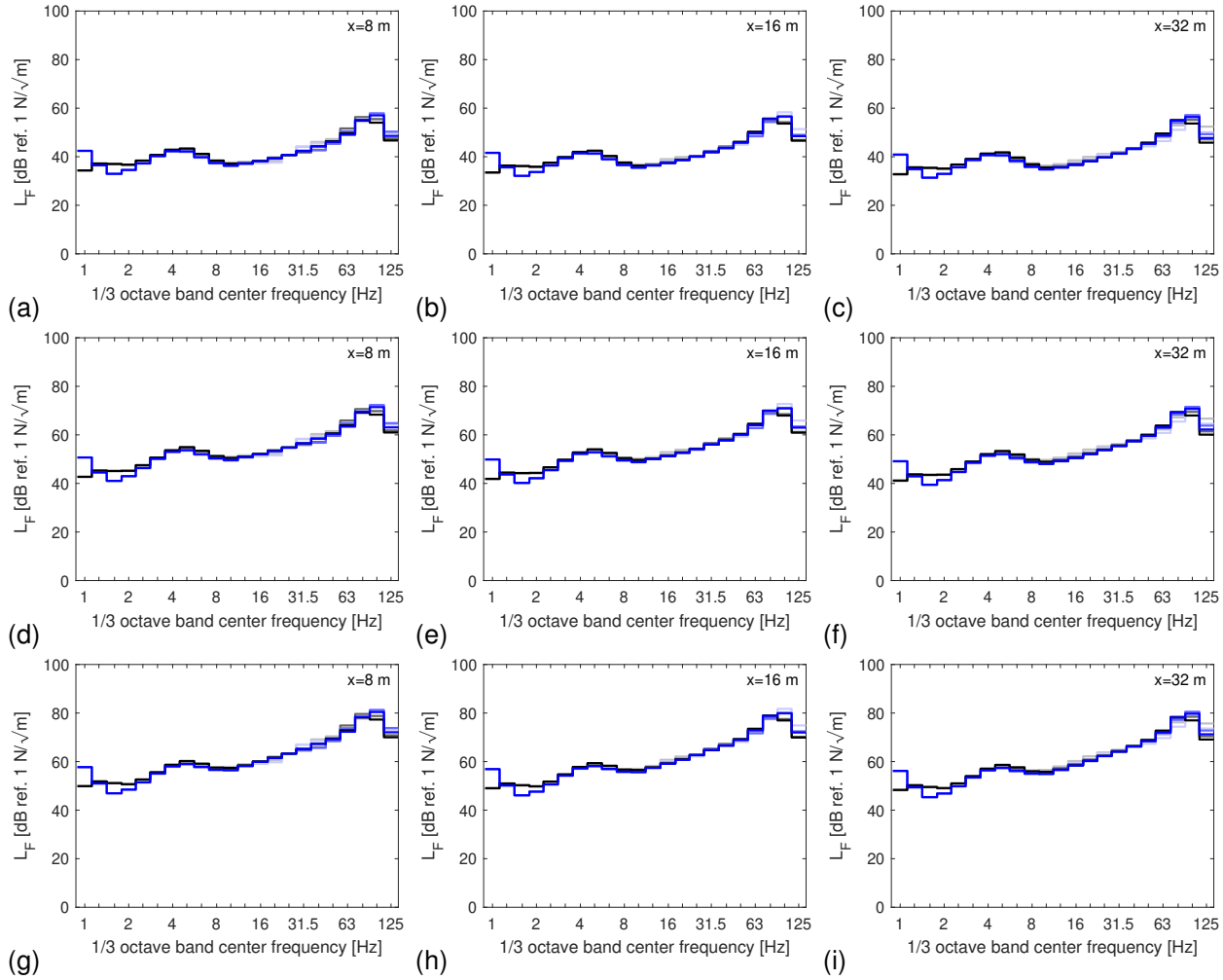

Figure 76: Force density $\mathrm{L_F}(\mathbf{X}, \mathbf{x}_1)$ for the IC train running at (a-c) 50 km/h, (d-f) 150 km/h and (g-i) 300 km/h on the slab track supported by soft, medium and stiff soil (light to dark lines). Receivers are located at (a,d,g) 8 m, (b,e,h) 16 m and (c,f,i) 32 m from the track. Results are computed with TRAFFIC (grey lines) and the prototype vibration prediction tool (blue lines).

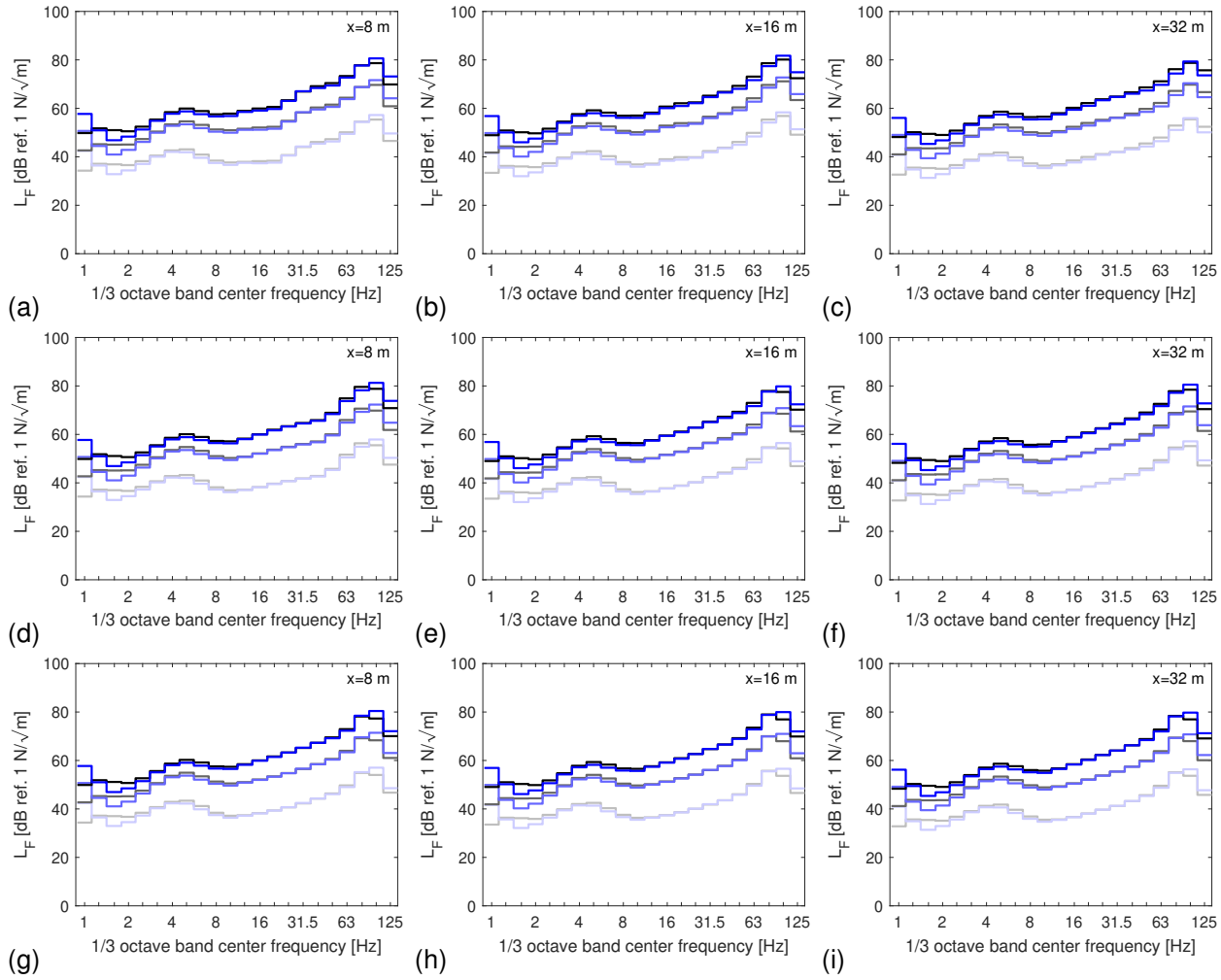

Figure 77: Force density $\mathrm{L_F}(\mathbf{X}, \mathbf{x}_1)$ for the IC train running at 50 km/h, 150 km/h and 300 km/h (light to dark lines) on the slab track supported by (a-c) soft, (d-f) medium and (g-i) stiff soil. Receivers are located at (a,d,g) 8 m, (b,e,h) 16 m and (c,f,i) 32 m from the track. Results are computed with TRAFFIC (grey lines) and the prototype vibration prediction tool (blue lines).

4.5 Conclusions

A numerical validation of the prototype vibration prediction tool was presented in this section. Predictions of the line source transfer mobility, vibration velocity level and force density for the ballasted and slab track were computed with the prototype tool, and with TRAFFIC including the modelling simplifications presented in section 3. The prototype tool uses pre-computed soil impedance and transfer functions in the frequency-wavenumber domain for a fixed track width equal to 3 m, which deviates from the actual track width of the ballasted and slab track (3.6 m and 3.4 m, respectively).

First, the influence of the track width on the soil impedance and transfer functions was assessed. It was concluded that increasing the track width results in higher soil stiffness (and higher dynamic axle loads), but lower transfer mobility. Hence, it is difficult to estimate the impact of the track width on the vibration velocity level in advance.

The line source transfer mobility, vibration velocity level and force density predicted with the prototype vibration prediction tool and TRAFFIC are in very good agreement. Differences mainly occur at high frequencies, but are limited to 4 dB. The discrepancy can be attributed to the lower width of the track-soil interface in the prototype tool due to the use of pre-computed soil impedance and transfer functions. This validation shows that the implementation of vehicle, track and soil models is correct in the prototype vibration prediction tool.

5. EXPERIMENTAL VALIDATION

5.1 Introduction

This section presents the comparison of the results of the prototype vibration prediction tool with experimental data collected at a site in Lincent (Belgium) on the high speed line L2 connecting Brussels and Köln. The measured data include passages of IC and Thalys trains, as well as track-soil transfer functions. Additional tests (borings, SASW tests and SCPTs) were performed to estimate the dynamic soil characteristics.

The section is organized as follows. First, a detailed description of the experimental case history is presented, including track, soil and train properties as well as the track unevenness. A comparison of the measured and predicted line source transfer mobility is presented next. Subsequently, the measured and predicted vibration velocity level and force density for a passage of the IC train at 198 km/h and the Thalys train at 292 km/h are discussed. The section is concluded with hybrid predictions of the vibration velocity level, where either the source or propagation term in the numerical model is replaced by measured data.

5.2 Case description

5.2.1 Measurement site

An extensive measurement campaign has been carried out at a site in Lincent (Belgium) on the high speed line L2 connecting Brussels and Köln. The section between Brussels and Liège was constructed between 1998 and 2002 and mainly follows the E40 highway. The test site in Lincent is located next to the high speed line L2 at kilometer 61.450, near the access point in the Rue de la Bruyère. Figure 78a provides a satellite view of the test location, showing the high speed line next to the E40 highway. Figure 78b shows a plan of the measurement site.

The high speed railway line is constructed in an excavation and runs parallel to the E40 highway separated by an embankment. A cross-section of the site is shown in Figure 79. The access point in the Rue de la Bruyère is located at the opposite side of the embankment, where the free field has an approximately horizontal surface. The excavation, varying in depth along the railway line, is around 1 m deep near the access point.

5.2.2 Track properties

The high speed line L2 consists of two railway tracks, one track in the direction of Liège (track 1) and one track in the direction of Brussels (track 2). It is assumed that both tracks can be considered as separate tracks. The ballasted track consists of two UIC 60 rails supported every 0.6 m by rubber pads on monoblock concrete sleepers. The track gauge equals 1.435 m. The track properties are summarized in Table 10.

The UIC 60 rails are continuously welded and have bending stiffness $E_{\mathrm{r}}I_{\mathrm{r}} = 6.42 \times 10^{6}\,\mathrm{Nm}^2$ and mass per unit length $\rho_{\mathrm{r}}A_{\mathrm{r}} = 60\,\mathrm{kg/m}$. The rails are modelled as Euler-Bernoulli beams.

(a)

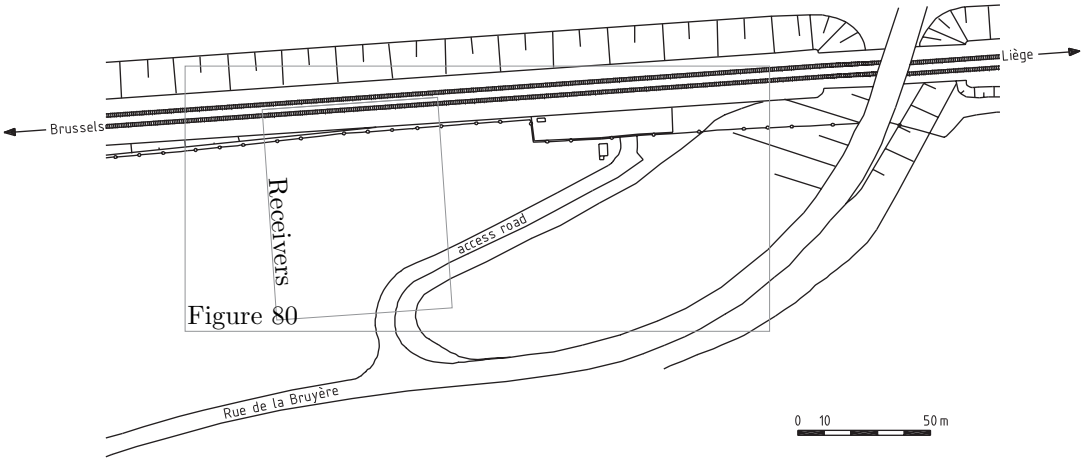

(b)

Figure 78: (a) Satellite view of the measurement site in Lincent. (b) Plan of the measurement site. The two boxes correspond to the location of the receivers and the SCPT, SASW and SR tests (figure 80).

The rails are fixed with a Pandrol E2039 rail fastening system and supported by resilient studded rubber rail pads (type 5197) with a thickness of 11 mm. Each rail pad is preloaded with a clip toe load of about 20 kN per rail seat. In order to determine the rail pad properties, a numerical track model was fitted to track receptance measurements in loaded conditions [8]. This results in an estimate for the rail pad stiffness $k_{\mathrm{rp}} = 153.4 \times 10^6$ N/m and viscous damping coefficient $c_{\mathrm{rp}} = 13.5 \times 10^3$ Ns/m. An equivalent, smeared rail pad stiffness $\bar{k}_{\mathrm{rp}} = k_{\mathrm{rp}}/d = 255.7 \times 10^6$ N/m^2 and damping coefficient $\bar{c}_{\mathrm{rp}} = c_{\mathrm{rp}}/d = 22.5 \times 10^3$ Ns/m^2 are computed to be used in a longitudinally invariant track model by dividing by the distance $d = 0.6$ m between two sleepers.

The prestressed concrete monoblock sleepers have a length $l_{\mathrm{slp}} = 2.5$ m, a width $b_{\mathrm{slp}} = 0.235$ m, a height $h_{\mathrm{slp}} = 0.205$ m (under the rail), a mass $m_{slp} = 300$ kg and a mass moment of inertia $\rho I_{\mathrm{t,slp}} = 157.3$ kgm^2. In a longitudinally invariant model, the smeared sleeper mass equals $\bar{m}_{slp} = 500$ kg/m and mass moment of inertia is $\rho \bar{I}_{\mathrm{t,slp}} = 262.17$ kgm.

The track is supported by a porphyry ballast layer (caliber 25/50, thickness $t_{\mathrm{bal}} = 0.35$ m) and a limestone sub-ballast layer (thickness 0.60 m). The density of these ballast layers is $\rho_{\mathrm{bal}} = 1700$ kg/m^3. The ballast mass per unit length is estimated as $m_{\mathrm{bal}} = \rho_{\mathrm{bal}} t_{\mathrm{bal}} l_{\mathrm{slp}} = 1488$ kg/m. Below the ballast, the soil has been stabilized over a depth of 1 m by means of lime.

The ballast and subgrade properties were estimated by performing a fit of the predicted track receptance with the measured track receptance in a frequency range between 30 Hz and 200 Hz [18], assuming

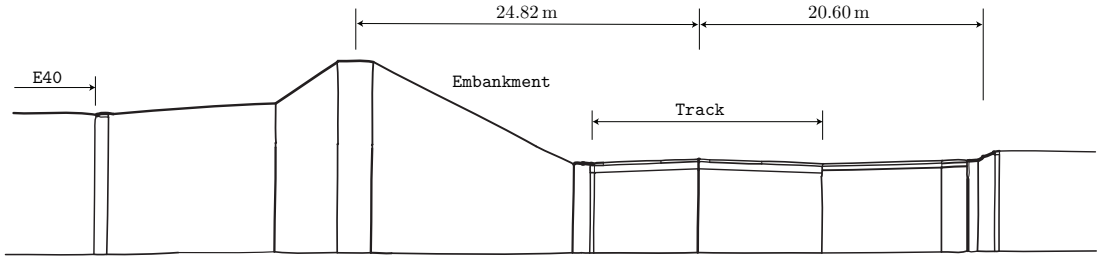

Figure 79: Cross-section of the measurement site in Lincent.

Table 10: Track properties for the Lincent site.

UIC60 rail	Rail positions	$l_1 = l_2 = 0.72$ m
	Bending stiffness	$E_\mathrm{r} I_\mathrm{r} = 6.42 \times 10^6$ Nm^2
	Mass per unit length	$\rho_\mathrm{r} A_\mathrm{r} = 60$ kg/m
Rail pad	Stiffness	$k_\mathrm{rp} = 153.4 \times 10^6$ N/m
	Viscous damping coefficient	$c_\mathrm{rp} = 13.5 \times 10^3$ Ns/m
Sleeper	Length	$l_\mathrm{slp} = 2.5$ m
	Width	$b_\mathrm{slp} = 0.235$ m
	Height	$h_\mathrm{slp} = 0.205$ m
	Mass	$m_\mathrm{slp} = 300$ kg
	Mass moment of inertia	$\rho I_\mathrm{t,slp} = 157.3$ kgm^2
	Spacing	$d = 0.6$ m
Ballast	Thickness	$t_\mathrm{bal} = 0.35$ m
	Top width	$b_\mathrm{bal}t = 3.6$ m
	Bottom width	$b_\mathrm{bal}b = 5.6$ m
	Mass per unit length	$m_\mathrm{bal} = 1488$ kg/m
	Stiffness per sleeper	$k_\mathrm{bal} = 180 \times 10^6$ N/m
	Hysteretic loss factor	$\eta_\mathrm{bal} = 0.06$
Subgrade	Thickness	$t_\mathrm{sub} = 1.0$ m
	Shear wave velocity	$C_\mathrm{s,sub} = 300$ m/s
	Density	$\rho_\mathrm{sub} = 1854$ kg/m^3

a Poisson's ratio $\nu = 1/3$. This results in an estimated shear wave velocity $C_\mathrm{s,bal} = 153.7$ m/s and $C_\mathrm{s,sub} = 300$ m/s for the ballast and subgrade, respectively. The ballast stiffness per sleeper is subsequently estimated as $k_\mathrm{bal} = K_\mathrm{bal} l_\mathrm{slp} b_\mathrm{slp} = E_\mathrm{bal} l_\mathrm{slp} b_\mathrm{slp} / t_\mathrm{bal} = 180 \times 10^6$ N/m, where $K_\mathrm{bal} = 306 \times 10^6$ N/m^3 is the ballast bedding modulus and $E_\mathrm{bal} = 107.1 \times 10^6$ N/m^2 is the Young's modulus. The material damping ratio for the ballast bed was also included as a model parameter in the fit, and was estimated as $\beta_\mathrm{s} = \beta_\mathrm{p} = 0.03$, corresponding to an equivalent hysteretic loss factor $\eta_\mathrm{bal} = 0.06$. In a longitudinally invariant model, the smeared ballast stiffness equals $\bar{k}_\mathrm{bal} = k_\mathrm{bal}/d = 300 \times 10^6$ N/m^2.

5.2.3 Soil properties

At the site in Lincent, several borings were carried out in preparation of the construction of the high speed railway track in order to identify the local geology. The borings reveal the presence of a shallow Quaternary top layer of silt with a thickness of 1.2 m, followed by a layer of fine sand up to a depth of 3.2 m. Between 3.2 m and 7.5 m is a sequence of stiff layers of arenite (a sediment of a sandstone residue) embedded in clay. Below the arenite layers is a layer of clay (from 7.5 m to 8.5 m depth), followed by fine sand (from 8.5 m to 10 m), below which thin layers of fine sand and clay are found.

A number of in situ tests were performed at the site in Lincent for the identification of the (small strain) dynamic soil characteristics, including Seismic Cone Penetration Tests (SCPTs), Spectral Analysis of Surface Waves (SASW) tests and Seismic Refraction (SR) tests. Figure 80 gives an overview of the site with the location of two SCPTs, two SASW tests and two SR tests. The results from these tests are summarized in [19]. Table 11 presents the dynamic soil characteristics at the Lincent site.

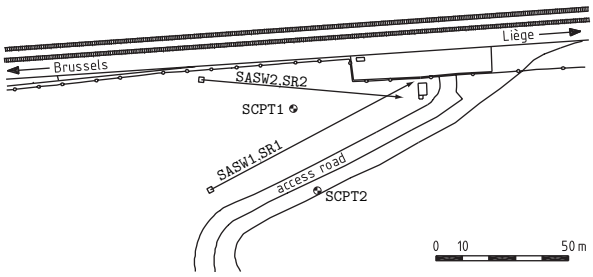

Figure 80: Location of the SCPT, SASW and SR tests at the site in Lincent.

Table 11: Dynamic soil characteristics at the Lincent site.

Layer	h [m]	C_s [m/s]	C_p [m/s]	β_s [-]	β_p [-]	ρ [kg/m^3]
1	1.4	128	286	0.044	0.044	1800
2	2.7	176	286	0.038	0.038	1800
3	∞	355	1667	0.037	0.037	1800

5.2.4 Modelling assumptions

The track is situated in a 1 m deep excavation. Verbraken [18] and Germonpré [5] showed that the excavation does not affect the predicted track compliance provided that it is computed with a reduced height of the top layer (0.4 m instead of 1.4 m in table 11).

Additionally, the effect of the 1 m deep lime stabilization directly below the track on the track compliance was studied. The subgrade stiffening significantly affects the track compliance, and hence, the dynamic axle loads. It cannot be ignored in the numerical model of the track.

Verbraken [18] showed that, for the computation of the track compliance, the lime stabilization can be considered as a 1 m stiffer top layer with estimated properties $C_{\mathrm{s,sub}} = 300\,\mathrm{m/s}$, $\nu = 1/3$ and $\rho_{\mathrm{sub}} =$

$1854\,\mathrm{kg/m^3}$ (see section 3). This results in the soil layering given in table 12. For the computation of the free field response, however, the soil properties in table 11 have to be used.

In the frame of the SILVARSTAR project, the soil impedance and transfer functions are pre-computed (see section 5.2 in Deliverable D2.1 [17]). For the computation of the soil impedance $\tilde{\mathbf{K}}_{\mathrm{s}}(k_y, \omega)$, the soil properties in table 12 are used, as the soil impedance is used to compute the track compliance. The soil properties in table 11 are used to predict free field response, and hence, to pre-compute the transfer functions $\tilde{\mathbf{h}}_{\mathrm{s}}(x, k_y, \omega)$.

Table 12: Dynamic soil characteristics for the computation of the track compliance, accounting for the 1 m deep excavation and 1 m thick lime stabilization below the track [19].

Layer	h [m]	C_{s} [m/s]	C_{p} [m/s]	β_{s} [-]	β_{p} [-]	ρ [kg/m^3]
1	1.0	300	600	0.044	0.044	1854
2	2.1	176	286	0.038	0.038	1800
3	∞	355	1667	0.037	0.037	1800

5.2.5 Train properties

Four different train types are operating on the line L2 in Lincent: the InterCity (IC) trains of type IC-A and IC-O, and the Thalys and ICE high speed trains. A 1-DOF vehicle model (unsprung mass only) is used to compute the dynamic axle loads for the IC trains and the Thalys high speed trains. The train speed for the IC trains varies between 160 km/h to 214 km/h, with an average train speed of 198 km/h. The Thalys train runs at 300 km/h.

IC train

Two IC train types (IC-A and IC-O types) are operating on the line L2. The considered IC train passages correspond to the IC-A type. The IC-A train consists of 1 locomotive HLE 13, 11 standard carriages I11 and 1 end carriage I11 BDx, and has a total length $L_{\mathrm{t}} = 335.91$ m (from first to last axle). The IC-A train is in push mode in the direction of Liège and in pull mode in the direction of Brussels.

Each locomotive and carriage has two independent bogies and four axles. The vehicle length l_{v}, the bogie spacing l_{b}, the axle spacing l_{a}, the total mass per axle m_{t}, the sprung mass m_{s} and the unsprung mass m_{u} of all cars are summarized in table 13.

Table 13: Geometrical and mass properties of the IC-A train [18, 7]: vehicle length l_{v}, bogie spacing l_{b}, axle spacing l_{a}, total mass m_{t}, sprung mass m_{s} and unsprung mass m_{u}.

	Number of axles	l_{v} [m]	l_{b} [m]	l_{a} [m]	m_{t} [kg]	m_{s} [kg]	m_{u} [kg]
Locomotive	4	19.11	10.40	3.00	22500	19677	2823
Central carriage	4	26.40	18.40	2.56	11610	10100	1500
End carriage	4	26.40	18.40	2.56	11830	10286	1544

Thalys train

The Thalys train operating on the line L2 is of the type PBKA. It consists of 2 locomotives, one at each end of the train, and 8 carriages in between and has a total length $L_\mathrm{t} = 200.19\,\mathrm{m}$ (from first to last axle). Each locomotive is supported by two bogies and has four axles. The side carriages, next to the locomotive, have one independent bogie and share the second bogie with the neighbouring carriage. The six remaining central carriages share both bogies with their neighbouring carriages, resulting in an articulated train composition. The total number of bogies is 13 and, consequently, the total number of axles is 26.

The vehicle length l_v, the bogie spacing l_b, the axle spacing l_a, the total mass per axle m_t, the sprung mass m_s and the unsprung mass m_u of all cars are summarized in table 14.

Table 14: Geometrical and mass properties of the Thalys train [18, 7]: vehicle length l_v, bogie spacing l_b, axle spacing l_a, total mass m_t, sprung mass m_s and unsprung mass m_u.

	Number of axles	l_v [m]	l_b [m]	l_a [m]	m_t [kg]	m_s [kg]	m_u [kg]
Locomotive	4	22.15	14.00	3.00	17000	14973	2027
Side carriage	3	21.84	18.70	3.00	17000	14973	2027
Central carriage	2	18.70	18.70	3.00	17000	14973	2027

5.2.6 Track unevenness

The Belgian Railway Company NMBS uses the EM130 measurement vehicle equipped with an Applanix POS/TG system to record the irregularity and alignment of both rails and the curvature, superelevation and grade of the track. The track unevenness at the Lincent site has been measured during a passage on track 1 in the direction of Liège in April 2011. From these measurements, the PSD $\tilde{S}_{u_{\mathrm{w/r}z}}(k_y)$ of the average vertical unevenness of both rails was computed. The PSD is reliable in a wavelength range between 3 m and 63 m. The unevenness for smaller (or larger) wavelengths was extrapolated from the measurements by fitting the PSD to the analytical formula proposed by the FRA given by equation (2). The fit results in an estimate $A = 4.75 \times 10^{-9}$ m, which is lower than the value for FRA class 6 (table 4). The fitted track unevenness level is given in table 15 for 1/3 octave bands with centre wavelengths between 0.0315 m and 100 m.

Table 15: Fit of the measured track unevenness level in dB (ref. 10^{-6} m) at the site in Lincent expressed in one-third octave bands.

Wavelength [m]	Unevenness level [dB ref. 10^{-6} m]
0.0315	-32.7
0.04	-29.7
0.05	-26.7
0.063	-23.7
0.08	-20.7
0.1	-17.6
0.125	-14.6
0.16	-11.6
0.2	-8.6
0.25	-5.6
0.315	-2.6
0.4	0.4
0.5	3.4
0.63	6.4
0.8	9.4
1	12.4
1.25	15.4
1.6	18.3
2	21.2
2.5	24.1
3.15	26.9
4	29.5
5	32.1
6.3	34.4
8	36.6
10	38.5
12.5	40.3
16	42.0
20	43.6
25	45.2
31.5	47.0
40	48.9
50	51.0
63	53.3
80	55.8
100	58.4

5.3 Line source transfer mobility

The line source transfer mobility was measured with hammer impacts applied at the sleeper edge (1.1 m from the centre, source points indicated as $\mathbf{X}_{\mathrm{SL}}$). However, in the computations made with the prototype vibration prediction tool, the source points are considered at both rail heads (0.5 N on each rail, source points indicated as $\mathbf{X}_{\mathrm{BR}}$). Figure 81 plots the line source transfer mobility $\mathrm{TM}_{\mathrm{L}}(\mathbf{X}, \mathbf{x}_1)$ predicted with TRAFFIC for both source point locations. The differences above 25 Hz are due to several reasons. When applying impacts on the sleeper edge, the rotation of the track is excited, while it is not excited with synchronized impacts on the rail heads. The rail pads also filter the vibration velocity level, and the rails spread the energy in the longitudinal direction.

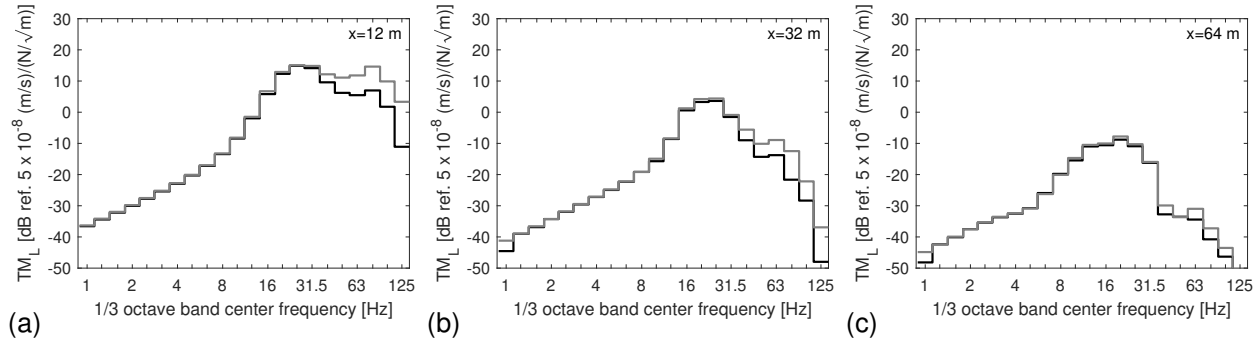

Figure 81: Line source transfer mobility $\mathrm{TM}_{\mathrm{L}}(\mathbf{X}, \mathbf{x}_1)$ for receivers at (a) 12 m, (b) 32 m and (c) 64 m from the track at Lincent. Results are computed with TRAFFIC for source points at both rails (black line) and at the sleeper edge (grey line).

The measured line source transfer mobility is corrected in order to be consistent with the definition of the force density $\mathrm{L}_{\mathrm{F}}(\mathbf{X}, \mathbf{x}_1)$ with impact on the rail heads. The correction corresponds to the difference in line source transfer mobility with impacts on both rails and on the sleeper edge:

$$\Delta\mathrm{TM}_{\mathrm{L}}(\mathbf{X}, \mathbf{x}_1) \quad = \quad \mathrm{TM}_{\mathrm{L}}(\mathbf{X}_{\mathrm{BR}}, \mathbf{x}_1) - \mathrm{TM}_{\mathrm{L}}(\mathbf{X}_{\mathrm{SE}}, \mathbf{x}_1) \tag{29}$$

This correction factor is shown in figure 82. This is larger at high frequency and for smaller distances.

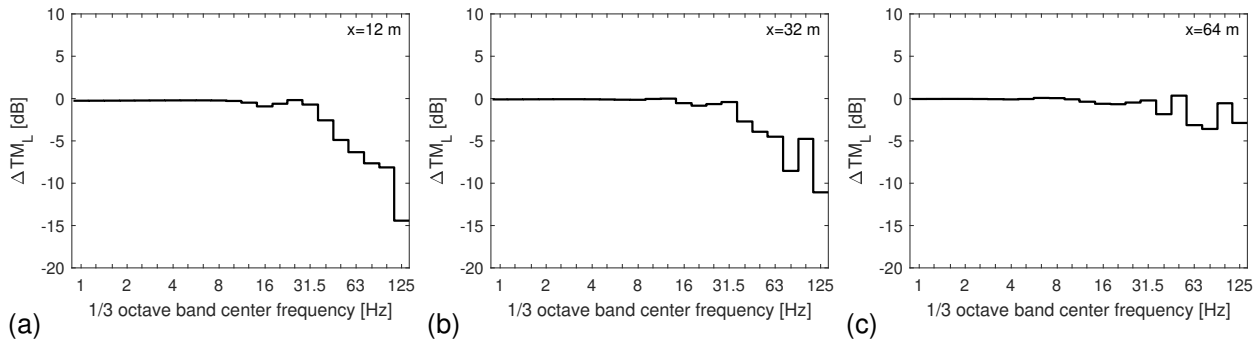

Figure 82: Difference $\Delta\mathrm{TM}_{\mathrm{L}}(\mathbf{X}, \mathbf{x}_1)$ for the line source transfer mobility computed with source points at both rails and at the sleeper edge for receivers at (a) 12 m, (b) 32 m and (c) 64 m from the track at Lincent.

Figure 83 plots the measured line source transfer mobility $\mathrm{TM}_{\mathrm{L}}(\mathbf{X}, \mathbf{x}_1)$, with and without the correction, as

well as the predicted one. Good agreement is obtained between the experimental data and the simulation in the frequency range between 12.5 Hz and 40 Hz. Below 8 Hz, the measured values are quite high due to low frequency measurement noise. Above 40 Hz, the simulated values are generally below the measured values. The best agreement is observed at 32 m. At 64 m, the simulated values are about 10 dB below the measured values, possibly due to underestimated soil damping in the model.

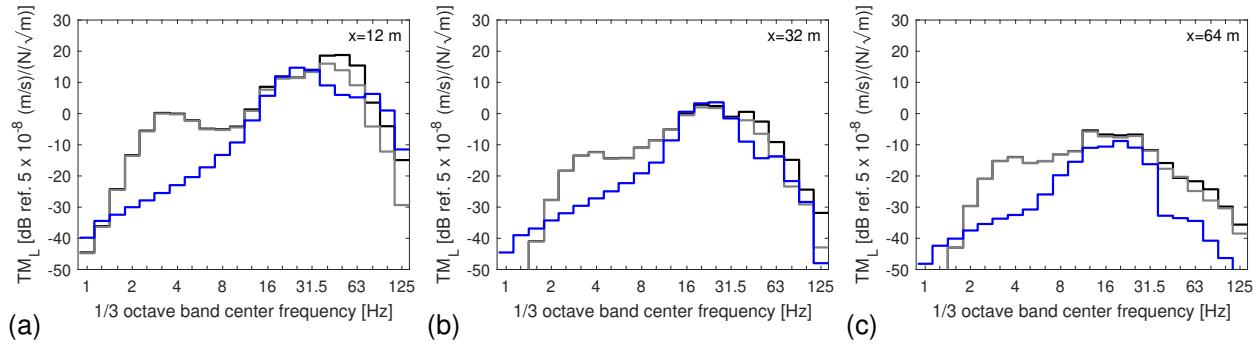

Figure 83: Line source transfer mobility $\mathrm{TM_L}(\mathbf{X}, \mathbf{x}_1)$ for receivers at (a) 12 m, (b) 32 m and (c) 64 m from the track at Lincent. Experimental data are shown for source points at the sleeper edge (black line). The experimental data are corrected to account for the position of the source points (grey line) and are compared to results obtained with the prototype vibration prediction tool (blue line).

5.4 Vibration velocity level

5.4.1 Theoretical considerations

The measured vibration velocity level contains both the quasi-static and dynamic component. Table 16 gives the main frequencies of the quasi-static components due to axle and vehicle spacing, and the parametric excitation due to the sleeper spacing. They are all in the considered frequency range between 1 Hz and 125 Hz. The dynamic component is generally dominated by the P2 (unsprung mass) resonance frequency. With the theoretical mechanical parameters used for the models of the train, the track and the soil (minor influence of the latter), the frequency is close to 50 Hz (45 to 55 Hz) for both trains.

Table 16: Quasi-static and parametric excitation components.

Train	IC-A	Thalys
Speed [km/h]	198	292
Axle spacing [m]	2.56	3.0
Axle passage frequency [Hz]	21.0	27.0
Bogie spacing [m]	10.4 (locomotive); 18.4 (carriage)	14.0 (locomotive); 18.7 (carriage)
Bogie passage frequency [Hz]	5.3 (locomotive); 3.0 (carriage)	5.8 (locomotive); 4.3 (carriage)
Vehicle length [m]	19.1 (locomotive); 26.4 (carriage)	22.15 (locomotive); 18.7 (carriage)
Vehicle passage frequency [Hz]	2.9 (locomotive); 2.1 (carriage)	3.7 (locomotive); 4.3 (carriage)
Sleeper spacing [m]	0.6	0.6
Sleeper passage frequency [Hz]	125.0	85.0

The rail unevenness was measured for wavelengths between 3 m and 63 m, corresponding to a frequency

range from 0.9 Hz to 18 Hz for a train speed of 198 km/h (IC train), and from 1.3 Hz to 27 Hz at 292 km/h (Thalys train). Outside these ranges, the unevenness is unknown and was extrapolated. This limits the validity of the results obtained with the numerical model based on the extrapolated unevenness.

5.4.2 IC train

Figure 84 shows the vibration velocity level, measured and predicted with the prototype vibration prediction tool, during the passage of the IC train. The experimental data show multiple train passages at ± 10 dB around the average value at high frequencies, and up to ± 20 dB below 10 Hz. Around 50 Hz, the numerical and the experimental data show a peak related to the P2 (unsprung mass) resonance. A peak is observed at 20 Hz due to the axle passage frequency.

In the experimental data, the quasi-static contribution is observed below 8 Hz close to the track; the prototype tool only considers the response due to dynamic axle loads and thus disregards the quasi-static contribution to the vibration velocity level. The coach and bogie suspension modes also affect the response at low frequencies. However, these are not accounted for by the numerical model, as the vehicle model only considers the unsprung mass. These two factors explain the difference between numerical and experimental results below 25 Hz.

Above 60 Hz, the predicted vibration velocity level is lower than the measured data, which is consistent with observations for the $\mathrm{TM_L}(\mathbf{X}, \mathbf{x}_1)$ (figure 83). This effect is compounded by the fact that the rail and wheel unevenness are unknown (not measured) in this frequency range.

Although the energy is concentrated in different frequency bands, the difference between the measured and predicted global vibration level $\mathrm{L_v^{global}}(\mathbf{x}_1)$ is less than 2 dB as shown in table 17. This shows that, overall, a good estimate of the vibration velocity level during the passage of the IC train is predicted.

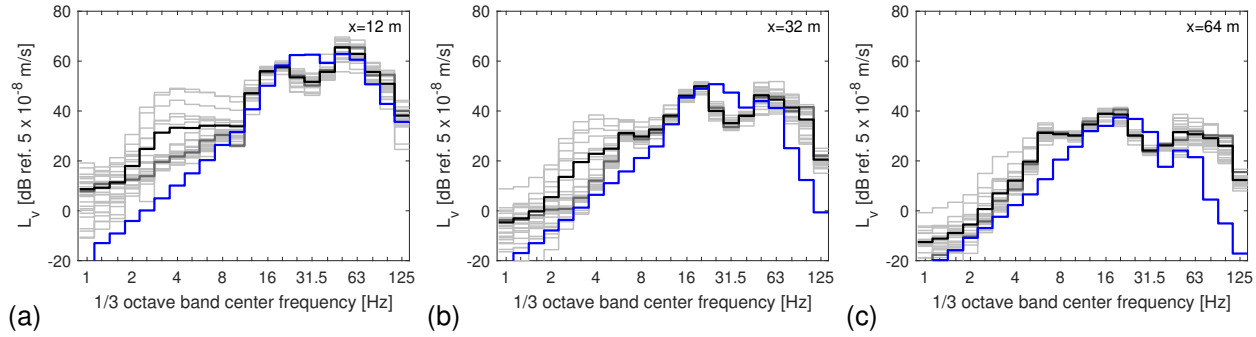

Figure 84: Vibration velocity level $\mathrm{L_v}(\mathbf{x}_1)$ for receivers at (a) 12 m, (b) 32 m and (c) 64 m from the track at Lincent. A total of 26 passages of the IC-A train in a speed range between 178 km/ and 218 km/h were measured (light grey lines), from which the average vibration velocity level (black line) is computed. A single passage (dark grey line) and the vibration velocity level predicted with the prototype tool (blue line) for the IC train running at 198 km/h are also shown.

5.4.3 Thalys train

Figure 85 shows the measured and predicted (with the prototype vibration prediction tool and with TRAFFIC) vibration velocity level $\mathrm{L_v}(\mathbf{x}_1)$ during the passage of the Thalys train at 292 km/h. The TRAFFIC

Table 17: Measured and predicted global vibration velocity level $\mathrm{L}_{\mathrm{v}}^{\mathrm{global}}(\mathbf{x}_1)$ [dB ref. 5×10^{-8} m/s] at 12 m, 32 m and 64 m from the track at Lincent during the passage of the IC-A train running at 198 km/h.

Receiver location x	12 m	32 m	64 m
Measured	68.9	54.2	44.3
Predicted with the prototype tool	69.3	55.3	42.3

Table 18: Measured and predicted global vibration velocity level $\mathrm{L}_{\mathrm{v}}^{\mathrm{global}}(\mathbf{x}_1)$ [dB ref. 5×10^{-8} m/s] at 12 m, 32 m and 64 m from the track at Lincent during the passage of the Thalys train running at 292 km/h.

Receiver location x	12 m	32 m	64 m
Measured	67.0	58.5	48.1
Predicted with the prototype tool	76.4	61.8	48.3
Predicted with TRAFFIC	76.8	60.9	46.1

predictions account for the quasi-static contribution due to the moving constant axle loads. A clear peak is observed at 4 Hz corresponding to the vehicle passage frequency. The peak around 25 Hz is due to the axle spacing. These peaks are also visible in the measured data. The P2 resonance is observed around 50 Hz to 63 Hz in the measured data, and at 50 Hz in the predictions.

The agreement between measurements and predictions is relatively good in the frequency range where the track unevenness was measured (below 27 Hz). The vibration velocity level is highly overestimated at 12 m between 20 Hz and 80 Hz. Better agreement is found at 32 m and 64 m, but the predicted response above 80 Hz is much lower than the measured response. This was also the case for the IC train, and is possibly related to an overestimation of the material damping ratio in the soil as well as the extrapolated unevenness data.

As seen in table 18, the global vibration velocity level difference between measurements and predictions with the prototype vibration prediction tool is up to 9 dB at 12 m, but about 3 dB at 32 m and less than 1 dB at 64 m. The predictions with TRAFFIC (including quasi-static effects and moving dynamic axle loads) are very close to the predictions with the prototype vibration prediction tool: a 1 dB to 2 dB difference on the global vibration velocity level is found between the two models.

5.5 Force density

The force density can be computed using the FRA procedure (equation (20)), which estimates the force density as the difference between the vibration velocity level and the line source transfer mobility. Alternatively, it can be computed directly from the dynamic axle loads (equation (21)). With the first approach, the force density can be determined experimentally as well as numerically, while the latter approach only allows for a numerical prediction of the force density.

5.5.1 IC train

Figure 86 shows the prediction of the force density with the prototype vibration prediction tool, using the aforementioned approaches (FRA procedure and based on dynamic axle loads). Differences of about 5 dB

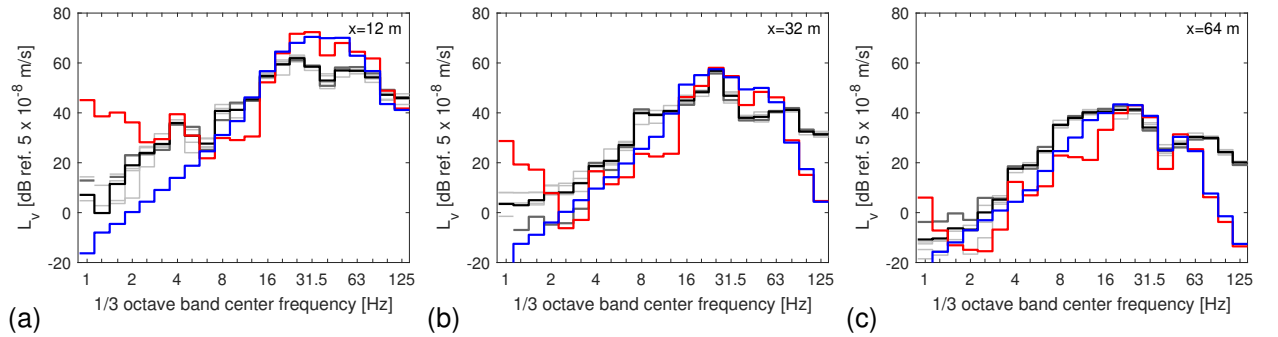

Figure 85: Vibration velocity level $\mathrm{L_v}(\mathbf{x}_1)$ for receivers at (a) 12 m, (b) 32 m and (c) 64 m from the track at Lincent. A total of 5 passages of the Thalys train in a speed range between 272 km/ and 312 km/h were measured (light grey lines), from which the average vibration velocity level (black line) is computed. A single passage (dark grey line) and the vibration velocity level predicted with the prototype tool (blue line) and TRAFFIC (red line) for the Thalys train running at 292 km/h are also shown.

are observed at high frequencies. The P2 resonance is clearly observed around 50 Hz.

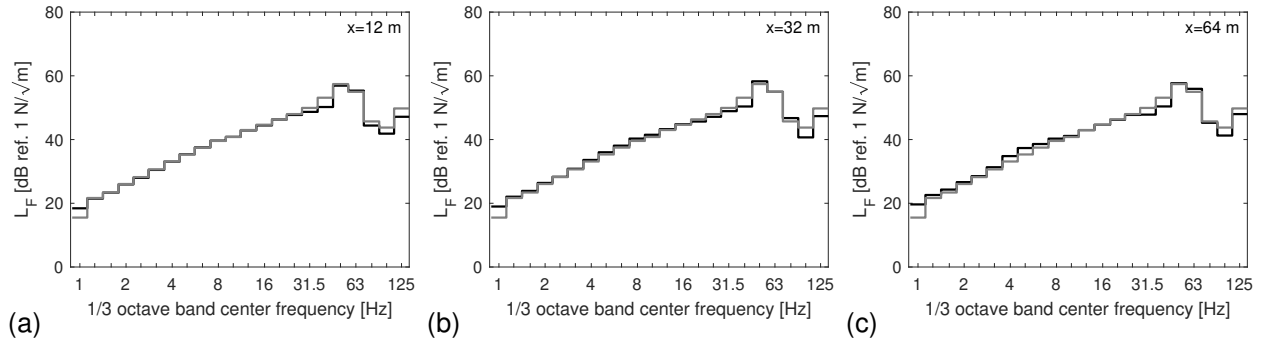

Figure 86: Force density $\mathrm{L_F}(\mathbf{X}, \mathbf{x}_1)$ for receivers at (a) 12 m, (b) 32 m and (c) 64 m from the track at Lincent. Results are computed with the prototype tool for the passage of the IC-A train at 198 km/h using the FRA procedure (black line) and a direct computation from the dynamic axle loads (grey line).

Figure 87 depicts the force density computed with the FRA procedure obtained from measured data and predicted with the prototype tool. Note that the corrected $\mathrm{TM_L}(\mathbf{X}, \mathbf{x}_1)$ (to allow for different excitation positions on both rails instead of sleeper edges) is used for the computation of the experimental force density (see subsection 5.3). The numerical results are close to the average measured force density (black line), except below 2 Hz, between 25 Hz and 40 Hz, and above 63 Hz. The numerical curves show a clear peak at the P2 resonance, while this phenomenon is not visible in the experimental data.

5.5.2 Thalys train

Figure 88 shows the force density for the Thalys train running at 292 km/h obtained numerically with the prototype tool using the FRA procedure and based on the dynamic axle loads. Differences of about 5 dB are observed. The P2 resonance is clearly seen at 50 Hz.

Figure 89 shows the force density computed with the FRA procedure obtained from measured data and

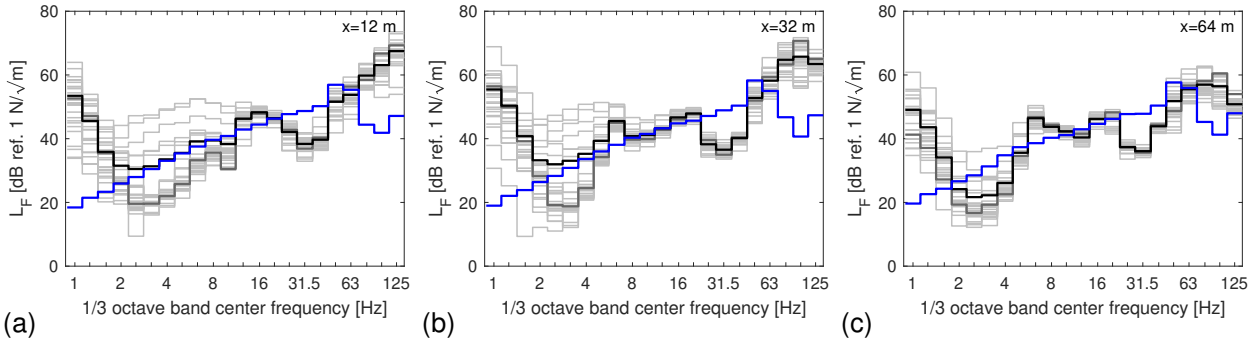

Figure 87: Force density $\mathrm{L_F}(\mathbf{X}, \mathbf{x}_1)$ for receivers at (a) 12 m, (b) 32 m and (c) 64 m from the track at Lincent. The force density is estimated with the FRA procedure for the 26 passages of the IC-A train in the speed range between 178 km/h and 212 km/h (grey lines), from which the average force density (black line) is computed. The force density for a single passage at 198 km/h (dark grey line) and the prediction with the prototype tool (blue line) using the FRA procedure is also shown.

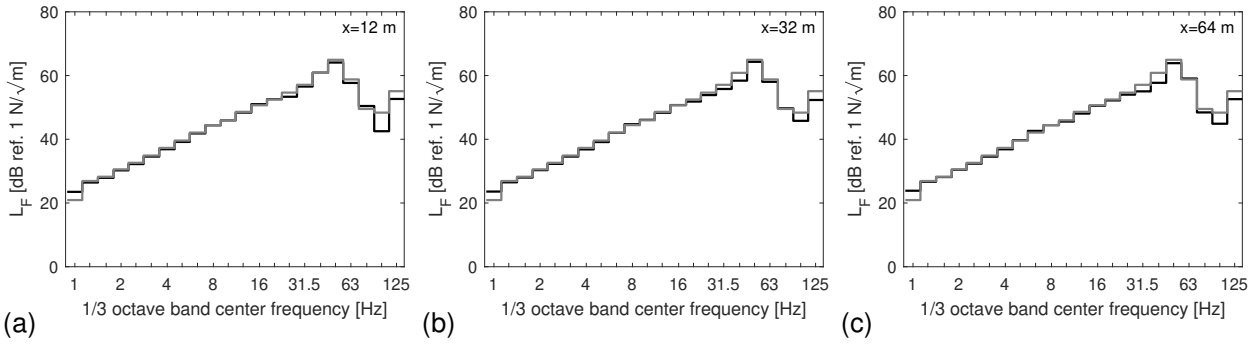

Figure 88: Force density $\mathrm{L_F}(\mathbf{X}, \mathbf{x}_1)$ for receivers at (a) 12 m, (b) 32 m and (c) 64 m from the track at Lincent. Results are computed with the prototype tool for the passage of the Thalys train at 292 km/h using the FRA procedure (black line) and a direct computation from the dynamic axle loads (grey line).

from numerical predictions. Note that the corrected $\mathrm{TM_L}(\mathbf{X}, \mathbf{x}_1)$ is used for the computation of the experimental force density (see subsection 5.3). The numerical prediction shows a clear peak at the P2 resonance, while this phenomenon is not visible in the experimental data.

5.5.3 Average force density

For hybrid predictions where the source term corresponds to an experimentally determined force density $\mathrm{L_F}(\mathbf{X}, \mathbf{x}_1)$ (hybrid model 2), an average force density is extracted from the measured data as follows. The force density is computed at each receiver location and is shown in figure 90. The force densities obtained at 8 m, 16 m and 24 m show very low (and abnormal) values below 16 Hz, and are therefore disregarded in the computation of the average force density. The force density at 6 m is also disregarded as the quasi-static contribution affects the force density at low frequencies. The average force density is also shown on figure 90 and used for the hybrid predictions in the next section.

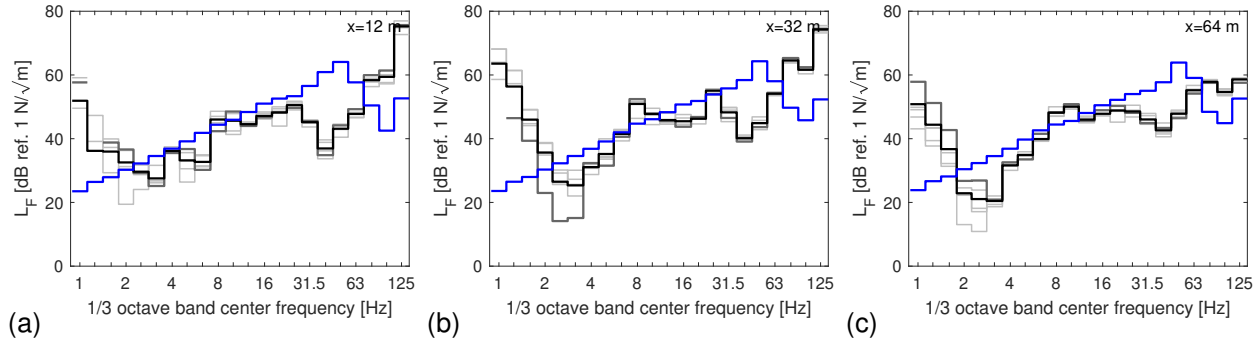

Figure 89: Force density $\mathrm{L_F}(\mathbf{X}, \mathbf{x}_1)$ for receivers at (a) 12 m, (b) 32 m and (c) 64 m from the track at Lincent. The force density is estimated with the FRA procedure for the 5 passages of the Thalys train in the speed range between 272 km/h and 312 km/h (grey lines), from which the average force density (black line) is computed. The force density for a single passage at 292 km/h (dark grey line) and the prediction with the prototype tool (blue line) using the FRA procedure is also shown.

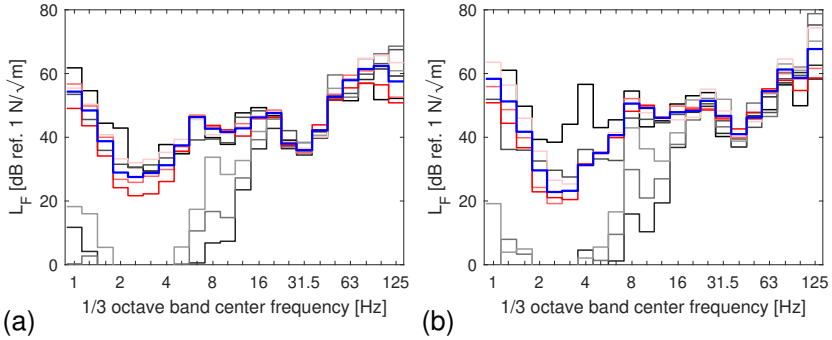

Figure 90: Average force density $\mathrm{L_F}(\mathbf{X}, \mathbf{x}_1)$ for receivers at 6, m, 8 m, 16 m and 24 m (black to light grey lines) and 12 m, 32 m, 48 m and 64 m (dark to light red lines) from the track at Lincent. The average force density is estimated with the FRA procedure for (a) 26 passages of the IC-A train and (b) 5 passages of the Thalys train. The average force density (blue line) is computed from the force density at 12 m, 32 m, 48 m and 64 m.

5.6 Hybrid prediction

The vibration velocity level $\mathrm{L_v}(\mathbf{x}_1)$ is now computed with two hybrid models:

- hybrid model 1: predicted force density $\mathrm{L_F}(\mathbf{X}, \mathbf{x}_1)$ combined with a measured line source transfer mobility $\mathrm{TM_L}(\mathbf{X}, \mathbf{x}_1)$ (with correction term for impact locations),
- hybrid model 2: measured force density $\mathrm{L_F}(\mathbf{X}, \mathbf{x}_1)$ (average) combined with a predicted line source transfer mobility $\mathrm{TM_L}(\mathbf{X}, \mathbf{x}_1)$.

The results obtained with both hybrid models are compared to fully numerical computations as well as measured vibration velocity levels.

5.6.1 IC train

Figure 91 compares the experimental data to the hybrid and fully numerical predictions for the IC train. Hybrid model 1 (predicted force density and measured line source transfer mobility) overestimates the vibration velocity level around the P2 resonance at 50 Hz. This is due to the fact the unevenness in this frequency range was not measured. Hybrid model 2 (measured force density and predicted line source transfer mobility) gives better agreement with measurements, especially at 32 m.

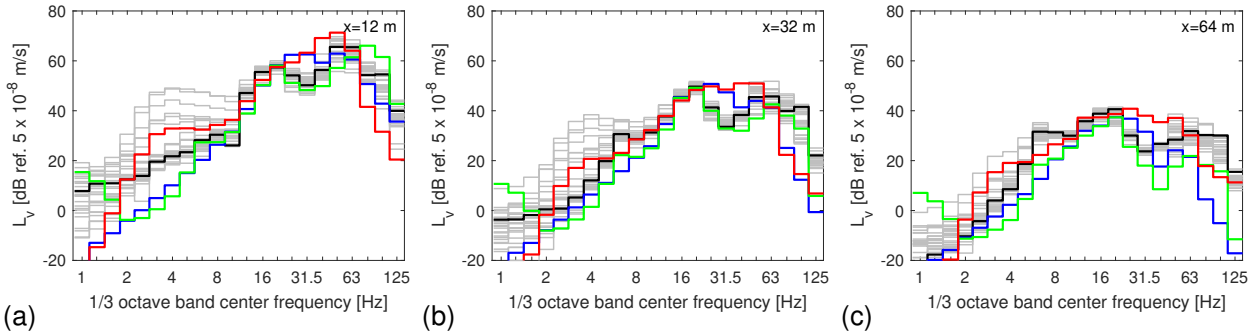

Figure 91: Vibration velocity level $\mathrm{L_v}(\mathbf{x}_1)$ for receivers at (a) 12 m, (b) 32 m and (c) 64 m from the track at Lincent. A total of 26 passages of the IC-A train in a speed range between 178 km/ and 218 km/h were measured (light grey lines), from which the average vibration velocity level (black line) is computed. The vibration velocity level is also computed with the prototype tool: fully numerical (blue line), hybrid model 1 (red line) and hybrid model 2 (green line).

Table 19 summarizes the measured and predicted global vibration velocity levels. Hybrid model 1 gives the largest discrepancies compared to measurements, with differences of up to 5 dB. The fully numerical model and hybrid model 1 give differences of 1 dB to 2 dB compared to the measured data. These differences are acceptable for numerical predictions, given the model and parameter uncertainty.

Table 19: Measured and predicted global vibration velocity level $\mathrm{L_v^{global}}(\mathbf{x}_1)$ [dB ref. 5×10^{-8} m/s] at 12 m, 32 m and 64 m from the track at Lincent during the passage of the IC-A train running at 198 km/h.

Receiver location x	12 m	32 m	64 m
Measured	68.9	54.2	44.3
Predicted with the prototype tool	69.3	55.3	42.3
Predicted with hybrid model 1	74.5	57.3	46.8
Predicted with hybrid model 2	69.3	52.1	40.0

5.6.2 Thalys train

Figure 92 compares the experimental data to the hybrid and fully numerical predictions for the Thalys train. Similar to the IC train, hybrid model 1 overestimates the vibration velocity level around the P2 resonance frequency at 50 Hz. Hybrid model 2 gives better agreement with the experimental data.

Table 20 lists the global vibration velocity levels for the measurements and the simulations. The highest

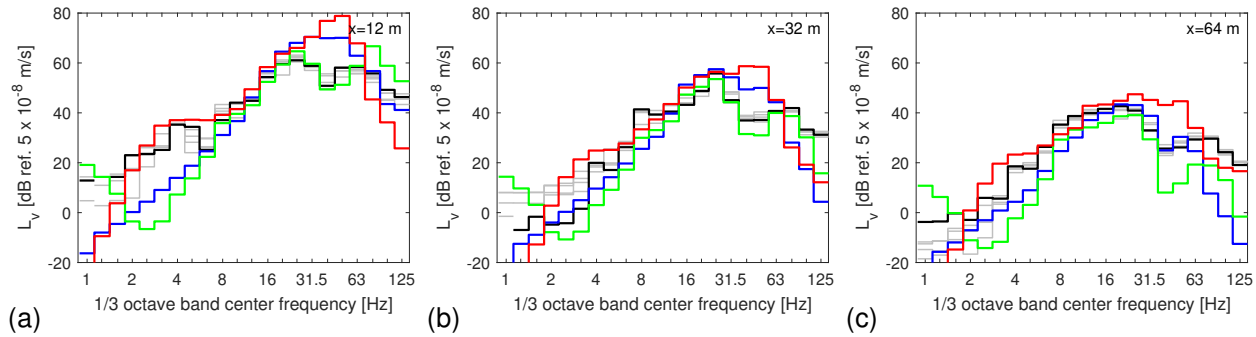

Figure 92: Vibration velocity level $\mathrm{L_v}(\mathbf{x}_1)$ for receivers at (a) 12 m, (b) 32 m and (c) 64 m from the track at Lincent. A total of 5 passages of the Thalys train in a speed range between 272 km/ and 312 km/h were measured (light grey lines), from which the average vibration velocity level (black line) is computed. The vibration velocity level is also computed with the prototype tool: fully numerical (blue line), hybrid model 1 (red line) and hybrid model 2 (green line).

discrepancies are observed at 12 m, with about 15 dB difference for hybrid model 1. Hybrid model 2 gives better agreement with differences up to 4 dB.

Table 20: Measured and predicted global vibration velocity level $\mathrm{L_v^{global}}(\mathbf{x}_1)$ [dB ref. 5×10^{-8} m/s] at 12 m, 32 m and 64 m from the track at Lincent during the passage of the Thalys train running at 292 km/h.

Receiver location x	12 m	32 m	64 m
Measured	67.0	58.5	48.1
Predicted with the prototype tool	76.4	61.8	48.3
Predicted with hybrid model 1	81.7	64.3	53.4
Predicted with hybrid model 2	70.6	56.5	44.1

5.7 Conclusions

This section presented the experimental validation of the prototype vibration prediction tool using measurement data (transfer functions and train passages) from a site at Lincent (Belgium). The predictions with the prototype tool consist of fully numerical as well as hybrid computations.

The comparison between experimental data and numerical predictions at the Lincent site shows reasonably good agreement overall. The main discrepancies are due to several reasons. First, the soil stratification and excavation at the site are complex, and not easy to model. More sophisticated models are required to capture accurately the influence of the excavation of the track and the subgrade stiffening below the track on the track impedance and the free field vibration. Furthermore, the rail unevenness has been extrapolated, leading to large uncertainty above 25 Hz for the considered train speeds. In addition, the wheel roughness is unknown and neglected. The quasi-static contribution is not taken into account, but is observed in the measured data up to 25 Hz for the considered train speeds.

When comparing the global vibration velocity levels, differences between measurements and predictions are reasonable: 1 dB for the best cases, with an average difference of about 4 dB, but up to 15 dB for the worst case. In one-third octave bands, the differences can also reach 15 dB to 20 dB, but the highest discrepancies are generally observed below 10 Hz, where the energy is low anyway. The discrepancies are mainly due to the fact that the quasi-static contribution and the bogie and coach suspension modes are not accounted for in the numerical predictions. In general, the models tend to overestimate the global vibration levels. Hybrid model 1 (predicted force density and measured line source transfer mobility) tends to highly overestimate the vibration velocity levels, with differences up to 20 dB for the worst case. Predictions with hybrid model 2 (measured force density and predicted line source transfer mobility) give global vibration levels that differ up to 4 dB compared to measurements, which is acceptable. The fully numerical model gives the same level of discrepancies.

In conclusion, the prototype vibration prediction tool is compared with measured data, and reasonable agreement was achieved, despite the simplifying assumptions made in the prediction tool and the remaining uncertainty on the track and soil properties.

6. CONCLUSIONS

This report presents the numerical and experimental validation of the prototype vibration prediction tool.

For the numerical validation, 18 case histories are considered for the IC train running at 50 km/h, 150 km/h and 300 km/h on a ballasted and slab track supported by soft, medium and stiff soil. Results computed with state-of-the-art numerical models (TRAFFIC and MOTIV) are compared in section 2. For the ballasted track, the track compliance and dynamic axle loads are in excellent agreement. At high frequencies, however, deviations up to 5 dB are observed in the line source transfer mobility and up to 10 dB in the vibration velocity level due to different kinematic assumptions at the track-soil interface. For the slab track, the track compliance and the dynamic axle loads are also in excellent agreement. The line source transfer mobility differs by maximum 1 dB, while deviations of up to 5 dB are observed for the vibration velocity level above 30 Hz.

In section 3, the effects of three modelling simplifications made in the prototype vibration prediction tool are quantified using TRAFFIC: (1) computation of the track compliance for non-moving instead of moving loads, (2) fixed positions of the dynamic axle loads (low-speed approximation), and (3) incoherent instead of coherent axle loads. The influence of the train speed on the track compliance is negligible and can be disregarded in the prediction of vibration velocity levels (differences less than 1 dB). The assumption of fixed positions of the dynamic axle loads disregards the Doppler effect, resulting in a redistribution of energy to different frequency bands. Significant differences (up to 20 dB in some frequency bands) are observed for the vibration velocity level, particularly when the train speed is high compared to the dominant wave velocity in the soil. The assumption of incoherent axle loads mainly affects the vibration velocity level below 20 Hz, where the response is low. For the global vibration velocity level, slightly higher values (up to 4 dB) are found when all simplifications are included in the model, which is mainly due to the low-speed approximation.

In section 4, the prototype vibration prediction tool is validated against the state-of-the-art model TRAFFIC. For the 18 case histories, the line source transfer mobility, vibration velocity level, and force density are computed. In TRAFFIC, the same modelling simplifications are imposed as in the prototype vibration prediction tool (section 3). The latter, however, uses pre-computed soil impedance and transfer functions for selected widths of the track-soil interface. First, the soil impedance and transfer functions for the actual track width are compared with those available in the database; the influence of the width is only observed at high frequencies and remains limited. This is also reflected in the line source transfer mobility: the difference between the prototype vibration prediction tool and TRAFFIC is limited to 3 dB at high frequencies. The vibration velocity level and the force density are also in very good agreement, which demonstrates that the computational core of the prototype vibration prediction tool is implemented correctly.

In section 5, the prototype vibration prediction tool is validated against experimental data collected on a site in Lincent. The measured and predicted line source transfer mobility are in relatively good agreement when a correction term is introduced that accounts for the impact position (on the sleeper edge in the experiments and on the rail heads in the prediction model). The measured data contain high levels of low frequency noise. The measured and predicted vibration velocity levels show similar trends, including peaks due to the axle passages and the P2 resonance. Significant differences at low frequencies are due to the omission of the quasi-static contribution and the bogie and coach suspension modes in the numerical model. At high frequencies, the predicted response is much lower than the measured one far from the track, which may be due to an overestimation of material damping in the soil. The difference on the global vibration level is generally limited to a few dB, which shows that the prototype vibration prediction tool is

able to make acceptable predictions despite the uncertainty on track and soil properties and the modelling simplifications.

Hybrid predictions of the vibration velocity level are finally computed with the prototype vibration prediction tool. Hybrid model 1 (predicted force density and line source transfer mobility) overestimates the response between 30 Hz and 60 Hz, and hence the global vibration level. Hybrid model 2 (measured force density and predicted line source transfer mobility) is in better agreement with the measured data. The difference on the global vibration level is around 4 dB, which is similar as for the numerical model.

REFERENCES

[1] S. Barcet, B. Nélain, P. Bouvet, D.J. Thompson, E. Ntotsios, G. Degrande, G. Lombaert, B. Fröhling, and A. Nuber. Description of the vibration prediction tool. SILVARSTAR project GA 101015442, Deliverable D1.2, Report to the EC, June 2022.

[2] G. Degrande, G. Lombaert, E. Ntotsios, D.J. Thompson, B. Nélain, P. Bouvet, S. Grabau, J. Blaul, and A. Nuber. State-of-the-art and concept of the vibration prediction tool. SILVARSTAR project GA 101015442, Deliverable D1.1, Report to the EC, May 2021.

[3] Deutsches Institut für Normung. *DIN 45672 Teil 2: Schwingungsmessungen in der Umgebung von Schienenverkehrswegen: Auswerteverfahren*, 1995.

[4] V.K. Garg and R.V. Dukkipati. *Dynamics of railway vehicle systems*. Academic Press, Canada, 1984.

[5] M. Germonpré. *The effect of parametric excitation on the prediction of railway induced vibration in the built environment*. PhD thesis, Department of Civil Engineering, KU Leuven, 2018.

[6] A. Hamid and T.L. Yang. Analytical description of track-geometry vibrations. *Transportation Research Record 838*, pages 19–26, 1981.

[7] G. Lombaert and G. Degrande. Ground-borne vibration due to static and dynamic axle loads of InterCity and high speed trains. *Journal of Sound and Vibration*, 319(3-5):1036–1066, 2009.

[8] G. Lombaert, G. Degrande, J. Kogut, and S. François. The experimental validation of a numerical model for the prediction of railway induced vibrations. *Journal of Sound and Vibration*, 297(3-5):512–535, 2006.

[9] G. Lombaert, S. François, and G. Degrande. TRAFFIC Matlab toolbox for traffic induced vibrations. Report BWM-2012-10, Department of Civil Engineering, KU Leuven, November 2012. User's Guide Traffic 5.2.

[10] G. Lombaert, P. Galvín, S. François, and G. Degrande. Quantification of uncertainty in the prediction of railway induced ground vibration due to the use of statistical track unevenness data. *Journal of Sound and Vibration*, 333:4232–4253, 2014.

[11] D.R.M. Milne, L.M. Le Pen, D.J. Thompson, and W. Powrie. Properties of train load frequencies and their applications. *Journal of Sound and Vibration*, 397:123–140, 2017.

[12] E. Ntotsios, D.J. Thompson, and M.F.M. Hussein. The effect of track load correlation on ground-borne vibration from railways. *Journal of Sound and Vibration*, 402:142–163, 2017.

[13] E. Ntotsios, D.J. Thompson, and M.F.M. Hussein. A comparison of ground vibration due to ballasted and slab tracks. *Transportation Geotechnics*, 21(100256), 2019.

[14] X. Sheng, C.J.C. Jones, and M. Petyt. Ground vibration generated by a harmonic load acting on a railway track. *Journal of Sound and Vibration*, 225(1):3–28, 1999.

[15] X. Sheng, C.J.C. Jones, and D.J. Thompson. A theoretical model for ground vibration from trains generated by vertical track irregularities. *Journal of Sound and Vibration*, 272(3):937–965, 2004.

[16] M. Shinozuka and G. Deodatis. Simulation of stochastic processes by spectral representation. *Applied Mechanics Reviews*, 44(4):191–204, 1991.

[17] D.J. Thompson, E. Ntotsios, G. Degrande, G. Lombaert, G. Herremans, T. Alexiou, B. Nélain, S. Barcet, P. Bouvet, B. Fröhling, and A. Nuber. Database for vibration emission, ground transmission and building transfer functions. SILVARSTAR project GA 101015442, Deliverable D2.1, Report to the EC, January 2022.

[18] H. Verbraken. *Prediction of railway induced vibration by means of numerical, empirical, and hybrid methods*. PhD thesis, Department of Civil Engineering, KU Leuven, 2013.

[19] H. Verbraken, G. Degrande, G. Lombaert, B. Stallaert, and V. Cuéllar. Benchmark tests for soil properties, including recommendations for standards and guidelines. RIVAS project SCP0-GA-2010-265754, Deliverable D1.11, Report to the EC, December 2013.

[20] P.D. Welch. The use of fast Fourier transform for the estimation of power spectra: A method based on time averaging over short, modified periodograms. *IEEE Transactions on Audio and Electroacoustics*, 15(2):70–73, 1967.